

**Development and Characterization of a Tactile
Array Sensor for Parallel Grippers for Use in
Object Manipulation**

Don Lakmal Madushanka Weerasinghe

(178050F)

Degree of Master of Science by Research

Department of Mechanical Engineering

University of Moratuwa

Sri Lanka

February 2020

Development and Characterization of a Tactile Array Sensor for Parallel Grippers for Use in Object Manipulation

Don Lakmal Madushanka Weerasinghe

(178050F)

Thesis submitted in partial fulfillment of the requirements for the degree Master
of Science in Mechanical Engineering

Department of Mechanical Engineering

University of Moratuwa

Sri Lanka

February 2020

DECLARATION

I hereby declare that this is my own work and this dissertation does not incorporate without acknowledgement any material previously submitted for a Degree or Diploma in any other University or institute of higher learning and to the best of my knowledge and belief it does not contain any material previously published or written by another person except where the acknowledgment is made in the text.

Also, I hereby grant to University of Moratuwa the non-exclusive right to reproduce and distribute my dissertation, in whole or in part in print, electronic or other medium. I retain the right to use this content in whole or part in future works (such as articles or books).

Signature:

Date:

The above candidate has carried out research for the MSc thesis under my supervision.

Signature of the Supervisor(s):

Date:

Dr. Damith Chathuranga

Senior Lecturer

Department of Mechanical Engineering

University of Moratuwa

Abstract

Within the era of modern robotics, during research as well as in industry, it is often the case to build robots that can mimic human-object interaction closely. To accomplish this goal, excellence is required in many technological aspects, where one is tactile sensing. Tactile sensing is the ability of a system to measure information arising from physical interaction with its immediate environment. These include static & dynamic force/torque sensing, vibrations sensing and thermal sensing. To fulfill these requirements, numerous types of sensors have been developed, which include but not limited to piezoresistive sensors, piezoelectric sensors, capacitive sensors and hall effect based sensors.

With any of the above sensors, it is necessary to accomplish mainly three tasks; at least one, if not all. These include contact point localization, dynamic sensing and tactile force measurement. These functionalities play a crucial role when developing human like grasping and manipulation capabilities. However, many problems arise during the design and manufacturing of these sensors due to the complexity of design, cost and difficulties in practical implementation due to size.

In order to overcome these difficulties and fulfill the above mentioned requirements, this thesis presents a tactile gripper that has been developed based on hall effect. An array of magnets and hall sensors create a unique combination of outputs for each different deformation of the dual layered silicon elastomer which houses the magnets. While allowing the interaction with non-planar surfaces due to the compliant nature of the silicon material, the sensor also facilitates accurate force recognition and contact localization using sensor readings and geometric properties of the silicon layer.

This tactile gripper can be used for object manipulation and many other forms of tactile sensing requirements with necessary modifications. Several experiments have been carried out to test and validate the operation of the sensor with successful results.

This thesis aims to provide the entire design and development of the sensor & gripper, experimentation process, results, limitations and possible future improvements to the reader with the expectation that this development will aid current research in research community and industry. The end goal is to contribute to the process of developing tactile sensors which aids the progression of robotics technology that plays a crucial role in modern scientific advancement.

Keywords-parallel gripper, hall sensor array, flexible silicon elastomer, tactile force sensing

DEDICATION

This dissertation is dedicated to my parents, to whom I can trace my every success to.

ACKNOWLEDGMENTS

First and foremost I offer my sincerest gratitude to my supervisor, Dr. Damith Chathuranga, who has given me the opportunity to follow my M.Sc. in University of Moratuwa and who supported me throughout my thesis with his patience and knowledge whilst allowing me the room to work in my own way. I attribute the level of my Masters Degree to his encouragement and effort and without him this thesis too, would not have been completed or written. One simply could not wish for a better or friendlier supervisor.

Besides my supervisor, I would like to thank Mr. Asitha Kulasekara, my progress review committee: Dr. Buddhika Jayasekara, Dr. Manoj Ranaweera for their insightful comments and encouragement and for the hard questions they have asked which encouraged me to widen my research from various perspectives.

Special gratitude must be given to my lab members in Computational Sensing and Smart Machines Laboratory, Department of Mechanical Engineering; Chanaka Prasad, Rancimal Binoy and to members of Bionics Laboratory, Department of Mechanical Engineering; Sanka Chandrasiri, Isuru Ruhunage and Achintha Mihiran. Gratitude must also be given to the staff of the Machine Workshop in Department of Mechanical Engineering and Mr. Janaka Mangala, Mr. Janath Priyankara at the Die and Mold Center of Department of Mechanical Engineering.

Finally, I thank my wife and parents for supporting me throughout this study at University.

TABLE OF CONTENTS

Declaration	i
Abstract	ii
Dedication	iii
Acknowledgments	iv
Table of Contents	viii
List of Figures	xiii
List of Tables	xiv
Abbreviations	xv
1 Introduction	2
1.0.1 Objectives of the Thesis	3
1.0.2 Contributions of the Thesis	4
1.0.3 Thesis Overview	4

2	Literature Review	6
2.1	Capacitive Tactile Sensors	7
2.2	Magnetic Sensors	16
2.2.1	Hall Effect	16
2.2.2	GMI (Giant magneto impedance)	18
2.2.3	Electromagnetic Induction	19
2.3	Optical Tactile Sensors	23
2.4	Piezoelectric Tactile Sensors	27
2.5	Piezoresistive Tactile Sensors	30
2.6	Tactile Super-resolution	34
2.7	Grippers	36
2.7.1	Classification of grippers	36
2.7.2	Grippers used in known environments	38
2.7.3	Grippers used in unknown environments	39
2.8	Research Gap	39
2.9	Proposed Characteristics of the Tactile Sensor	40
3	Design of the proposed tactile sensor array	41
3.1	Application of Transduction Principle	41
3.2	Design Criteria	43

3.2.1	Elastomer	43
3.2.2	Magnet Array	50
3.2.3	Hall Sensor Array	54
3.2.4	Aluminum Container	56
3.2.5	Design of the Amplifier	57
3.2.6	Signal Analysis and Processing	63
3.3	Design of the Parallel Jaw Gripper	72
3.4	Hardware Setup	72
4	Characterization of the sensor array	76
4.1	Calibration Setup	76
4.2	Experimentation Procedure	78
4.2.1	Displacement Step Method	80
4.2.2	Force Step Method	80
4.3	Analysis	87
4.4	Drift and Noise Characteristics	88
4.5	Super-resolution	92
5	Conclusion and Future Directions	97
5.1	Conclusion	97
5.2	Future Directions	98

List of Publications	100
Bibliography	114
A Appendix	115
A.1 Firmware of Sensor - Data Acquisition & Processing: Teensy 3.6 .	115

LIST OF FIGURES

2.1	Textile based capacitive tactile sensor developed by Sergio et al.	9
2.2	CMOS Micromachined Capacitive Tactile Sensor developed by Ko et al.	10
2.3	Tactile fingertip developed by Schmitz et al.	11
2.4	Shear force sensing capacitive tactile sensor designed by Shashank et al.	12
2.5	Prototype board with above sensor implemented	12
2.6	Parallel plate capacitor with onion epidermal cells as the dielectric layer by Chen et al.	13
2.7	3D force sensing tactile sensor developed by Dobrzynska et al.	14
2.8	3D force sensing tactile sensor developed by Liang et al.	14
2.9	3D force sensing tactile sensor developed by Charalambides et al.	15
2.10	Basic principle behind hall effect based tactile sensors	16
2.11	Robotic hand with the sensor developed by Kyberd et al.	17
2.12	Flexible tactile sensor developed by Jamone et al.	18
2.13	Hall effect based sensors fixed on fingertips and phalanges by Paulino et al.	18

2.14	The nanocomposite based cilia tactile sensor	19
2.15	Multi-functional sensor developed by Li et al.	20
2.16	Tactile sensor with a LC filter developed by Futai et al.	21
2.17	CMC based tactile sensor developed by Chen et al.	21
2.18	Tactile sensor with fingerprint shaped surface developed by Chen et al.	22
2.19	Electro-magnetic induction based tactile sensor for 3D force mea- surement developed by Takenawa et al.	23
2.20	Electro-magnetic induction based tactile sensor with sandwiched layers developed by Wattanasarn et al.	23
2.21	Optical tactile sensor developed using conical feelers method by Ohka et al.	24
2.22	Optical tactile sensor for underwater applications developed by Tan et al.	25
2.23	Three axis optical tactile sensor developed by Kobayashi et al. . .	26
2.24	Optical tactile sensor array developed by Xie et al.	26
2.25	Optical tactile sensor with rod structure developed by Ahmadi et al.	27
2.26	MEMS based 3D force sensor developed by Kim et al.	28
2.27	Piezoelectric tactile sensor for MIS developed by Sokhanvar et al.	28
2.28	Bio-mimetic piezoelectric tactile sensor array developed by Wettels et al.	29
2.29	Piezoelectric tactile sensor array developed by Liu et al.	29

2.30	Flexible piezoelectric transducer array developed by Seminara et al.	30
2.31	Three axis tactile sensor developed by Wen et al. - Sensing Beam	31
2.32	Three axis tactile sensor developed by Wen et al. - Sectional Views	32
2.33	CNT–PDMS composite-based tactile sensor developed by Pyo et al.	33
2.34	Modular tactile sensor developed by Schurmann et al.	33
2.35	Force Sensing Resistor array developed by Heever et al.	34
2.36	Capacitive tactile sensor array developed by Lepora et al.	35
2.37	Super resolution based applications of the above sensor	35
2.38	2-jaw and 3-jaw Grippers	37
2.39	4DOF sensorised surgical forceps for MIS developed by Kim et al.	39
3.1	Basic design of the proposed tactile sensor	42
3.2	Exploded view of the sensor	44
3.3	3D Model of Outer Layer	46
3.4	3D model of Intermediate layer	47
3.5	3D Model of Inner Layer	48
3.6	Exploded view of the elastomer	48
3.7	Sectional view of the elastomer	49
3.8	3D Model of the mold for outer layer	49
3.9	3D Model of the mold for intermediate layer	50
3.10	3D Model of the mold for inner layer	51

3.11	Steps in developing the elastomer	51
3.12	3D Model of the simulated setup	52
3.13	Simulation Results–no load	53
3.14	Simulation Results–full load	54
3.15	ss39et sensor in SOT-23 package	55
3.16	Circuit for one hall sensor	56
3.17	Hall sensor array	56
3.18	Exploded view of the complete construction	58
3.19	Typical arrangement for a Differential Operational Amplifier	60
3.20	Op-Amp circuit for one hall sensor	61
3.21	Op-Amp Array for Tactile Sensor	62
3.22	Signal output waveforms from sensor	65
3.23	FFT for hall sensor output	66
3.24	Filtered signal from sensor output	69
3.25	Parallel Jaw Gripper - Assembled View	72
3.26	Parallel Jaw Gripper - Exploded View	73
3.27	Hardware setup	74
3.28	The complete experimental setup	75
4.1	A taxel	77
4.2	Universal Testing System	78

4.3	Tactile Sensor fixed to the Universal Testing Machine	79
4.4	Using the Universal Testing Machine to Characterize the Tactile Sensor	81
4.5	Sensor Reading, Load Cell Reading vs. Time: Displacement Step Method	82
4.6	Sensor Reading, Load Cell Reading vs. Time: Force Step Method	83
4.7	Sensor Reading vs. Load Cell Reading: Displacement Step Method	84
4.8	Sensor Reading vs. Load Cell Reading: Force Step Method	85
4.9	Generalized Characterization for the Sensor	86
4.10	Acquisition and Recording of Data	87
4.11	Sensor Drift - No load	91
4.12	Sensor Drift - 0.5N Force	92
4.13	Actual location of contact vs. Gap between taxels	93
4.14	Tactile image	94
4.15	Graphical User Interface	96

LIST OF TABLES

2.1	Properties of the mechanoreceptive afferents of glabrous skin of the human hand	7
2.2	Transduction techniques and their relative advantages and disadvantages	8
4.1	Tactile Sensor: Hysteresis values of each taxel	89
4.2	Tactile Sensor: R-Squared values of regression lines	89
4.3	Coefficients list for the quadratic regression functions obtained for loading and unloading phases of displacement step method	90
4.4	Coefficients list for the quadratic regression functions obtained for loading and unloading phases of force step method	90
4.5	Hysteresis and R-Squared values calculated from the mean of all data	91
4.6	Coefficients of the quadratic regression function obtained using the mean of all data	91

LIST OF ABBREVIATIONS

CNC Computer Numerical Control

DC Direct Current

Vdc DC Voltage

PDMS Polydimethylsiloxane

CNT Carbon Nano Tubes

EMI Electromagnetic Induction

EMF Electromotive Force

PVDF Polyvinylidene fluoride

PVDF-TrFE poly[vinylidene fluoride-co-trifluoroethylene]

CCD Charge-Coupled Device

CMOS Complementary Metal-Oxide-Semiconductor

SEM Scanning Electron Microscope

CMC Carbon Micro Coils

MIS Minimally Invasive Surgery

FFT Fast Fourier Transform

SNR Signal-to-Noise Ratio

CoG Center of Gravity

PCB Printed Circuit Board

IC Integrated Circuit

SOT Small Outline Transistor

VCC Supply Voltage

GND Ground Connection

SIL Single in Line

THT Through Hole Technology

SMT Surface Mount Technology

ADC Analog to Digital Converter

op-amp Operational Amplifier

EMA Exponential Moving Average

RMSE Root Mean Square Error

GUI Graphical User Interface

USB Universal Serial Bus

INTRODUCTION

Humans have a remarkable ability in handling objects with various kinds of shapes. The system is so sophisticated that they can perform a multitude of tasks with these objects without giving much attention to how they have to move their arms, hands and fingers.

A system known as the human tactile system is responsible for providing the feedback necessary from fingers to perform such tasks. The mechanoreceptors (nerve endings on finger tips) can detect tactile forces (forces created by physical contact with the target object) and slip (relative movement between finger tips and objects).

These mechanoreceptors are divided into sub categories such as FAI & FAII and SAI & SAII based on their response speed. Each of them have specific functions such as the stimuli they are responsive to. Through this method, the human finger tip is able to provide tactile feedback in multiple domains enabling object manipulation capabilities that currently surpass that of all machinery combined.

The robotic tactile system is an artificial adaptation of the human tactile system aiming to implement similar functionality on robotic systems. They are developed using various technologies such as piezoresistive, piezoelectric, capacitive, optical etc. They are capable of detecting tactile forces & slip, surface texture discrimination and other functionalities that can roughly approximate human capabilities.

Robotic grippers are the mechanical means of actuating a tactile sensing system to perform its task. They are used to impose the sensors on an object by implementing the sensing system on human like fingers or jaws. With multiple applications in industrial, research and service robotics domains, they come in various configurations such as two finger, multi-finger and some odd adaptations capable of dynamic shape manipulation.

The grippers when fixed with tactile sensors can perform the measurement of tactile forces, contact pressures, vibrations, changes in temperature and so on. They have enabled the development of full scale robotic systems that can be deployed for production, service, military, aerospace and research applications.

1.0.1 Objectives of the Thesis

- Design and development of a tactile gripper
- Characterization of tactile sensors of the gripper

A servo operated parallel jaw gripper is developed with mounting facilities for the tactile sensors. Aluminum is used as the construction material due to its light weight, strength and durability. Tactile sensors are also developed with an aluminum housing. It contains a 4×4 array of taxels and means for external connectivity.

Characterization of the sensor is done using a Universal Testing Machine. The sensor is mounted on the test bed and forces were imposed on each taxel using the load cell of the machine. Multiple readings were taken and used for characterization of the sensor.

1.0.2 Contributions of the Thesis

Research work presented in this thesis addresses the development and characterization of a tactile array sensor for parallel grippers for use in object manipulation. The developed sensor contains a 4×4 array of taxels each using a commercial hall sensor and a magnet embedded in a silicon elastomer. It performs the tasks of tactile force measurement, tactile image generation and contact localization.

Its ability to perform tactile force measurement is tested using a calibration setup equipped with a Universal Testing Machine. The correlation between sensor output and testing machine's load cell output has been studied. Also tactile image generation and contact localization has been tested with a Graphical User Interface (GUI) built for the sensor.

1.0.3 Thesis Overview

The thesis consists of four other chapters to elaborately present the research work carried out related to the topic. Contents of each chapter can be summarized as below.

Chapter 2 discusses the design and functionality of most of the existing tactile sensors & grippers in both research and commercial stages. Several types of transduction principles, their implementation in tactile sensors, advantages and disadvantages of each of them are also discussed. The types of available grippers, methods of actuation and their usage are discussed at the end of this chapter.

Chapter 3 discusses the transduction principle, its application in the research and methods of integration in the tactile sensor array. It also describes the physical construction of the tactile gripper, fabrication processes, design of the amplifier circuit and firmware.

Chapter 4 discusses the mapping of actual applied forces to hall sensor read-

ings. Details of the experimentation setup, experimentation procedure, analysis of the data and findings are discussed in separate subsections. A possible functionality of the device, the potential to apply a super-resolution algorithm is also discussed.

Final chapter of this thesis presents the conclusion of research work carried out. It also discusses the limitations of the sensor and possible future directions for this research to progress.

LITERATURE REVIEW

Tactile Sensing is a broad field of research spanning a multitude of technologies and applications. While its primary goal is to deduce information on physical contact between sensor surface and external objects, the implications are far reaching. The magnitude of progression in this technology during the past decade stands as a witness for this [1].

The ability of a tactile sensing system to provide a 'Sense of Touch' [2] to a functional robotics system enables major improvements to its ability on handling objects. It also enhances and refines its capabilities in interacting with an uncertain external environment. This applies to all types of robots alike and especially to humanoids.

The inspiration for tactile sensing is obtained through the tactile sensing system of human hand. The glabrous skin of human hand is made up of four mechanoreceptors that are sensitive to stretching and compression of skin [3]. The receptors can be categorized as Rapidly Adapting or Fast Adapting (RA or FA) & Slowly Adapting (SA) and each as Type I & II depending on their functionality.

The rapidly adapting type has almost no response to static deformation of skin, but responds rapidly to dynamic variations of skin deformation. On the other hand slowly adapting type shows less sensitivity to dynamic deformations, but responds readily to deformations that are more static or slowly changing. They can also be categorized based on their receptive field, where type I denotes

Receptor type	Receptive field area (mm ²)	Frequency range (peak sensitivity) (Hz)	Amplitude threshold for vibration (mm)	Effective stimulus
RAI	1–100	1–300(50)	2	Skin motion
SAI	2–100	0–100 (5)	30	Edges, points, corners
RAII (PC)	10–1000	5–1000 (250)	0.01	Vibration
SAII	10–500	<8 (0.5)	40	Skin stretch

Table 2.1: Properties of the mechanoreceptive afferents of glabrous skin of the human hand [3]

sensors with a smaller receptive field and vice versa. Refer to Table 2.1

In order to mimic the behavior of mechanoreceptors mentioned above, technologies have been developed in multiple forms [4]. Capacitive, Piezoresistive, Piezoelectric, Optical & Magnetic are to name a few of such technologies. They have distinct advantages and disadvantages over each other depending on their application. Refer to Table 2.2.

2.1 Capacitive Tactile Sensors

Capacitive tactile sensing is a popular choice among researchers due to its attractive features and ease of construction. Multitude of research have been carried out using this technique with several innovations.

Capacitive tactile sensors employ the concept of electrical capacitance and its variation to measure static and dynamic forces. Electrical capacitance is the ability of two electrodes to sustain an electric charge when being separated by a thin dielectric material. The effect depends on factors like material used for dielectric and distance between electrodes.

When the distance between electrodes change, so does the capacitance. Capacitive tactile sensors exploit this fact by allowing tactile forces to be applied

Transduction technique	Modulated parameter	Advantages	Disadvantages
Capacitive	Change in capacitance	Excellent sensitivity Good spatial resolution Large dynamic range	Stray capacitance Noise susceptible Complexity of measurement electronics
Piezoresistive	Change in resistance	High spatial resolution High scanning rate in mesh Structured sensors	Lower repeatability Hysteresis Higher power consumption
Piezoelectric	Strain (stress) polarization	High frequency response High sensitivity High dynamic range	Poor spatial resolution Dynamic sensing only
Inductive LVDT	Change in magnetic coupling	Linear output Uni-directional measurement High dynamic range	Moving parts Low spatial resolution Bulky Poor reliability More suitable for force/torque measurement applications
Optoelectronic	Light intensity/spectrum change	Good sensing range Good reliability High repeatability High spatial resolution Immunity from EMI	Bulky in size Non-conformable
Strain gauges	Change in resistance	Sensing range Sensitivity Low cost Established product	Calibration Susceptible to temperature changes Susceptible to humidity Design complexity EMI induced errors Non-linearity Hysteresis
Multi-component sensors	Coupling of multiple intrinsic parameters	Combination of advantageous parameters	Discrete assembly Higher assembly costs

Table 2.2: Transduction techniques and their relative advantages and disadvantages [5]

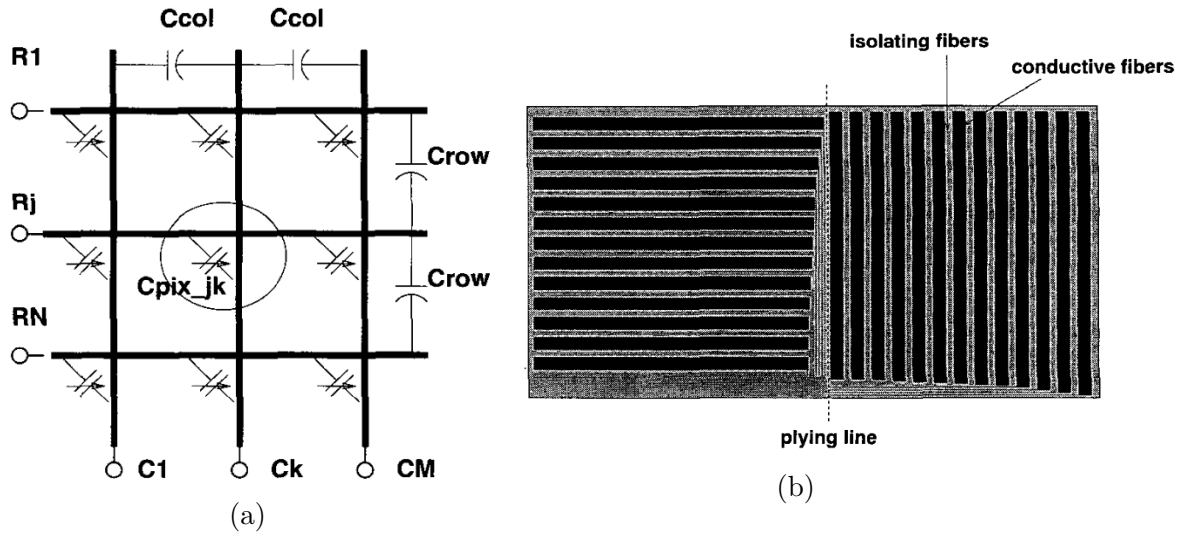


Figure 2.1: (a) Arrangement of capacitive sensors over the fabric (b) Pattern of conductive fibers on fabric [6]

on the electrodes of the capacitor thus varying their separation. The resulting change in capacitance can be correlated with the actual forces being applied.

A basic example for this technology can be seen in the textile based capacitive tactile sensor developed by Sergio et al. [6]. They have used a passive array of capacitors distributed over a piece of fabric. The capacitors are built by separating a pattern of conductive stripes (on each fabric) using a dielectric material.

When pressure is applied, the dielectric material is compressed between the fabrics creating variations in capacitance. Scanning over the entire array will reveal this change in capacitance allowing to identify the pressure being applied. Refer to Figure 2.1.

A more improved approach has been taken by Shkel et al. [7] using a solid state capacitor. The capacitor has an elastic dielectric and has been tested for normal loads against capacitors with an air gap as the dielectric material. The authors claim that their capacitor provides higher sensitivity, large measurement range and strong signal output.

An interesting research has been carried out by Arshak et al. [8] with a mod-

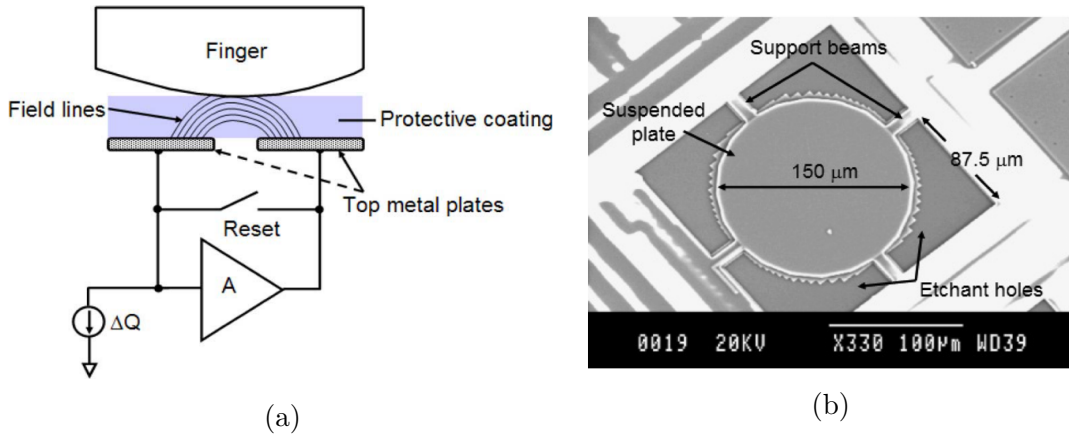


Figure 2.2: (a) Schematic of one pixel cell of the capacitive fingerprint sensor (b) SEM of the fabricated tactile sensor [9]

ified dielectric layer. They have used a silicon material dispersed with carbon black as the dielectric material for the capacitor. This will change the electrical characteristics of the material, improving its permittivity. The result is a capacitive sensor with improved sensitivity. The effect tends to increase with the increase of carbon loading.

Ko et al. [9] have developed a Complementary Metal-Oxide Semiconductor (CMOS) Micromachined Capacitive Tactile Sensor to be used for finger print reading. This research was carried out during a period where capacitive finger print readers were uncommon. Optical finger print reading mechanism lacked robustness. It wouldn't respond well for stained fingers, cannot withstand vibrations, were bulky and prone to frequent malfunctions. Often they could be fooled with an identical printed media of the same finger print reducing its applicability for security needs.

This research introduces a MEMS based capacitive sensor micro-machined on a silicon wafer which aim to mitigate the above mentioned disadvantages. Refer to Figures 2.2.

Another development on this methods has been done by Salo et al. [10], where CMOS based micro-machining has been applied to develop medical tactile sen-

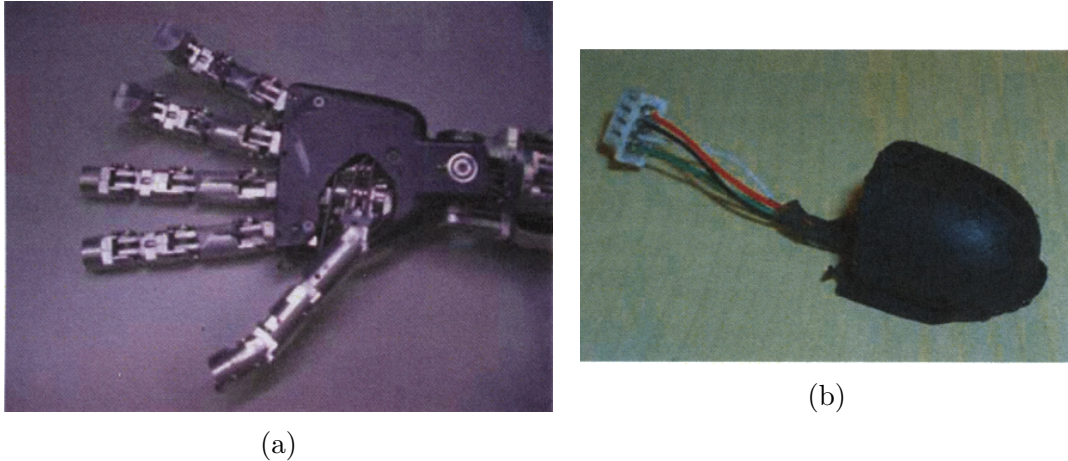


Figure 2.3: (a) A hand of the humanoid robot iCub (b) A picture of the first version of the fingertip [11]

sors. They have tried two processes to develop the capacitor, namely sacrificial etching of aluminum or silicon dioxide. While sacrificial silicon dioxide etching results in reliable dielectric gap formation, it also resulted in large variations of stress properties, which made them inferior to membranes resulted from sacrificial aluminum etching.

A noticeable development has been made by Schmitz et al. [11] where a capacitive pressure sensor is integrated into a finger tip. The capacitive sensor has 12 sensing zones, and are naturally shaped and distributed over the fingertip area of the humanoid robot iCub.

The fingertip is made out of silicone, which makes it soft and compliant with external surfaces. The electronic circuitry to perform A/D conversion is also built into the fingertip, reducing the number of wiring and noise related issues. They have tested the first prototypes with successful results. Refer to Figure 2.3.

Using the separation distance between two electrodes to measure tactile forces has the default implication that normal loads would be imposed on the capacitor plates to cause that variation. As tactile sensing requires a comprehensive description of the forces being applied, such a simple model would not suffice. Shashank et al. [12] have tried to address this issue by developing a capacitive

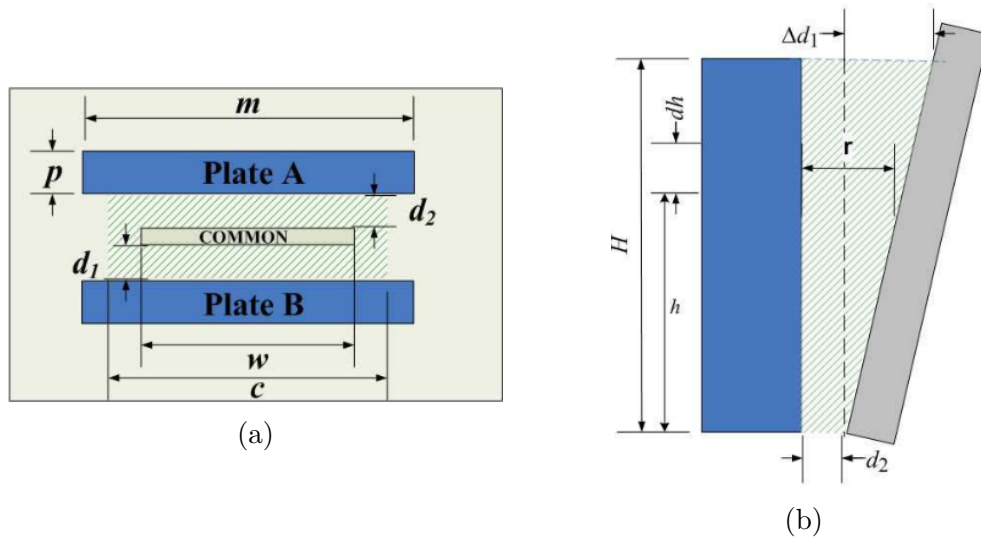


Figure 2.4: (a) The structure of the shear force sensor from top view (b) Partial side-view of the sensor showing one plate and a displaced common plate due to shear force [12]

tactile sensor that can detect shear forces.

The arrangement has two capacitive plates made by PCBs. In between them is a common plate that can move according to shear forces being applied. The arrangement is enclosed in a silicon coating to be held together.

Shear forces will displace the common plate, causing changes in the differential capacitance, which in turn can be used to characterize the magnitude of the forces being applied. However this sensor is only functional along one axis. The authors expect to refine the design to allow the detection of shear forces along two perpendicular axes. Refer to Figures 2.4 & 2.5.



Figure 2.5: Prototype board with sensor [12]

An interesting approach has been taken by Chen et al. [13] in substituting various materials for the dielectric layer. They have used a single layer of onion epidermal cells as the dielectric layer for a parallel plate capacitor to create a 4×4 array of tactile sensors. Their sensor has good sensitivity and linearity and can be used for biomedical and electronic skin applications. Refer to Figure 2.6.

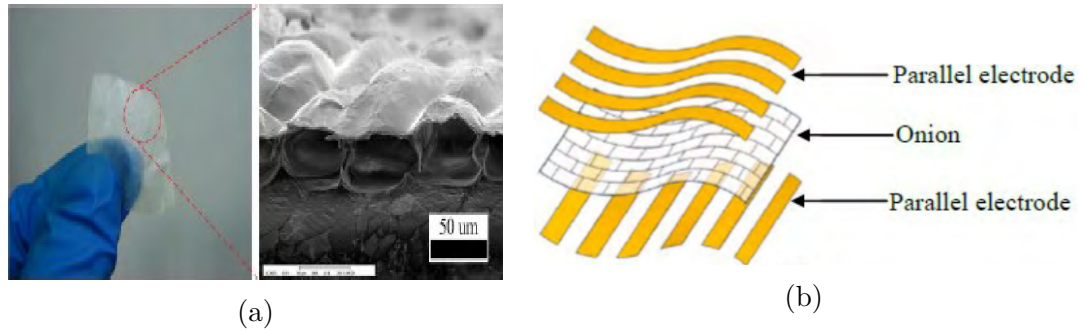


Figure 2.6: (a) Transparent onion epidermal cell layer as the dielectric material (b) Schematics of the tactile sensor array with the onion epidermal cell layer sandwiched between row and column electrodes [13]

In capacitive tactile sensors, a major limitation is the number of axes the sensor is responsive to. It is usually limited to one axis (normal loads) and occasionally to two axes (two shear stress directions). However, its lack of ability to sense tactile forces in all three directions severely hinder its applications in many practical scenarios.

Dobrzynska et al. [14] have created a tactile sensor that is responsive in all three perpendicular directions using finger shaped electrodes. The simulated model of the sensor comprises of finger shaped top and bottom electrodes and a dielectric layer made with a novel combination of polymers. These characteristics make the sensor very flexible and markedly sensitive to shear forces as well as normal loads. Refer to Figure 2.7.

It has been demonstrated by Tee et al. [15] that a patterned micro-structure on a dielectric layer can vastly improve the characteristics of capacitive tactile sensors. Through finite element analysis, they have been able to create pyramid shaped micro-structures on the dielectric layer that can dramatically reduce the

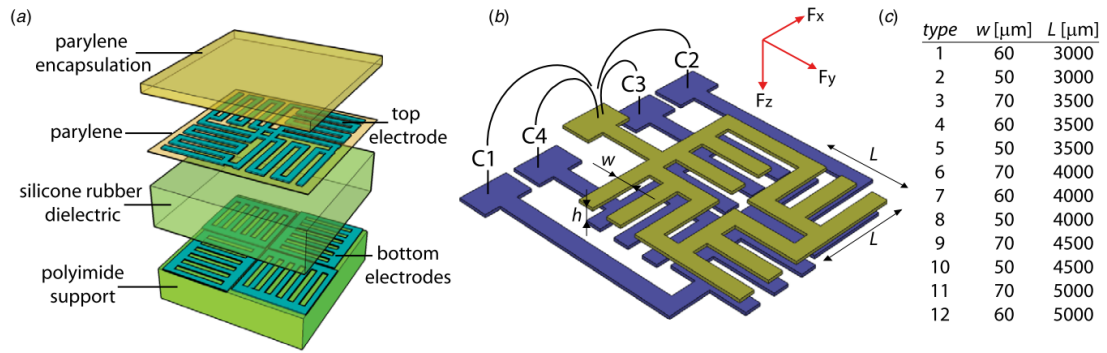


Figure 2.7: (a) Conceptual view of the tactile sensor. (b) Finger shaped electrodes (c) Fabricated sensors with varying geometry design [14]

mechanical modulus of the dielectric layer, thus improving the sensor's flexibility and sensitivity.

Liang et al. [16] have used this concept for developing a tactile sensor that is able to do 3D force measurements. They have in fact used truncated pyramid structures on dielectric layer so that the contact area between the dielectric layer and electrodes is also improved.

The sensor array has been mounted on a prosthetic hand and used for object grasping. The authors have been able to obtain successful results signaling the viability of these sensors being applied for robotics and prosthetic applications. Refer to Figure 2.8.

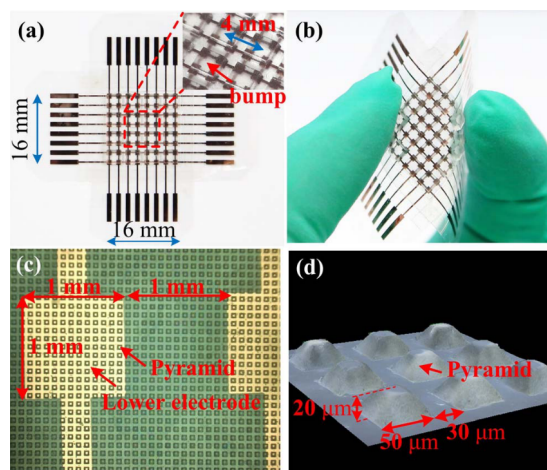


Figure 2.8: (a) The fabricated sensor array (b) bent by hand; (c) the lower electrode layer, and (d) the truncated pyramid array [16]

An interesting development has been made by Charalambides et al. [17], where an all-elastomer 3D force sensing capacitive sensor is built. The electrodes of the MEMS sensor is built using conductive elastomer, created by embedding carbon particles inside of an elastomeric material. Dielectric material will be filled inside electrode gaps, and additional material will seal top and bottom of the sensor for protection.

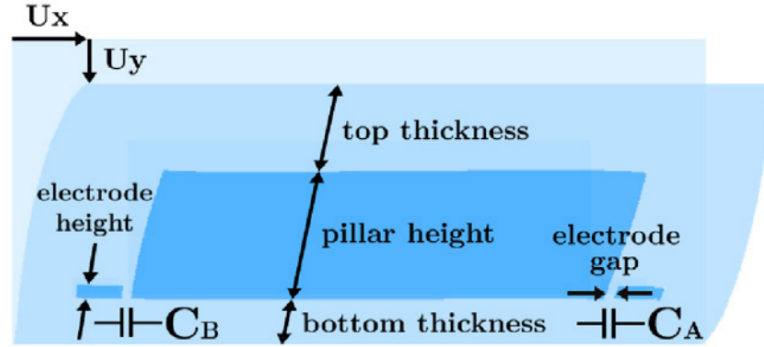


Figure 2.9: Proposed sensor architecture [17]

The pillar in Figure 2.9 deforms in shear direction under shear forces and compresses evenly under normal load. Under shear load, depending on the deformation direction of the pillar, one electrode gap will increase while the other will decrease. The differential capacitance ($C_B - C_A$) correlates with the magnitude of shear force. Electrodes for each direction of shear stress is required.

Under normal load, the compression of the pillar will evenly increase both C_B & C_A which correlates with the magnitude of normal force. The simulation was done with successful results and a micro-fabrication process to develop the sensor is also proposed.

Additionally more improvements that can be made to the dielectric layer [18] and integrating these sensors on industrial grippers [19] have also been investigated.

2.2 Magnetic Sensors

When considering magnetic tactile sensors, there are three categories to concern with namely; Hall Effect, GMI (Giant Magneto Impedance) and Electromagnetic Induction. All three areas have been subject to significant research from which notable research are mentioned below.

2.2.1 Hall Effect

Hall effect is the generation of voltage across a current carrying conductor, transverse to the current propagating direction upon application of some magnetic field. The effect is more pronounced in semiconductors thus commercial hall effect sensors are available in the market for multiple applications.

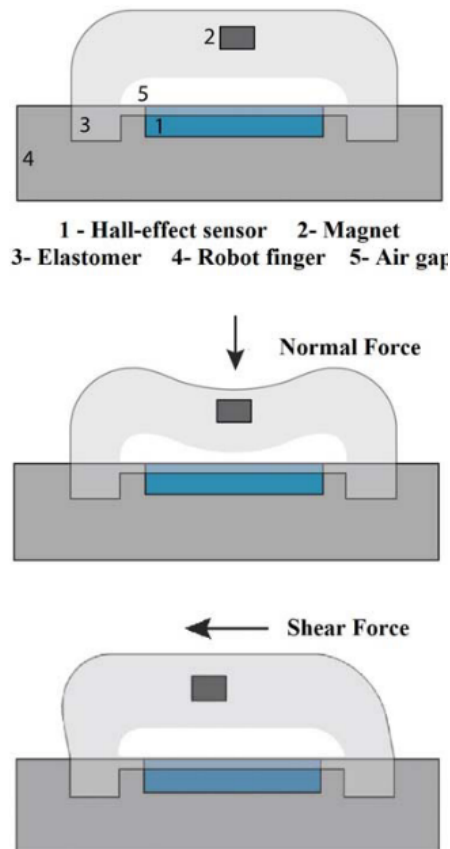


Figure 2.10: Basic principle behind hall effect based tactile sensors [20]

A hall effect sensor can be used to detect the change of a magnetic field usually stemming from the change of position or orientation of a permanent magnet. If some mechanism could be devised so that the position and orientation of a permanent magnet could change based on the applied tactile force, a hall sensor can be used to detect and quantify that force. Refer to Figure 2.10.

One of the first attempts at achieving the above has been made by Kyberd et al. [21] in their force sensor which was then implemented on an artificial robotic hand. Force detection, object slip detection, sensor resolution and reducing sensor's cross sensitivity have been studied. Refer to Figure 2.11.

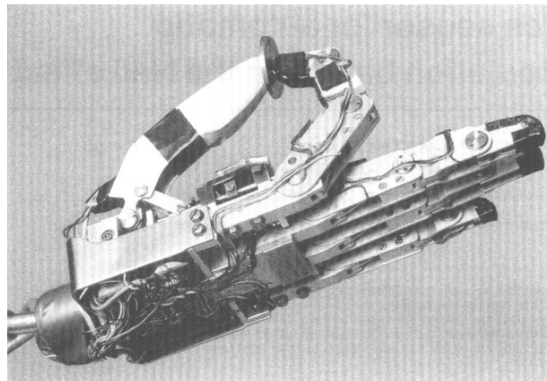


Figure 2.11: Robotic hand with the sensor [21]

A more recent much improved version of the same research was done by Jamone et al. [22] where they have developed a similar sensor (a small magnet embedded inside a soft silicon body is attached to a hall sensor below) and fixed 17 of such tactile sensors to an anthropomorphic robotic hand.

Two types of bodies are developed, one for the tip of the finger, and other for a phalange of the finger. The authors report higher sensitivity, reduced hysteresis and high repeatability than previous designs. Refer to Figure 2.12.

Paulino et al. [20] have further improved this technology by developing a 3-axis tactile sensor that can sense shear forces in both directions and normal loads as well. They have used a 3D hall sensor with a magnet embedded inside a silicon body.

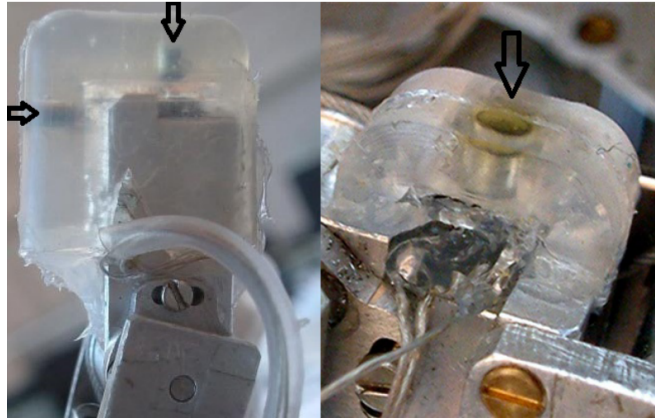


Figure 2.12: Depiction of Sensor, Left: Fingertip Right: Phalanges [22]

The sensor is a low cost and easy to assemble device with multiple applications. It has been developed into several shapes and integrated to the fingertip and phalanges of an anthropomorphic hand for experimentation. The authors have been able to obtain positive results with a minimum sensed force of 7 mN. Refer to Figure 2.13.

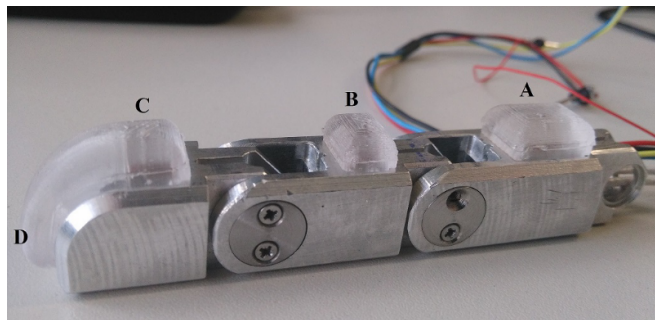


Figure 2.13: Sensors fixed on fingertips and phalanges [20]

2.2.2 GMI (Giant magneto impedance)

GMI is the phenomena displayed by some materials by creating large variations in electrical impedance upon changing magnetic field. Sensors working under this principle can be used to detect magnetic field variation caused by the movement of magnetic material due to application of tactile forces.

Alfadhel et al. [23] have come up with a novel application for this technology. They have created artificial nano-composite cilia embedded in a Polydimethyl-

siloxane (PDMS) layer. The nano-composites are made using iron nano wires that has permanent magnetism. The GMI sensor is placed below this layer.

Application of tactile forces bend the cilia, changing the average magnetic field felt by the GMI sensor. The change in impedance can be used to quantify the tactile forces being imposed on the sensor. This sensor is very sensitive, power efficient, multi-functional and can operate in both air and liquid (can detect liquid forces as well). Refer to Figure 2.14.

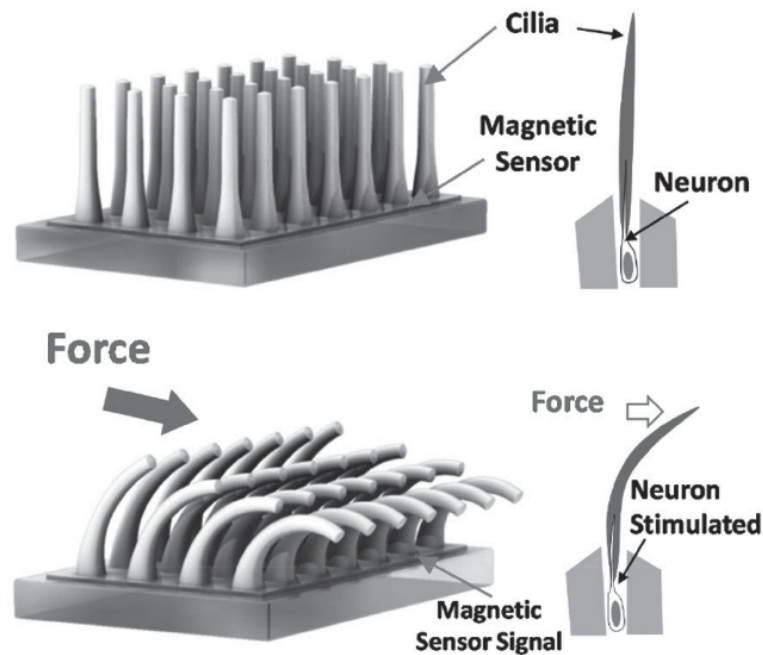


Figure 2.14: The nanocomposite cilia based tactile sensor. The sensor mimics the neuron in natural cilia. [23]

2.2.3 Electromagnetic Induction

Electromagnetic Induction is the phenomena where a change in magnetic field creates an Electro-Motive Force (EMF) in a conductor. A conductor, preferably a coil can be placed in a changing magnetic field usually generated by another set of coils. Tactile forces applied on the conductor may deform it or change its orientation, causing a change in EMF induced in the coil. This differential voltage can be used to quantify the tactile forces being applied.

One of the earliest developments were made by Li et al. [24] where a multi-functional sensor was developed using two spiral shaped conductors. When the two coils are used as electrodes, it has the property of capacitance. When one coils is made to heat up and the other is used as a resistor, it can sense temperature. And when coils are coupled magnetically, they have the property of inductance.

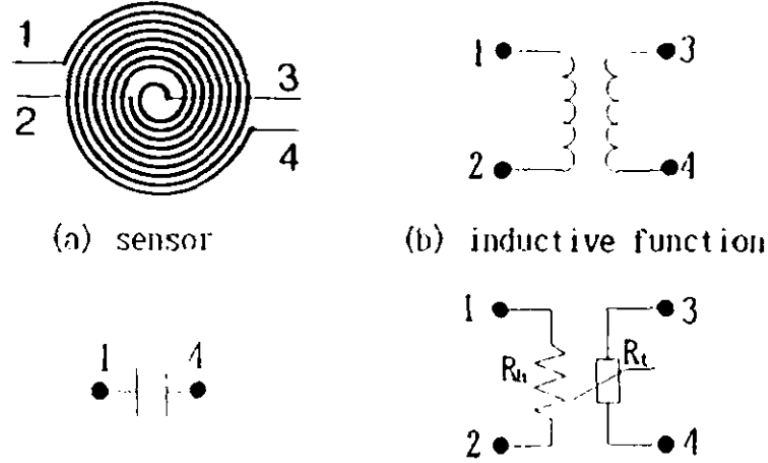


Figure 2.15: Proposed multi-functional sensor [24]

The authors have used the sensor to discriminate between metals. They highlight the sensor's ability to discriminate materials which has implications for artificial skin development. Refer to Figure 2.15.

A novel attempt has been made by Futai et al. [25] by creating a series LC filter as the sensing element. Tactile forces will deform the inductor changing the resonant frequency of the circuit. The trap circuit can measure this change and provide a signal output. Using multi-point acquisition, several sensing elements can be measured at once.

The fabricated sensors were highly robust, highly sensitive and had high repeatability. When connected in series, two electrical lines and one signal frequency could operate the entire system providing simplicity of design and operation. Refer to Figure 2.16.

Chen et al. [26] have extended the same concepts into microscopic region where

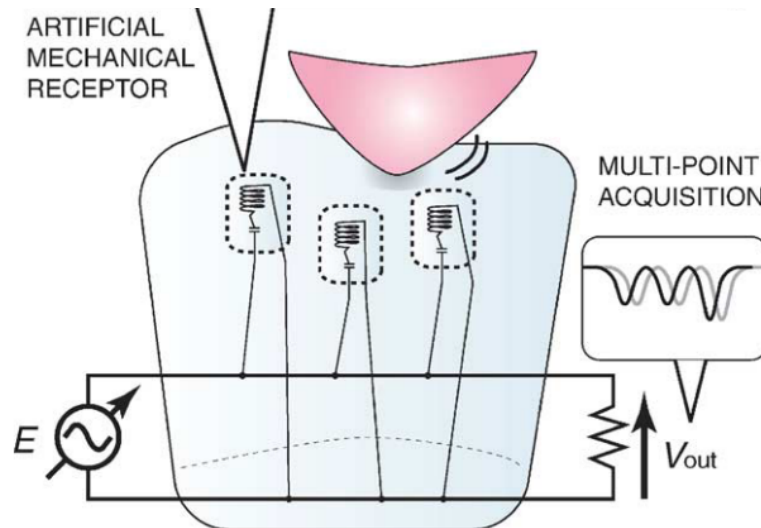


Figure 2.16: Design of the sensor [25]

they have utilized carbon micro-coils (CMCs) made of polysilicone composites. These CMCs change their inductance, capacitance and resistivity based on extension or contraction.

Sensors built using CMCs are multiple orders of magnitude greater than the sensitivity of ordinary tactile sensors and can measure loads in the range of milligrams. They have various applications ranging from medical to aerospace and robotics. Refer to Figure 2.17.

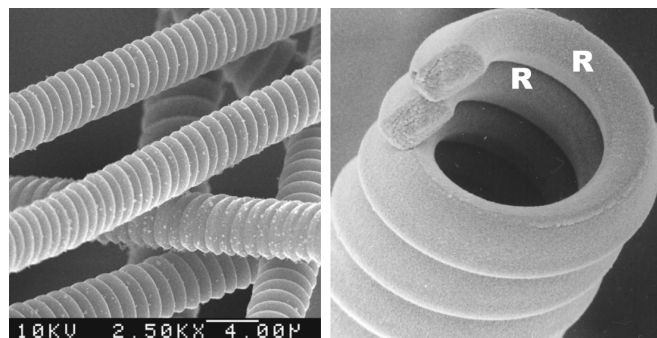


Figure 2.17: SEM of double helix carbon micro-coils: Diameter 4 μ m [26]

Same authors republished with an improved version of the same research [27]. They revised the CMC manufacturing process and created super-elastic CMCs with enhanced properties. These modifications provided improved performance.

Same authors also published a research where they developed the same sensor with fingerprint type surface [28]. This further improved the sensitivity of the sensor. They also found that during the application of dynamic loads, application of such forces in a vertical direction to the epidermal ridges caused a two fold increase of sensitivity to that of in the horizontal direction. Refer to Figure 2.18.

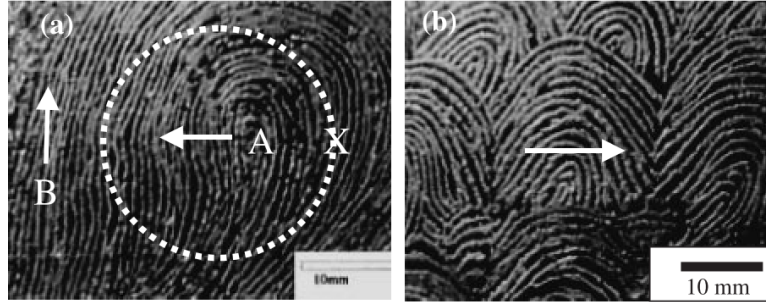


Figure 2.18: Surface morphology of fingerprint-type sensor elements. (a) Single fingerprint, (b) multi fingerprint [28]

An improved method of fabricating CMCs is also developed by Motojima et al. in [29].

Takenawa et al. [30] have proposed a electro-magnetic induction based tactile sensor for 3D force measurement and tactile sensing. The sensor consists of a 2D array of inductors and one permanent magnet embedded inside an elastomeric material.

Tactile forces will deform the elastic body displacing the magnet. This movement is sensed by the inductor array allowing the quantification of tactile forces being applied or slip incurred. Refer to Figure 2.19.

Wattanasarn et al. [31] have developed a tactile sensor based on a similar concept. The sensor contains from top to bottom a bump layer, detection coils (2D array), spacer layer, excitation coils (2D array) and a bottom layer. The layers are made of PDMS substrate.

The bump layer deforms according to shear and normal stresses applied. This deformation causes the detection coils to deform. As they are coupled to the

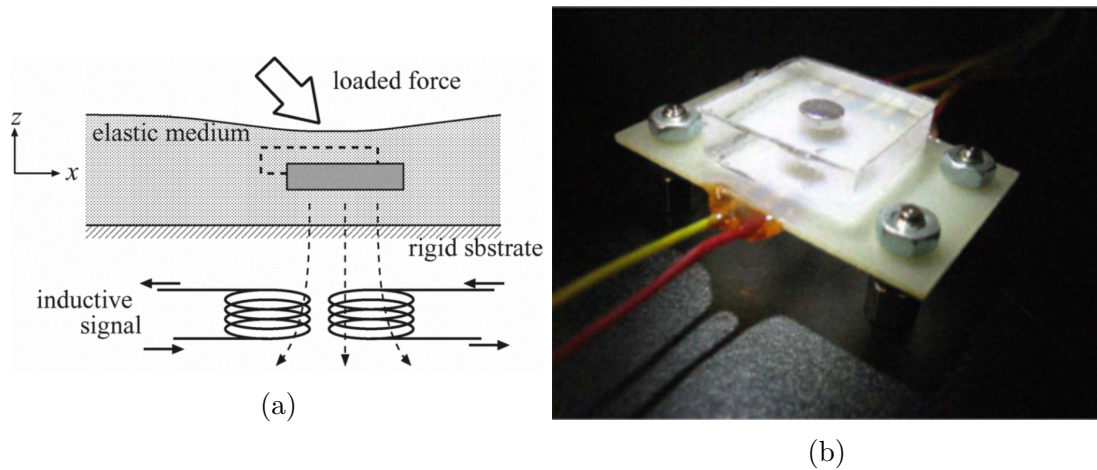


Figure 2.19: (a) Construction of each cell (b) Outlook of actual sensor [30]

alternating magnetic fields being generated from the excitation coils, this deformation will cause a change in the EMF being induced in the detection coils. This change can be used to quantify the tactile forces being applied. Thus the sensor is capable of 3D force measurement. Refer to Figure 2.20.

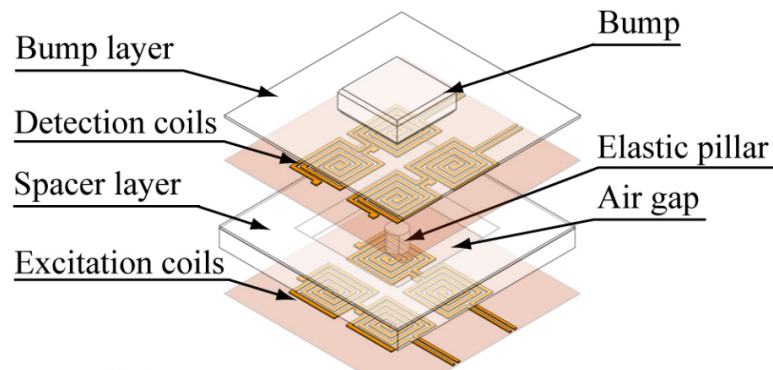


Figure 2.20: Proposed 3D tactile sensor [31]

2.3 Optical Tactile Sensors

Optical tactile sensors utilize the detection of light particles that were reflected or deflected according to some tactile forces being applied. Detection of light is often done using a Charge Coupled Device (CCD) or CMOS device.

Ohka et al. [32] have developed a tactile sensor based on this concept. The

sensor is able to detect both normal and shear forces. The sensor is equipped with a rubber sheet (where forces are applied) and conical feelers below it. These feelers maintain contact with an optical wave guide plate.

Application of normal forces will push down these feelers while shear forces will displace the feelers horizontally. Lights beams reflected from the feelers are captured through a light sensor to measure tactile forces. Refer to Figure 2.21.

Research based on a similar concept have been carried out by Piacenza et al. [33] and Massaro et al. [34].

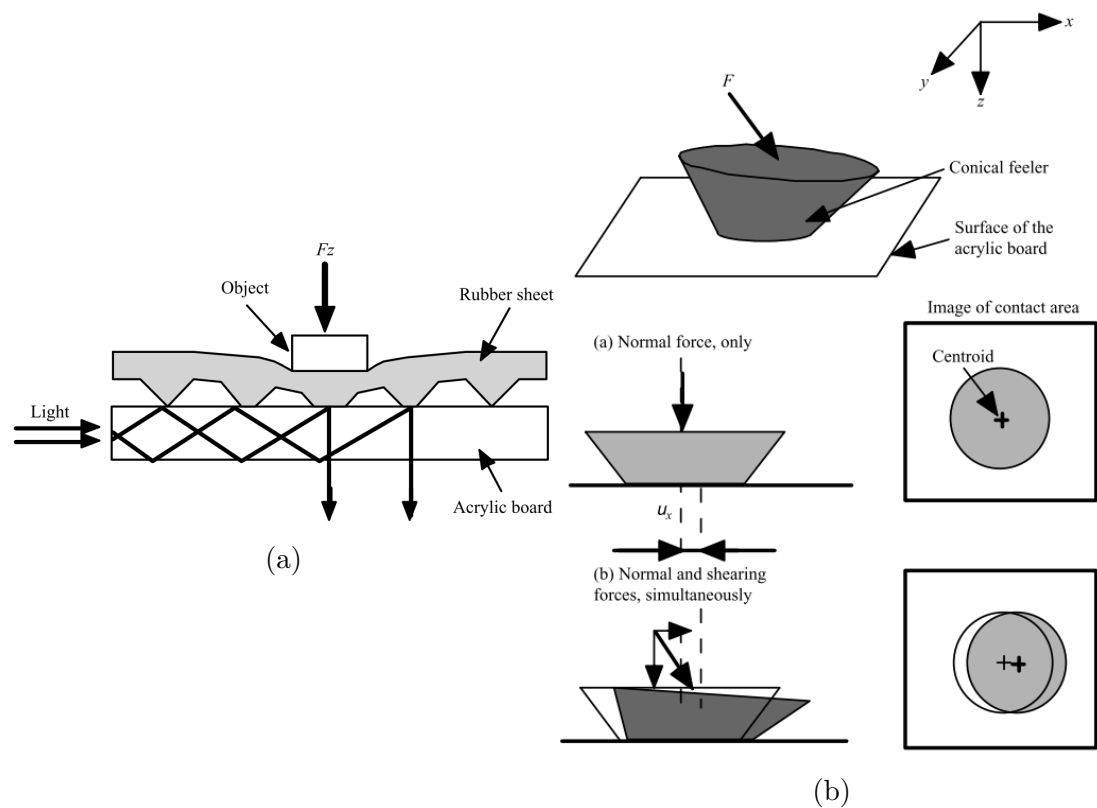


Figure 2.21: (a) Sensing mechanism of the sensor (b) Role of conical feelers [32]

The same authors have also improved the design by incorporating a columnar feeler and a 2×2 array of conical feelers to the sensor [35]. Calibration of the sensor has been done to obtain positive results.

Tan et al. [36] have developed an optics based sensor for underwater applications. Since most of the sensors developed for ground, air or space applications

do not suit underwater applications, this designs proves to be useful.

The sensor utilized a spring based force transfer mechanism and an optical fiber. Tactile forces are transferred to the optical fiber using the mechanical design. These forces cause the optical fiber to deform causing a change in the optical power output. Using the differential amount of power, the magnitude of tactile forces can be calculated. Refer to Figure 2.22.

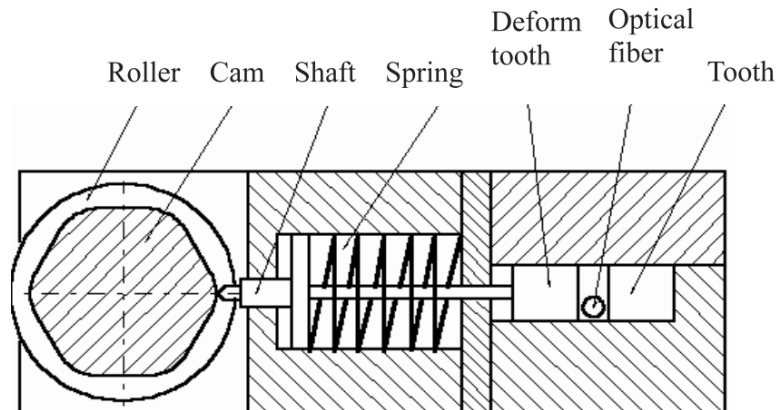


Figure 2.22: Structure of the tactile sensor [36]

Kobayashi et al. [37] have developed a tactile sensor for application on 3 degree of freedom (DOF) robotic hand. The sensor utilizes a concept similar to [35] where the reflected light travels through a optical fiber to a CCD camera. The authors state that the sensor is capable of measuring 3D forces and could be applied for dexterous object manipulation. Refer to Figure 2.23.

Lepora et al. [38] have improved on this concept to obtain tactile perception with increased accuracy. [39] is also a similar research while [40] depicts a possible application of using a CCD sensor for surface roughness measurement.

Xie et al. [41] have come up with a novel method for optical tactile sensing. They have developed a 3×3 array of optical taxels that can be used for Minimally Invasive Surgery (MIS). The system contains a 3×3 array of flexures coupled to a set of mirrors that can change their position and orientation based on the deformation of flexures.

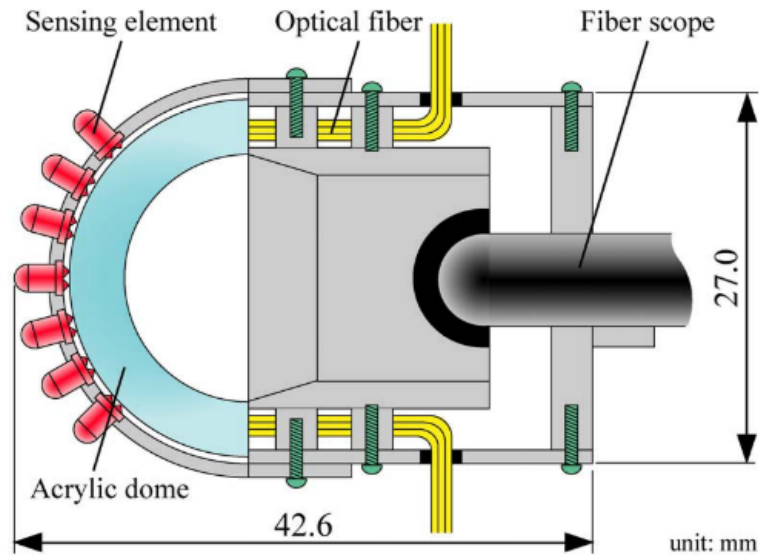


Figure 2.23: Three axis tactile sensor [37]

These mirrors reflect light from a light source to an optical sensor. Any change in light reflection due to tactile forces can be detected and measured by the optical sensor. Refer to Figure 2.24.

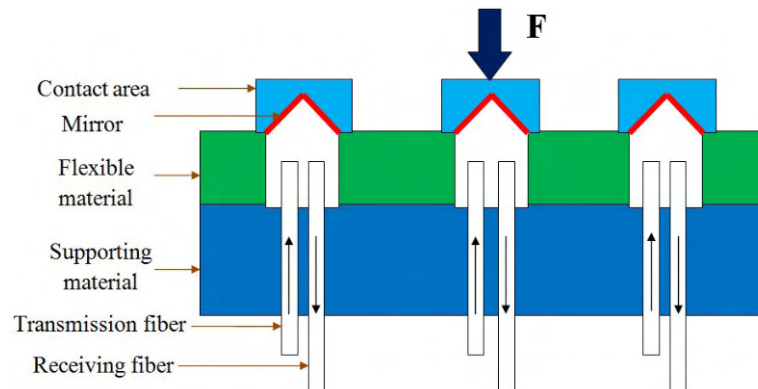


Figure 2.24: Design of the optical tactile sensor [41]

Another noteworthy development in optical tactile sensors for MIS applications is that of developed by Ahmadi et al. [42]. Their sensor is based on the bending of an optical fiber upon contact with a tissue anomaly e.g. a lump. The novel rod structure in the sensor enables accurate localization of the tissue problem without the use of a sensor array. Refer to Figure 2.25.

A similar research is that of done by Fujiwara et al. [43].

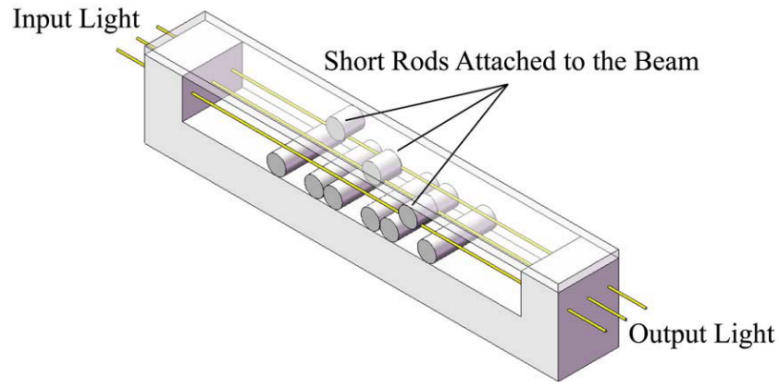


Figure 2.25: The structure of the tactile sensor [42]

2.4 Piezoelectric Tactile Sensors

Piezoelectric tactile sensors utilize the piezoelectric effect. The piezoelectric effect is the ability depicted by piezoelectric materials to generate a voltage potential upon being subjected to mechanical deformation. When the sensing element of a tactile sensor is built using a piezoelectric material, the voltage potential generated by the sensing element can be used to characterize the tactile forces being imposed.

However, the charge generated due to mechanical deformation of a piezoelectric element is only short lived. To sustain the charge potential, the element should be subjected to continuous or cyclic deformation. Therefore this methods is good for dynamic force measurement, but lacks in robustness for static force measurement.

Kim et al. [44] have developed a MEMS based 3D force sensor using this technology. The sensor has a 10×10 array of micro-force sensors capable of measuring 3D forces up to 3N. Each micro-sensor is made using four strain gauges. Refer to Figure 2.26. The size of entire sensor is $10\text{mm} \times 10\text{mm}$.

Major improvements to this research were done by the same authors in 2009 [45].

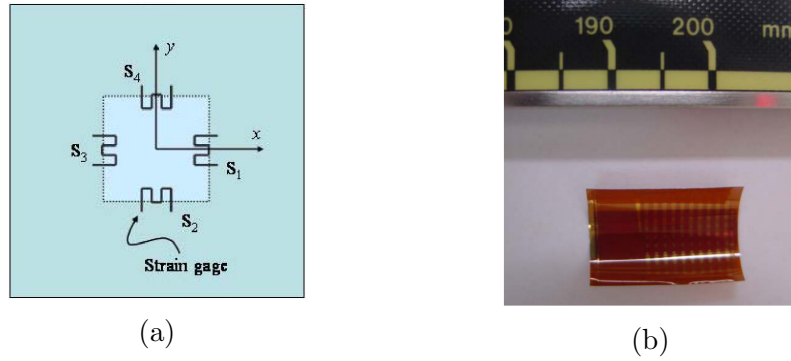


Figure 2.26: (a) A single micro-force sensor with 4 strain gauges (b) Outlook of actual sensor [44]

A popular piezoelectric material used by researchers for developing such sensors is Polyvinylidene Fluoride (PVDF). It results in highly sensitive sensors and is also compatible with micro-machining for MEMS applications. Several research have been conducted using this material for sensor development [46, 47].

Also a piezoelectric material called vinylidene fluoride (VDF) has been introduced that contain advantageous properties over PVDF. It has a higher remnant polarization and piezoelectric coefficient thus suitable for medical applications [48].

MIS is also a potential application field for these sensors. Several research have been conducted under this area for sensor development. A MIS grasper [49] (Figure 2.27), a miniaturized force sensor for tissue anomaly detection [50] and a tactile slip sensor for a tele manipulator [51] have been developed using PVDF fabrication technology.

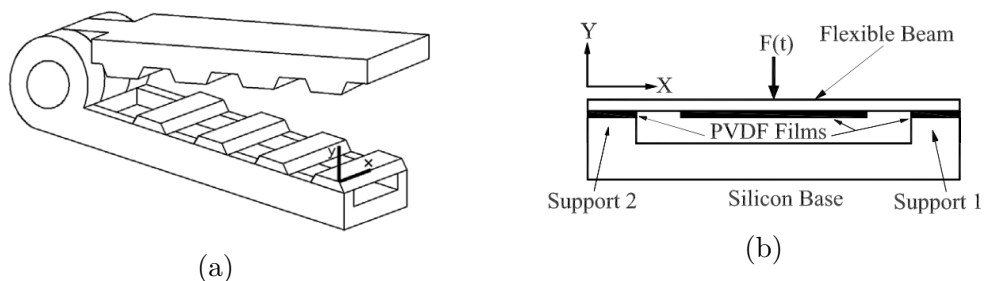


Figure 2.27: (a) Grasper with an array of sensing units (b) Cross section of a sensing unit [49]

Bio-mimetic piezoelectric tactile sensors have also been developed. Wettels et al. [52] have integrated an array of tactile sensing units to a compliant finger tip. They mimic the activity of mechanoreceptors in a human finger tip. Refer to Figure 2.28.

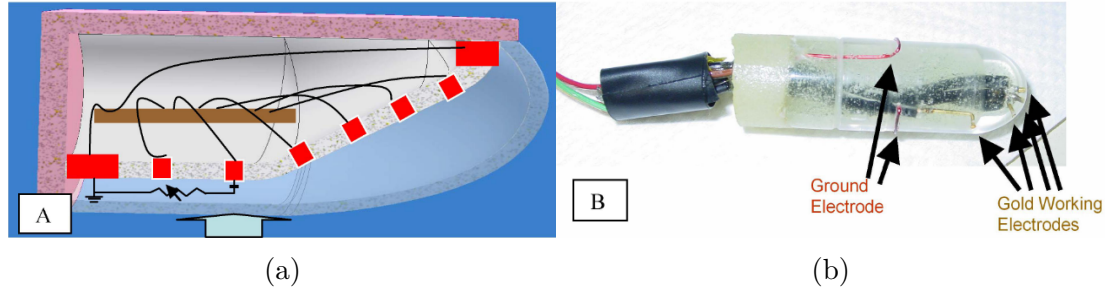


Figure 2.28: (a) Internal structure of finger tip (b) Outer construction [52]

A similar attempt has been made by Liu et al. [53] where a 2×2 array of piezoelectric sensors have been integrated on a finger tip. The authors have used it for roughness encoding under various scanning velocities. Refer to Figure 2.29. Using human like epidermal ridges to enhance the sensitivity of piezoelectric tactile sensors has also been tried [54].

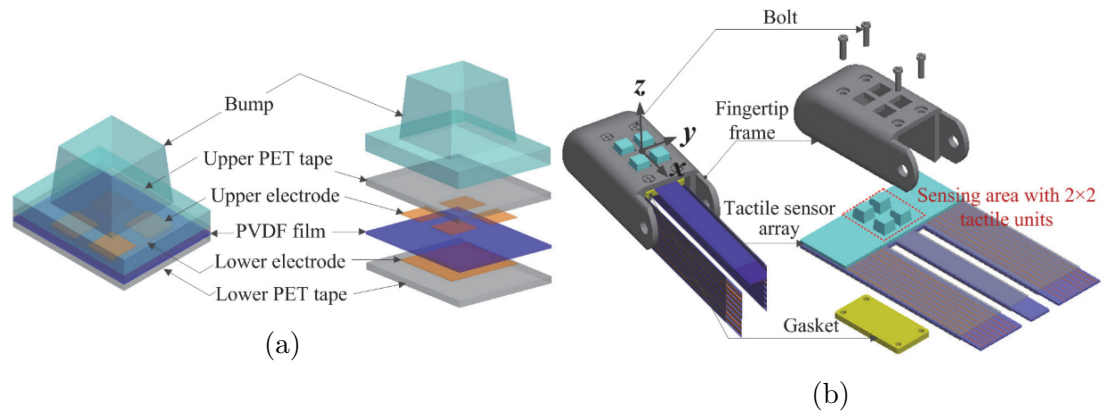


Figure 2.29: (a) Structure of single cell (b) Full Assembly [53]

Also thin film transistor technology has been used to develop ultra-flexible piezoelectric sensors with enhanced properties [55]. Another application of piezoelectric tactile sensing is for artificial skin development. The flexibility, dynamic

range and simplicity in construction delivered by this technology makes it suitable for this purpose.

Sim et al. [56] have developed a tactile sensor that suits for the use in artificial skin development. The sensor is able to categorize a tactile sensation into sharp, blunt, hot or cool categories. Also Seminara et al. [57] have developed a piezoelectric transducer array for flexible applications. The sensors can be implemented on an artificial skin. Refer to Figure 2.30.

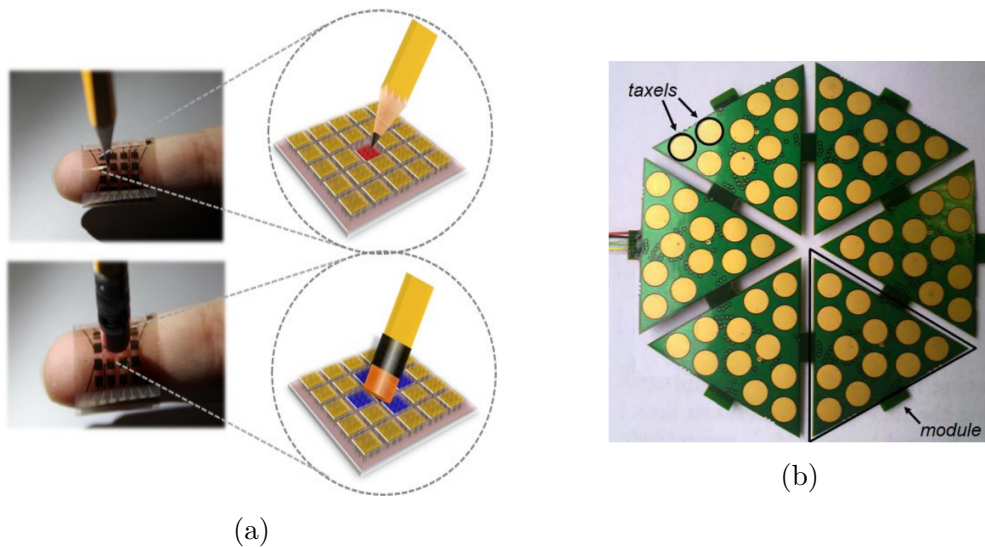


Figure 2.30: (a) Piezoelectric transducer array for sensation categorization [56]
(b) Piezoelectric transducer array for flexible artificial skin [57]

2.5 Piezoresistive Tactile Sensors

Piezoresistive materials have the peculiar property of changing electrical resistivity upon application of mechanical deformation. This property can be utilized in tactile sensing by integrating piezoresistive material into the sensing element of the sensor.

Upon application of tactile forces, this piezoresistive element will deform causing a change in electrical resistivity of the accompanying circuit. This change in resistance can be measured to quantify the tactile forces being applied.

Kumar et al. [58] gives a primary example on development and application of such technology. They have integrated a resistive force sensor onto one claw of a two jaw gripper equipped to a 5 degrees of freedom (DOF) robotic arm. They have used the setup for grasp control.

The first consideration is to select a proper piezoresistive material. Polydimethylsiloxane (PDMS) stands to serve as the material of choice in recent research due to its bio-compatibility, flexibility, chemical inertness and high sensitivity [59]. A NiCr based method has also been proposed for MEMS applications [60].

While designing tactile sensors, it is often necessary to have the capability of sensing 3D forces i.e. shear stress in perpendicular directions and normal loads. Wen et al. [61] have developed a three axis tactile sensor using a polymeric membrane and four sensing cantilevers.

The cantilevers have two piezoresistive elements, one on the top surface and other on the sidewall. Therefore deformation along perpendicular planes can be captured. When the polymeric membrane causes all four cantilevers to deform simultaneously depending on tactile forces applied on the membrane, change in resistance of all elements can be used to quantify the tactile force. Refer to Figures 2.31 & 2.32.

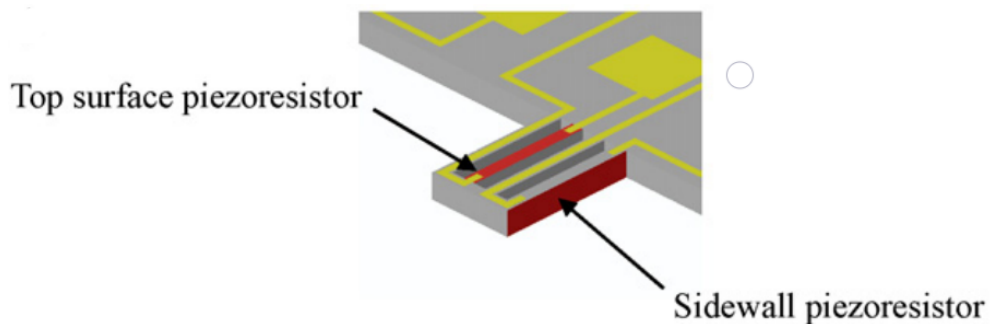


Figure 2.31: Enlarged view of the sensing beam [61]

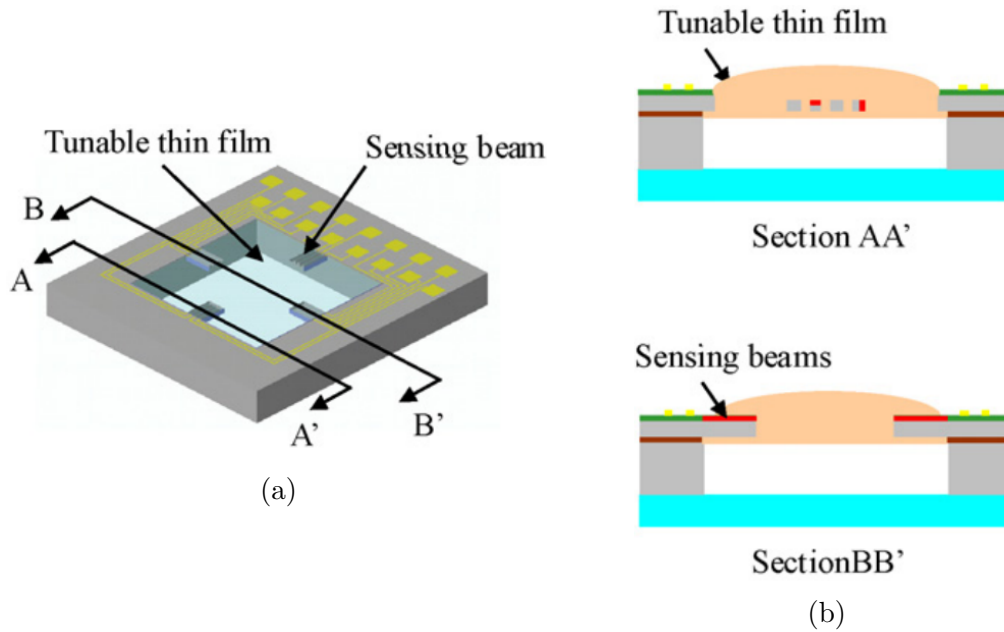


Figure 2.32: (a) Four piezoresistive sensing beams covered with polymer membrane (b) Cross-section views of the sensor [61]

Another sensor operating on a similar concept has been developed for MIS applications by Hu et al. [62]. A different approach for three axial sensing has been taken by Pyo et al. [63] where a piezoresistive substrate is kept above a pair of 2×2 interdigitated electrodes as in Figure 2.33.

The piezoresistive substrate is made by dispersing Carbon Nano Tubes (CNT) inside of a PDMS body. This composition enhances the substrates flexibility and electrical properties.

Tactile forces are transferred through the bump to the substrate. Its deformation will cause the resistance between electrodes to change, which can be captured through an external electrical circuit. Some other interesting approaches for shear force sensing can also be found in research of Hsieh et al. [64] & Noda et al. [65].

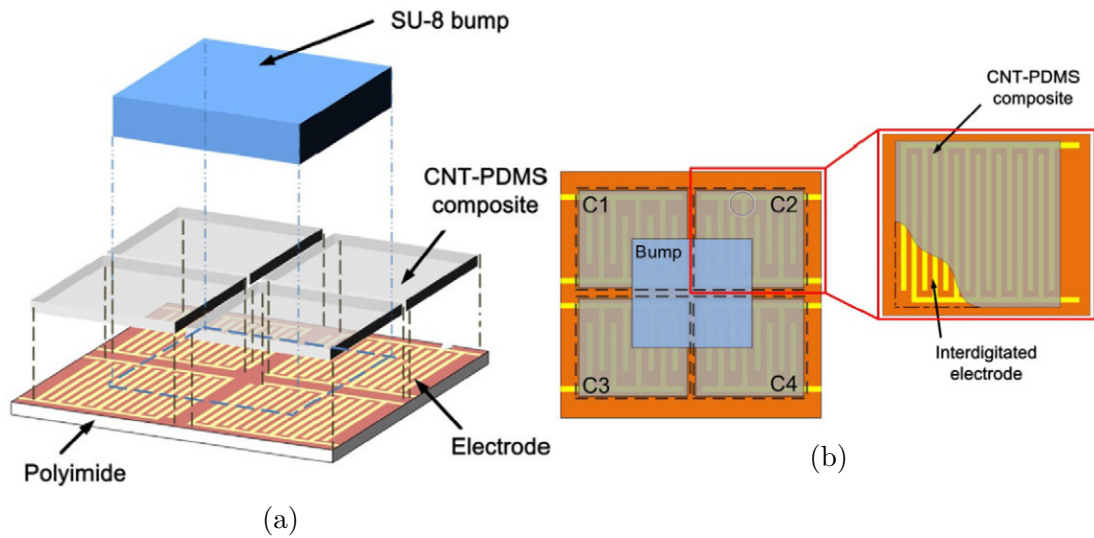


Figure 2.33: (a) CNT–PDMS composite-based tactile sensor (b) Four sensing cells consisting of a CNT– PDMS composite [63]

The technology also has applications in object classification [66], hardness detection [67] and contact localization [68]. Schurmann et al. [69] have proposed a modular tactile sensor which can be assembled according to layout based needs. This methods seems to be feasible when dealing with large sensor arrays instead of building an entire sensor array with complex circuitry from ground up. Refer to Figure 2.34.

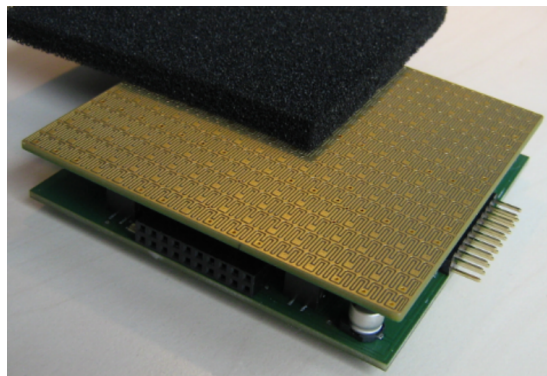


Figure 2.34: Single sensor module [69]

2.6 Tactile Super-resolution

Tactile sensors are often made as a single unit; or if in an array with a limited number of sensing elements. This lack of resolution limits the amount of data gathered from a contact surface.

Increasing the number of tactels to overcome this issue is not always practical due to design constraints, size limitations and cost. Therefore it is necessary to find some other feasible method to address this issue.

Tactile super-resolution is a technique stemming from optical super-resolution microscopy. It involves sub-pixel image localization through centroid calculation over several adjacent pixels [70]. This method can improve the tactile image generated by a tactile array with limited resolution.

Heever et al. [71] have created a force sensing resistor (FSR) array for autonomous neck palpation. The device feeds the tactile data acquired through palpation to a super-resolution algorithm to enhance tactile data and detect tissue anomalies in neck. Refer to Figure 2.35.

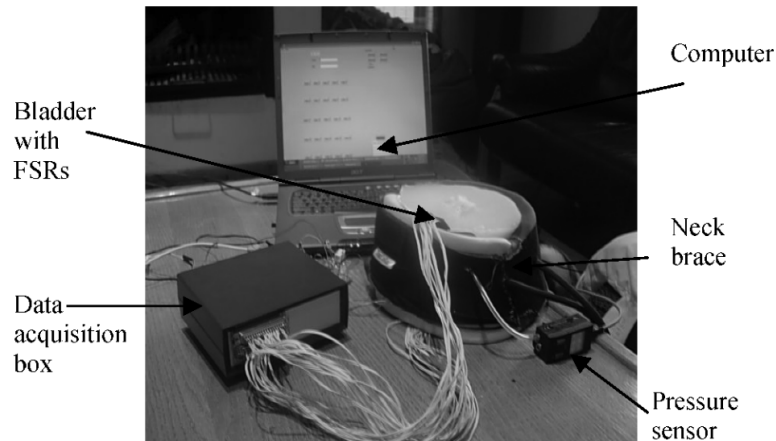


Figure 2.35: Complete device [71]

Lepora et al. [72] have made a more systematic approach into the concept where they have integrated an array of capacitive sensors on a finger tip. The

sensors are distributed over the finger tip and has broad, overlapping and sensitive receptive fields.

The tactile perception method interpolates between the readings of the sensors to attain sub-pixel acuity. The authors claim that they have improved the localization accuracy up to 0.12mm from the actual spacing between sensors which is 4mm. Refer to Figures 2.36 & 2.37.

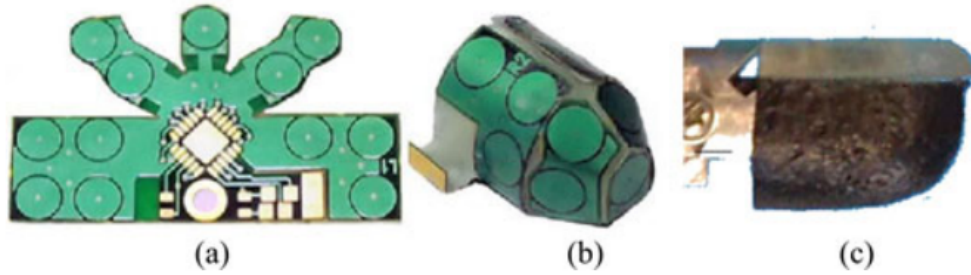


Figure 2.36: Tactile fingertip. (a) Flexible Printed Circuit Board (PCB) (b) Hard core (c) Device covered in a soft silicon foam insulator [72]

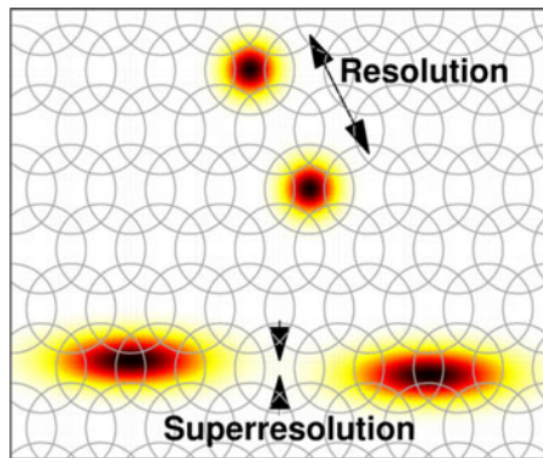


Figure 2.37: Localization super resolution versus sensor resolution [72]

2.7 Grippers

A key aspect to consider while developing tactile sensors is how to implement those sensors on a object manipulation system. In addition to preliminary testing and characterization of a sensor, it is of great importance to evaluate its functionality during real time applications such as object manipulation.

Research has been underway for tactile grippers for a long period of time. They have resulted in grippers being developed in both industrial and research dimensions. Some grippers that are available today can lift weights up to 1000kg [73], have excellent repeatability [74] and fast execution rates [75].

These grippers have found their applications in production industry [76], medical field [77], space exploration [78] and several other fields [79, 80].

2.7.1 Classification of grippers

Grippers in both research and industrial arena can be categorized according to their number of jaws, methods of force/torque generation and methods of force/torque transmission [80].

Number of Jaws

Jaws refer to the contact surfaces of the gripper that interact with the object being grasped. Grippers with two parallel jaws [81] are the most common. They perform simple grasps that often suffice for the task at hand. Where more secure grasps are required three jaw grippers [82] can be used. The enclosed grip performed by three jaw grippers often result in more stable grasps even with arbitrary shaped objects.

Anthropomorphic robotic hands are grippers with four or more fingers that

resemble the construction of human hand. Under actuated mechanisms are also developed. They can be used to solve complex grasping problems including manipulation of irregular shaped objects.



Figure 2.38: (a) 2 jaw Gripper [81] (b) 3 jaw Gripper [82]

Methods of force/torque generation

Grippers can utilize various force/torque sources to operate. Electric motors are the most popular of them. Consisting of servo motors, stepper motors, DC & AC motors, they provide an efficient, clean and easily controllable means of actuation with the ability to handle heavy loads.

Pneumatic actuators are also used in grippers where they utilize pressurized air and/or vacuum suction to operate. Their construction is simple and provide high gripping forces with a relatively lighter system. Hydraulic operated grippers are often found in large settings where high levels of load handling is required. Cost and weight of such systems is high due to its necessary components such as hydraulic oil reservoirs, pumps and circulation channels.

Force/torque transmission mechanism

Several mechanical means of force/torque transmission can be found in grippers. Linkages are most common of them. Gear and rack configuration, cam and follower configuration and screw type actuation are also used. These configurations determine how the movement is transferred to the jaws, force vs actuation speed characteristics and how wide the jaws could open.

2.7.2 Grippers used in known environments

Industrial Grippers

Grippers used in industrial settings usually have information on grasp parameters. These parameters include position & orientation, size & shape, static equilibrium on dynamic movements of the object. They usually use feedback on dynamic change of those parameters using hall sensors, accelerometers, ultrasonic sensors and photoelectric sensors [83].

Vacuum suction based grippers have also been used due to their advantages such as the ability to lift wet, oily or slippery objects. They are also capable of lifting large objects with minimum effect on the structure of objects. They have been widely used in sheet metal fabrication [84], glass pane manufacturing [85] and packing industry [86, 87].

Medical Grippers

In MIS (Minimally Invasive Surgery) grippers are required to handle tissue manipulation [88]. However, a common problem of such devices is the possibility of tissue damage due to lack of fine control. Use of soft grippers have been researched to avoid this problem by utilizing their self limiting features in force application [89, 90].

Also research have been conducted for robot assisted surgery using grippers. Notable research include a star shaped micro-gripper for tissue excision [91], miniature gripper for tissue retraction [92] and 4 DOF (Degrees of Freedom) surgical forceps for tissue manipulation with force feedback [93].

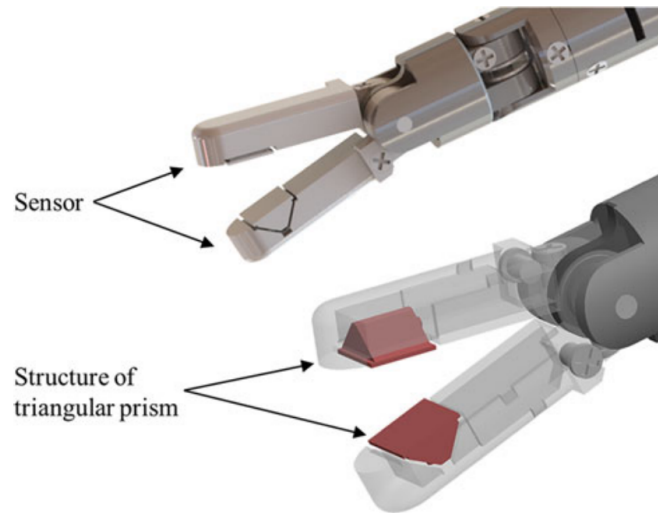


Figure 2.39: 4DOF sensorised surgical forceps for MIS developed by Kim et al. [93]

2.7.3 Grippers used in unknown environments

Grippers used in unknown environments require an extensive amount of information using sensors to evaluate its immediate surroundings. Most often, acquiring these information requires a vision system. A vision system can evaluate the position of the gripper, position of the target object, its orientation and roughly its velocity. Use of vision systems is commonly found in research literature. These research include, picking up randomly oriented object from a bin [94], semiconductor industry [95] and harvesting robots [96,97].

2.8 Research Gap

Though there have been much research conducted on tactile sensors, the inadequate amount of research carried out on tactile sensing systems/arrays limit

their practical applications. These sensing systems and arrays overall have limited robustness with susceptibility to temperature, humidity and unexpected disturbances. Also they lack consistency as their zero load outputs and pressure response curves change over hundreds of cycles. This inconsistency also necessitates individual calibration of each sensing element that is time consuming and error prone.

2.9 Proposed Characteristics of the Tactile Sensor

The tactile sensor developed under this research will address the above issues. It will consist of a robust tactile sensing array based on hall effect. Hall effect based sensors are known to be robust, consistent and easy to fabricate. They are also cost effective. The design of the sensor is compliant to surface irregularities and can perform tasks such as tactile force recognition and contact localization.

DESIGN OF THE PROPOSED TACTILE SENSOR ARRAY

3.1 Application of Transduction Principle

The transduction method used in this sensor is magnetic transduction based on hall effect. The Hall effect is the production of a voltage difference (hall voltage) across an electrical conductor, transverse to an electric current in the conductor and to an applied magnetic field perpendicular to the current [98]. This phenomena and its applications in tactile sensors are described in the literature review.

The above mentioned electrical conductor based hall effect applications are difficult to implement. This is because to generate a considerably high hall voltage, the required current, magnetic field density and size of the conductor can all be somewhat larger than what is acceptable as in scale for the development of a tactile sensor.

Therefore semiconductor based hall effect generation has to be considered for any practical purpose regarding tactile sensors. Though the actual mechanisms of action can be quite complex than that of using an electrical conductor, semiconductor based hall effect sensors are commercially available that are both robust and cheap.

Such hall effect based sensor is kept stationary below a magnet that can move freely inside an elastomeric material. Upon application of force on the elastomer,

it deforms; causing a proportional variation of displacement of the magnet. Refer to figures 3.1a & 3.1b.

Due to the change of magnetic field resulting from displacement of the magnet, the reading from the hall sensor changes. This change can be related to the applied force through deformation of the soft structure as described subsequently in later chapters.

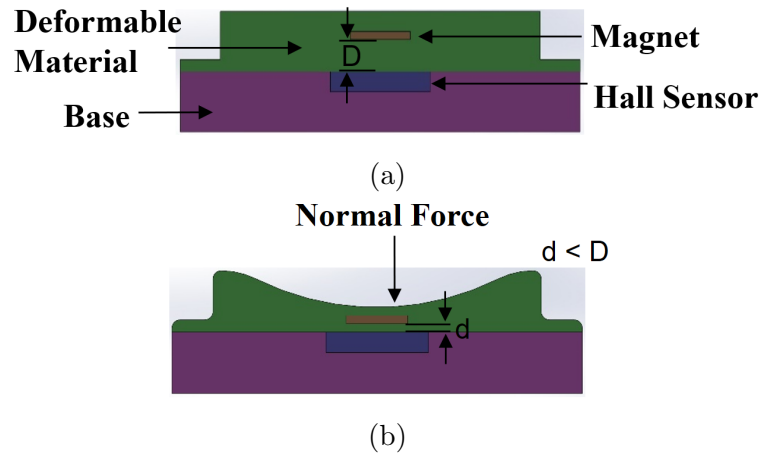


Figure 3.1: (a) Conceptual Design (b) Behavior upon application of force

Then a 4×4 array is constructed with each element being one of these constructions. Consequently, the base of the sensor contains 16 hall sensors in a 4×4 array and the elastomer above it contains 16 magnets in a likewise array aligned one-to-one on top of each other.

Whenever the sensor comes in to contact with an object, forces acting between the object & sensor cause the elastomer to deform. This deformation will change the spatial arrangement of magnetic array residing in the elastomer.

This causes the alignment of flux lines (generated by magnet array) going through the hall sensors to change. The hall sensors can detect this, and upon proper calibration they can be used to characteristically relate the source of disturbance i.e. tactile forces to spatial and temporal variation of hall sensor readings.

3.2 Design Criteria

The sensor is made with a rigid structure built from aluminum. The aluminum container houses all internal parts of the sensor, provides space for external connectivity and means of securing to a gripper. The overall size of the sensor is 64 mm \times 64 mm and sensing area of the sensor is 42 mm \times 42 mm. The size is decided considering the range of objects the sensor is required to interact with and expected strength of the frame.

On the inside, there is a 4 \times 4 array of hall sensors on a Printed Circuit Board (PCB). Next to it, there is a flexible elastomer with a 4 \times 4 array of magnets embedded inside. Hall sensor array directly resides next to magnet array, aligned one-to-one. Refer to Figure 3.2.

Subsequent sections describe the design and construction of following parts of the sensor.

- Elastomer
- Magnet Array
- Hall Sensor Array
- Aluminum Container
- Amplifier
- Signal Analysis and Processing

3.2.1 Elastomer

The elastomer performs one of the most crucial functionalities of the sensor i.e. responding to applied tactile forces via spatial and temporal change of orientation and position of the magnet array inside.

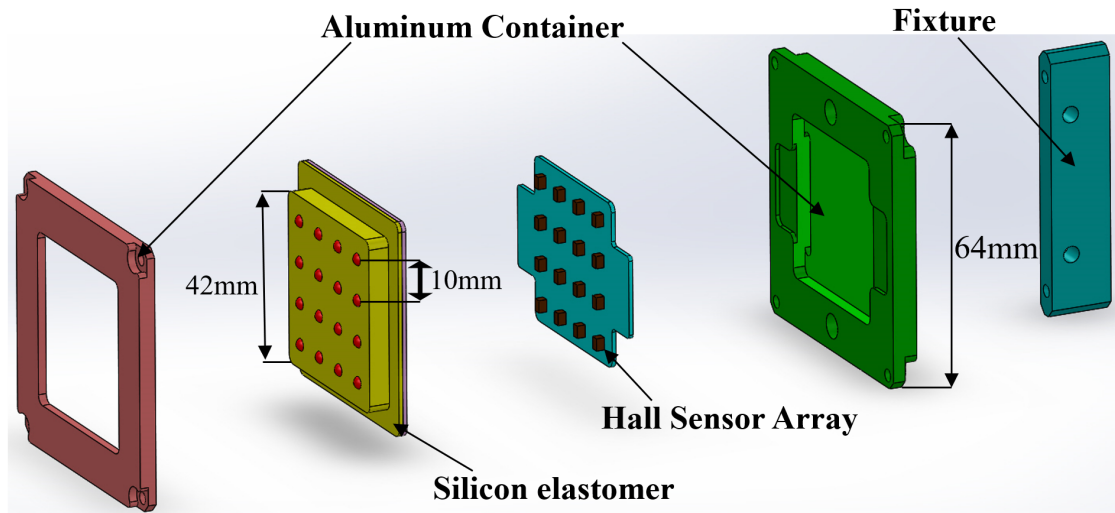


Figure 3.2: Exploded view of the sensor

While developing the elastomer, two design aspects had to be considered. On one side the elastomer should be durable. During continuous use of the sensor, the elastomer gets touched, rubbed against & compressed by various sets of objects with diverse shapes and surface textures. This can happen hundreds if not thousands of times during long term use.

As such the elastomer should considerably withstand wear & tear over a long period of time. Due to this reason, the elastomer has been built with a material that is both strong & durable but still soft & deformable.

By referring to commercially available products, a silicon elastomer marketed as MoldMax 40 [99] has been selected to build the outer layer of the elastomer. This material's hardness added good surface properties for the outer surface of the sensor. Also greenish and opaque nature added decent appearance as well.

However due to the hardness of this substance, it was not feasible to embed the magnet array inside this material. During interaction of the sensor with target object, often than not, it is the minuscule movements of the magnet array that provide a comprehensive description about grasp condition. However the hardness of this material could cause damping of those movements, potentially

causing loss of information.

Therefore it was necessary to select a softer more compliant material than above to embed the magnets, so that they can move more freely. But as per above, we still needed the harder silicon material as well. So the trick is to create a multilayered silicon elastomer with each type of material layered in parallel to provide intended functionality.

Again opting to silicon based materials (due to their low cost, ease of fabrication and durability) Ecoflex DragonSkin [100] has been selected as the ideal candidate for the new purpose. The material had all the required properties and also it allowed propagation of magnetic flux lines through itself reasonably well. This was important for the functionality of hall sensors.

The construction was as follows. The outer later (MoldMax 40) was 1 mm thick and covered the entire sensing area. It also ran inside the aluminum container, securing the elastomer mitigating any relative movement between the elastomer and aluminum construction.

It also had a 4×4 array of hemispherical ridges built on the outside. This was done to enhance the grip between target object and sensor. This became useful in later stages of development since enhanced surface friction between contact surfaces increase the responsiveness of the sensor. It became sensitive to smaller disturbances thus allowing to capture minor changes of tactile forces. Refer to Figure 3.3a.

Then there was another 4×4 array of cylindrical ridges built on the inside of the elastomer that was perfectly aligned one-to-one with the previously mentioned array of hemispherical ridges. This was done to enhance the transmission of tactile forces felt by the outer hemispherical ridges to the magnets embedded in the elastomer by utilizing the same harder material to do so instead of using the softer material. Refer to Figure 3.3b.

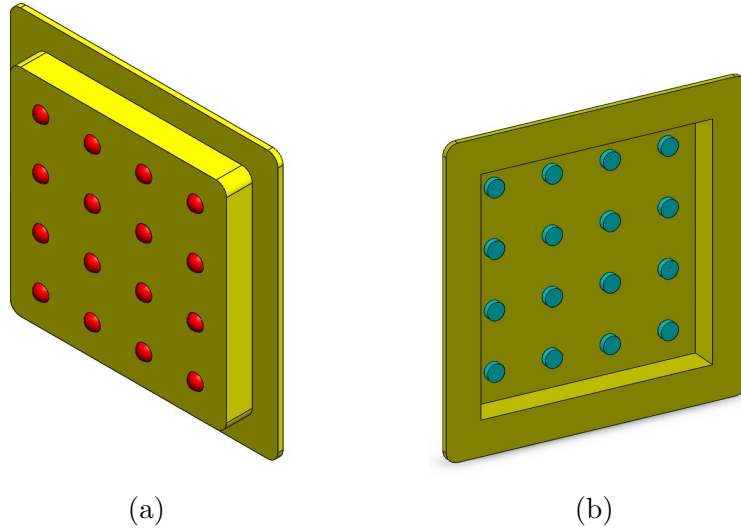


Figure 3.3: 3D Model of Outer Layer – (a) Hemispherical ridges on outside (b) Cylindrical ridges on inside

The magnets (rare earth metal – neodymium circular magnets) used were 3 mm in diameter and 2 mm in thickness. They were placed on top of the cylindrical ridges that possessed the same diameter as magnets.

A problem arise at this stage due to the strength of the magnets. They cannot practically be kept on the elastomer till next stage of molding since they tend to stick to each other at the slightest misalignment. Sticking the magnets to the elastomer using Cyanoacrylate i.e. super glue has been tried, but the alignment was not perfect.

If there was any misalignment between magnets after the elastomer was made, it would act detrimentally for the performance of the sensor since each taxel becomes non-identical to each other w.r.t to response. As random variations of magnetic flux dispersed throughout the elastomer cause hall sensors to output erratic signals. The sensor could become unreliable with regard to maintaining sufficient correlation between input tactile forces and output hall voltages.

The solution was to add an intermediate layer of silicon (EcoFlex DragonSkin), for the sole purpose of aligning and holding the magnets in place for subsequent stages of development of the elastomer. This intermediate layer filled the cavity

inside the outer layer, leaving necessary space for placing the magnets.

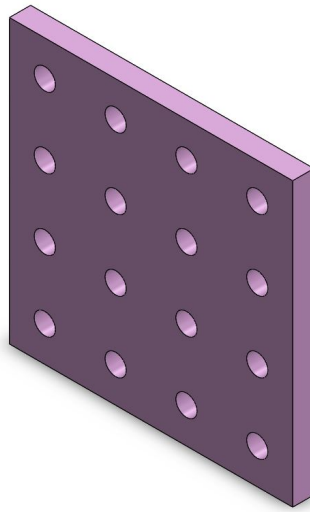


Figure 3.4: 3D model of Intermediate layer

After magnets were placed evenly in the holes, the inner layer of the elastomer was developed. Initially it was planned to develop intermediate layer and inner layer at once. But since it was met with practical difficulties, this method was adopted. However, since both layers are built with the same material, the curing stage fuse the two layers into one eliminating any relative movement between the layers.

Also it should be noted that the intermediate layer sticks to the outer layer extremely well even though they are built of two types of silicon materials. Thus upon finishing the fabrication of elastomer, it behaves as one single unit rather than three layers acting independently (This characteristic is critical to the performance of the sensor).

To finish the fabrication of elastomer, the inner layer was developed on intermediate layer effectively trapping the magnets inside. Refer to Figure 3.5a. Also on the open side of the inner layer, space was reserved to embed the hall sensors since only then there would be no relative movement between the hall sensor array and the elastomer itself. Refer to Figure 3.5b. Emphasis should be made on the fact that the *only* relative movement desired is between the magnets

themselves and hall sensors.

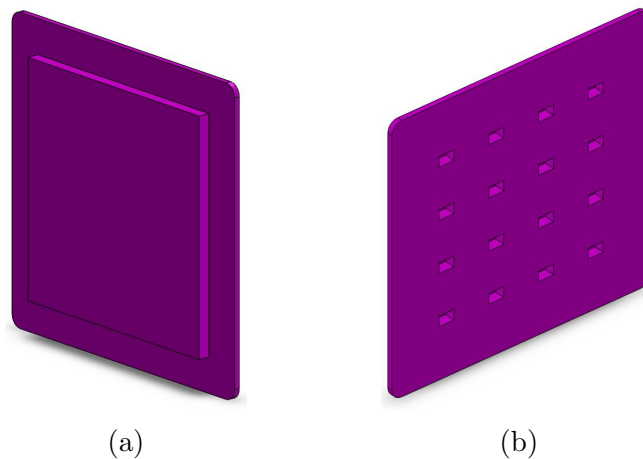


Figure 3.5: 3D Model of Inner Layer – (a) Flat side touching the magnets (b) Rectangular holes to receive SOT-23 package of the hall sensors [101]

After the fabrication was complete, the final elastomer consisted of three layers fused with each other with magnets embedded. It also had space left for insertion of the hall sensors. Refer to Figures 3.6 & 3.7.

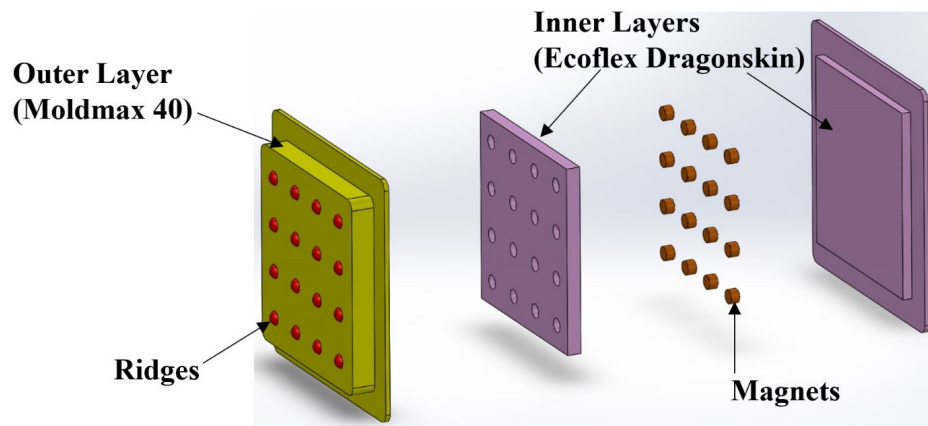


Figure 3.6: Exploded view of the elastomer

The fabrication of the elastomer was done using 3D printed molds. The prepared substance (MoldMax 40 or EcoFlex DragonSkin) was poured into the mold and allowed to cure as per given instructions. After a reasonable period of time, the material was cured and the molds were be separated carefully.

Upon mixing with the curing agent, MoldMax 40 material was poured into the bottom flange (red) of the mold. After allowing for the trapped air to escape, the

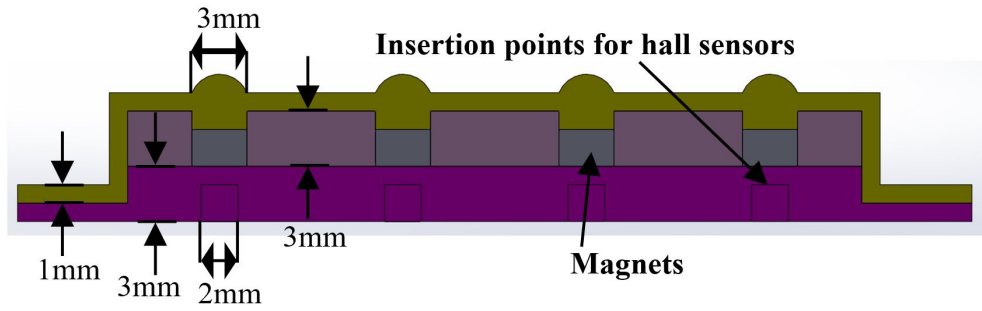


Figure 3.7: Sectional view of the elastomer

outer-layer-flange was placed on top and pressure was applied till the mold was closed. While pressure was being applied the excess material was squeezed out. Refer to Figure 3.8.

This setup is kept to cure for the duration mentioned by the manufacturer. Also small holes (1 mm in diameter) were drilled on the top flange to allow more air to escape, or conversely to allow some air to enter in case of shrinkage.

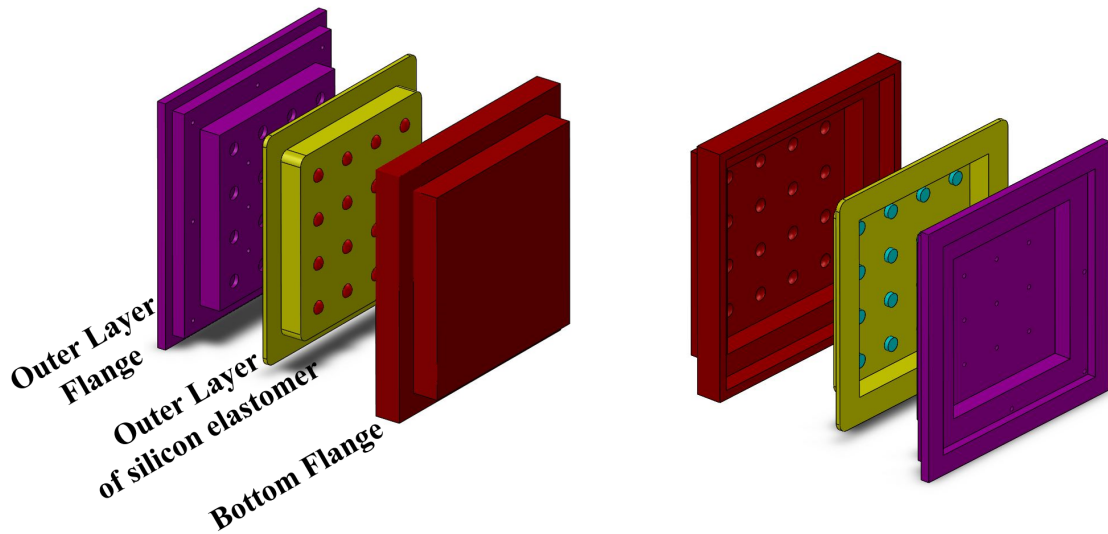


Figure 3.8: 3D Model of the mold (Red & Violet) for outer layer – material is poured into the flange depicted in red

After curing, the top flange was carefully removed. The outer layer was kept without removal in the bottom flange. To create the intermediate layer, prepared EcoFlex DragonSkin solution was poured into the cavity of the outer layer. Now the intermediate-layer-flange was placed on the bottom flange and the subsequent procedure was followed exactly as it has been done before. Refer to Figure 3.9

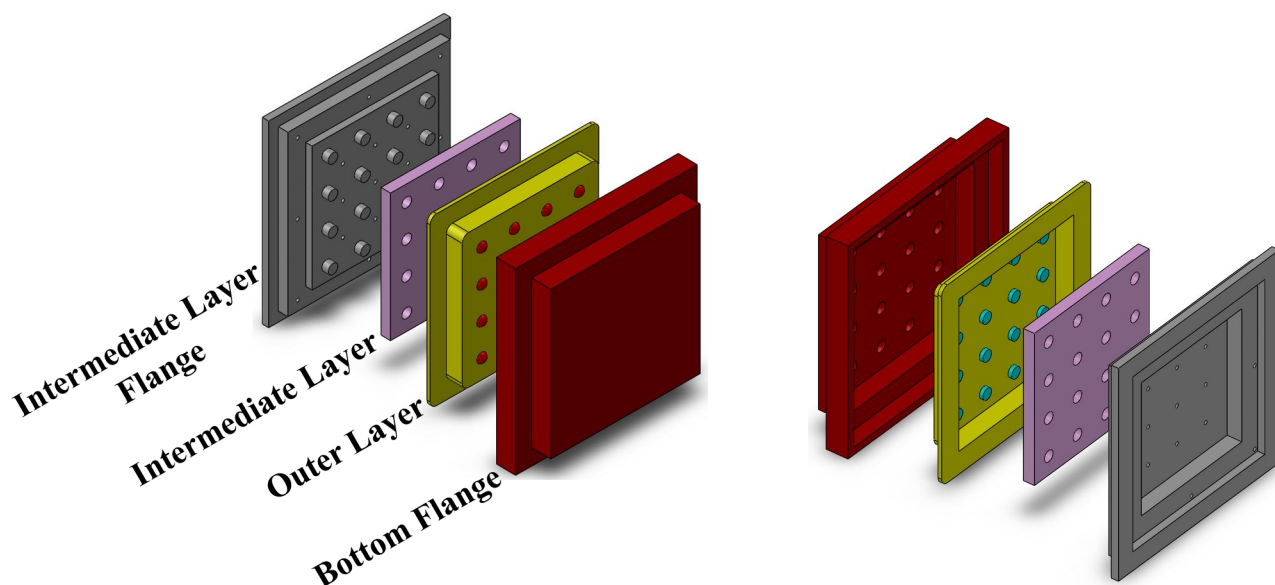


Figure 3.9: 3D Model of the mold for intermediate layer (Pink) – material is poured into the cavity of yellow colored outer layer over the blue colored cylindrical pattern

After curing and removing the top flange, the magnets were placed in the 4×4 array of cavities formed by the mold in the intermediate layer. The magnets were placed with coercivity direction in mind, so that they were all aligned in one direction.

After placing the magnets, the inner layer was formed by pouring the prepared EcoFlex Dragon Skin to the remaining space of the bottom flange. Then the inner-layer-flange was placed on top and the previous procedure was repeated to finish the construction of the elastomer. Refer to Figure 3.10. Figure 3.11 depicts actual construction steps in developing the elastomer.

3.2.2 Magnet Array

The elastomer contained a 4×4 array of magnets embedded inside. They were evenly spaced and placed in a single plane. The selected magnets were cylindrical shaped rare earth metal (Neodymium-N50) magnets with 3 mm in diameter and 2 mm in thickness.

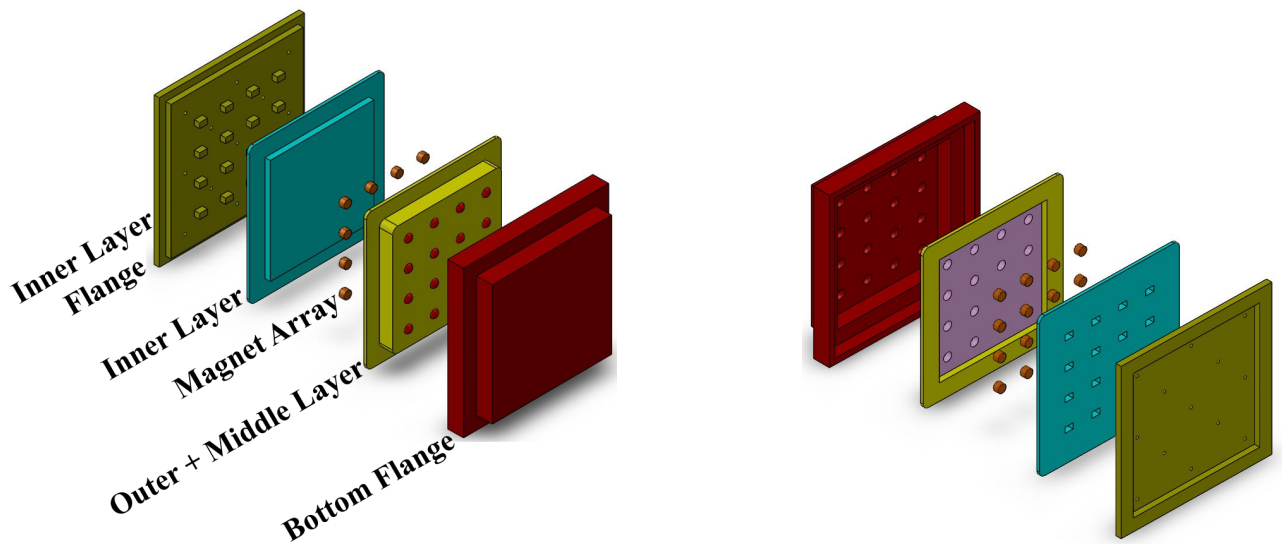


Figure 3.10: 3D Model of the mold for last layer (Blue) – material is poured into the flange depicted in red over the intermediate layer concealing the magnets



Figure 3.11: Steps in developing the elastomer from Left to Right – Outer Layer, Intermediate Layer & Magnets and Inner Layer

The shape of the magnets were selected to ease the fabrication process. Circular & cylindrical shapes are easier to model and also such cavities can easily be molded. They do not accompany complications related to edges or corners and their symmetry greatly simplifies the analysis.

The size of the magnets were selected keeping in mind the size of the array and overall size of the sensor. The strength of the magnets were selected considering the shielding provided by the elastomer material. Higher the strength of the magnet, more responsive the sensor would be. But if the strengths of the magnets

were too high, it would saturate the hall sensor preventing it from operating fully throughout its functional range.

A preliminary study has been done using magnetostatic simulation to probe into the variation of magnetic field distribution. Magnet size (diameter & thickness), Strength (grade-N50 etc.), spacing between elements in the magnet array and perpendicular distance between hall sensor array and magnet array has been varied during this analysis.

As it is difficult to present all simulation results for every variation that has been tried, simulation results for the current variation is presented below. Understanding the distribution pattern of magnetic field for present design parameters was key to designing subsequent circuitry that includes hall sensor selection, amplifier design and firmware development.

The design that was being simulated is as follows. Refer to Figure 3.12.

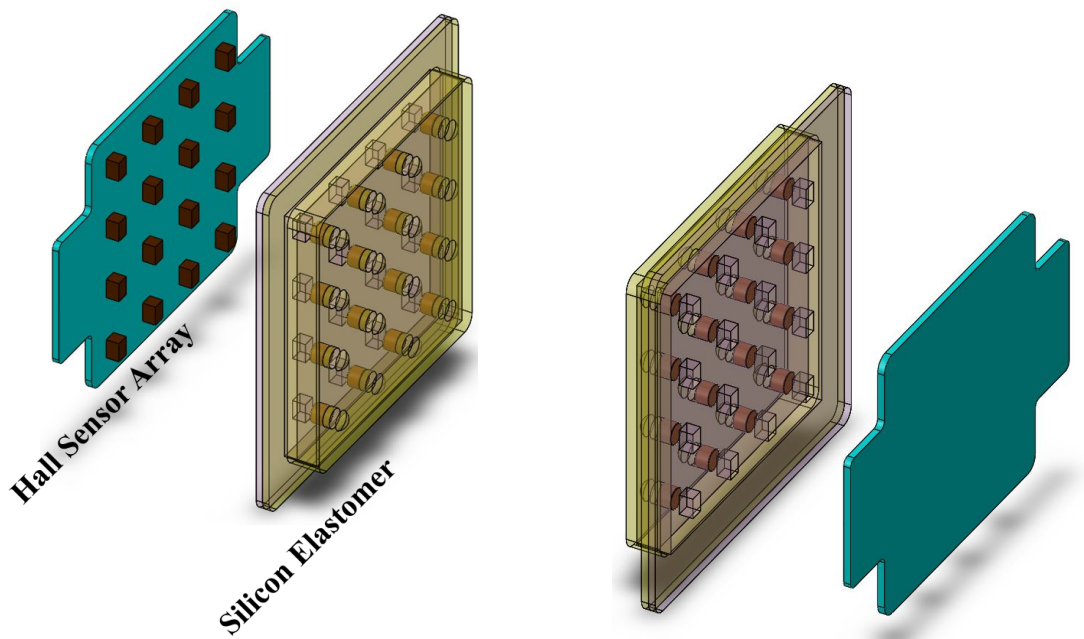


Figure 3.12: 3D Model of the simulated setup – Hall sensor array on the PCB & Transparent view of elastomer

Blue colored panel denotes the PCB and brown colored cuboids on it represent

the hall sensor array. These are 2 mm \times 2 mm \times 3 mm cuboids that are actual dimension-wise representations of the real hall sensor according to manufacturers specifications. The cavities formed in the elastomer are also molded accordingly.

Through the transparent elastomer, the positions of the magnets can be observed. For simulation under no-load condition, the second row of magnets is selected. Only one row consisting of 4 magnets is simulated here due to increase of computational requirements accompanied by increasing complexity of the model. As the structure is symmetrical, uniformity of testing parameters over the entire array guarantees a similar distribution of electromagnetic field over the entire elastomer. Thus simulating only one row suffices for our requirement.

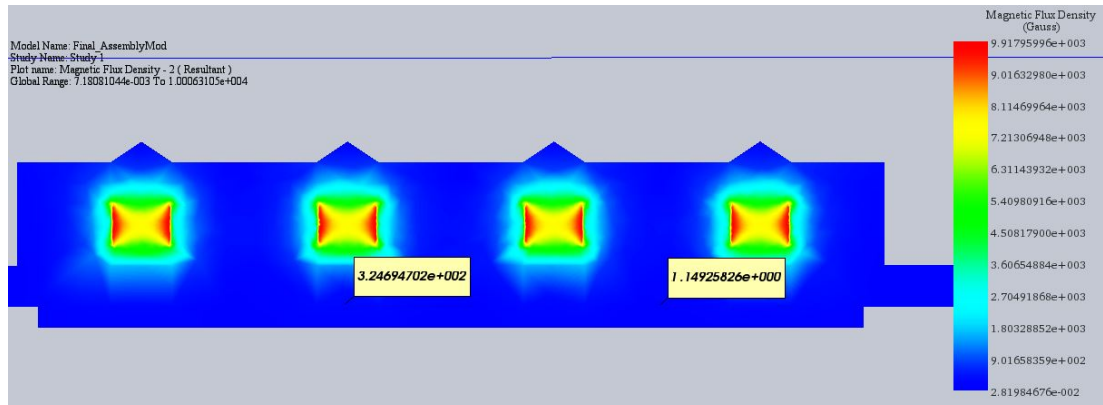


Figure 3.13: Simulation Results—one row under no-load

The responsive range of the ss39et [101] hall sensor is typically between ± 1000 Gauss. According to Figure 3.13 the magnetic flux density near the hall sensor is $\tilde{3}24.69$ Gauss. A field strength of that amount is detectable by the hall sensor yet insufficient to saturate the sensor at the same time.

Moving away from the magnets, the magnetic field diminishes accordingly reporting $\tilde{1}.149$ Gauss in-between hall sensors in the vicinity of PCB. Thus it can be deduced that cross talk between hall sensors due to overlapping magnetic fields is kept at a minimum.

Figure 3.14 captures the magnetic flux distribution under maximum possible compression of the elastomer. It is at this point the hall sensors feel the maximum

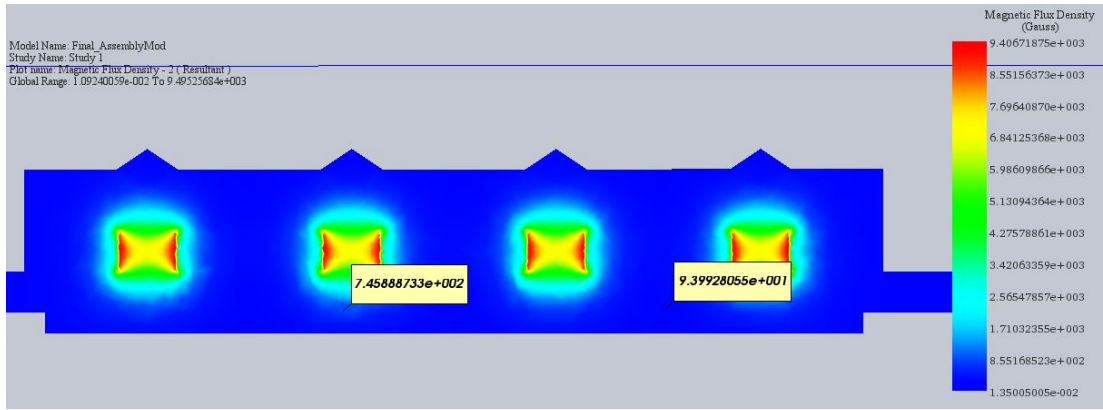


Figure 3.14: Simulation Results—one row under full-load

field strength of the magnets. The hall sensors are exposed to a magnetic flux density of 745.89 Gauss which is a marked increase w.r.t the previous simulation in Figure 3.13.

However this value is still below the saturation field density of the sensor which enables reliable sampling of data throughout the full range from no-compression to maximum compression of the elastomer. It should be noted that the distance magnets have moved towards the hall sensor is only 1 mm between Figures 3.13 & 3.14 to cause this change in field density. Thus the sensor is extremely sensitive to external disturbances such as tactile forces and to a lesser extent, noise.

The simulation was carried out using the Magnetostatic simulation module of EMWorks plugin [102] for Solidworks.

3.2.3 Hall Sensor Array

The hall sensor array is the array of electronic elements that are sensitive to the change of electromagnetic flux density caused by deformations of the elastomer. As depicted in Figure 3.17 the hall sensors were arranged in a 4×4 array on a PCB. The circuit board has an odd shape with extensions on two ends. These extensions allowed for a fixturing mechanism for securing the PCB to the aluminum container so that it would not move relative to other parts during operation.

The hall sensor used here is ss39et [101] Integrated Circuit (IC) developed by Honeywell International Inc. Its low cost, small footprint i.e. Small Outline Transistor Package-23 (SOT-23) and minimal current consumption characteristics make it an ideal candidate for this purpose. Refer to Figure 3.15.

It has an operating voltage range from 2.7 DC Voltage (Vdc) to 5 Vdc of which 5 Vdc is ideal. The response is linear i.e. output voltage (analog) varies linearly with strength of the magnetic field. This behavior makes characterizing the sensor immensely simple. The sensor has an operating temperature range of $-40-100^{\circ}\text{C}$ with null drift of $\pm 0.1\% ^{\circ}\text{C}^{-1}$.



Figure 3.15: ss39et sensor in SOT-23 package – package area is $4.4\text{ mm} \times 2.4\text{ mm}$

The sensor responds to both positive and negative Gauss with a typical range of ± 1000 Gauss. It outputs $\tilde{2.5}$ Vdc at zero field strength and reaches zero volts or Supply Voltage (VCC) depending on field direction. Thus was the necessity to arrange magnets in the elastomer with identical coercivity directions so that all hall sensors will have identical response to the movement of magnets.

As these hall sensors are required to respond to minor movements of magnets, signal to noise ratio is a critical factor. Too much noise will drown out the fine voltage variations generated by small changes in magnetic fields. Therefore it is necessary to use filtering capacitors on VCC for each sensor to filter out high frequency noise. The typical circuit is as follows.

For the complete setup, 16 of such circuits have to be arranged on one PCB with interconnecting power lines and separate output lines. To increase robustness, filter capacitors are added for each hall sensor's power line separately. The additional wiring requires a multi layer PCB, with two layers in total for power

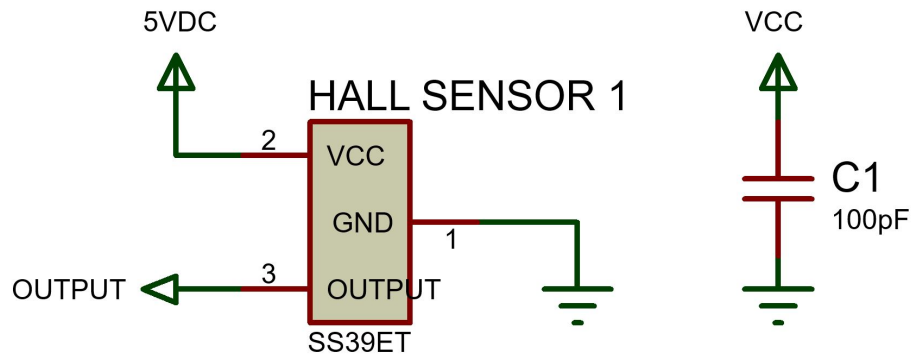


Figure 3.16: Circuit for one hall sensor

plane, ground plane and signal lines.

Power and output connections are made at the back of the PCB using Single in Line (SIL) connectors mounted via Through Hole Technology (THT). All other parts are mounted via Surface Mount Technology (SMT) to save space.

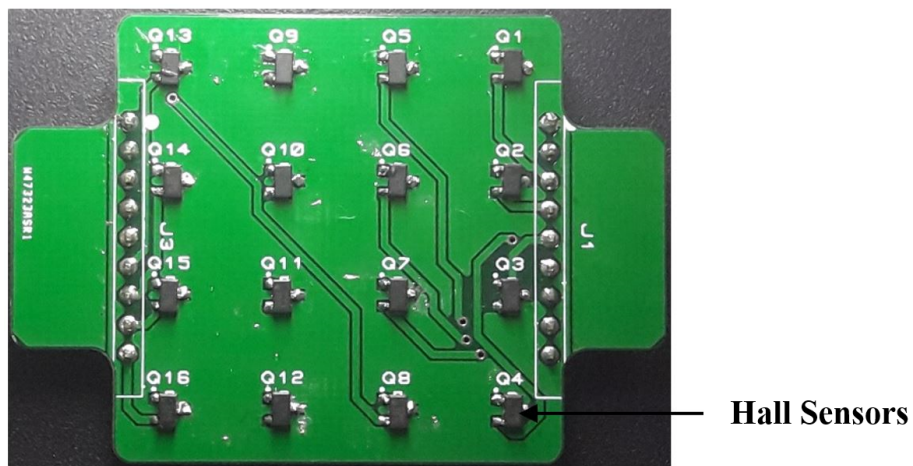


Figure 3.17: Hall sensor array

3.2.4 Aluminum Container

This is the assembly that holds all the internal parts of the sensor. It is a rigid, corrosion resistant construction that is also aesthetically appealing. It protects delicate inner parts against impacts, vibrations and prevents undesired movement of parts by holding them tightly in place. It is made of 6mm thick sheet of aluminum (a light, strong & durable material) and spray painted with a

black protective coating.

Computer Numerical Control (CNC) machining has been used to route and drill on the metal sheet. This allows sub-millimeter accuracy in development and close approximation of multiple curvatures in the design. Though the cost of CNC machining can be quite high, the benefits outweigh the expenses by a large margin.

The construction has three parts namely flange, base and fixture. Initially the fixture is attached to the base using two nut & bolt pairs. It provides means to fix the sensor to an external device such as a gripper. Electronics are placed on the base and space is provided for wiring through back of the base.

The odd extensions of the PCB perfectly aligns with grooves on the base thus allowing proper securing of the hall sensor array. The elastomer is placed on top and flange is secured using four nut & bolt pairs. Refer to Figure 3.18.

3.2.5 Design of the Amplifier

Magnetic flux density values obtained from the magnetostatic simulation depicted in Figures 3.13 & 3.14 are $\tilde{3}24.69$ Gauss and $\tilde{7}45.89$ Gauss for uncompressed and fully compressed states of the elastomer respectively. Though there can be minor variations of these values due to slight changes in material properties of EcoFlex DragonSkin and trapped air bubbles in the elastomer, the overall behavior is the same.

The typical response range of the hall sensor is ± 1000 Gauss and above values from simulation are in positive flux density response range of the sensor i.e. 0–1000 Gauss. As per manufacturer’s specifications analog output of the sensor varies linearly with the strength of the magnetic field between 0–VCC for ± 1000 Gauss. VCC denotes the Direct Current (DC) supply voltage.

This means for positive Gauss values, the output varies between $VCC / 2$

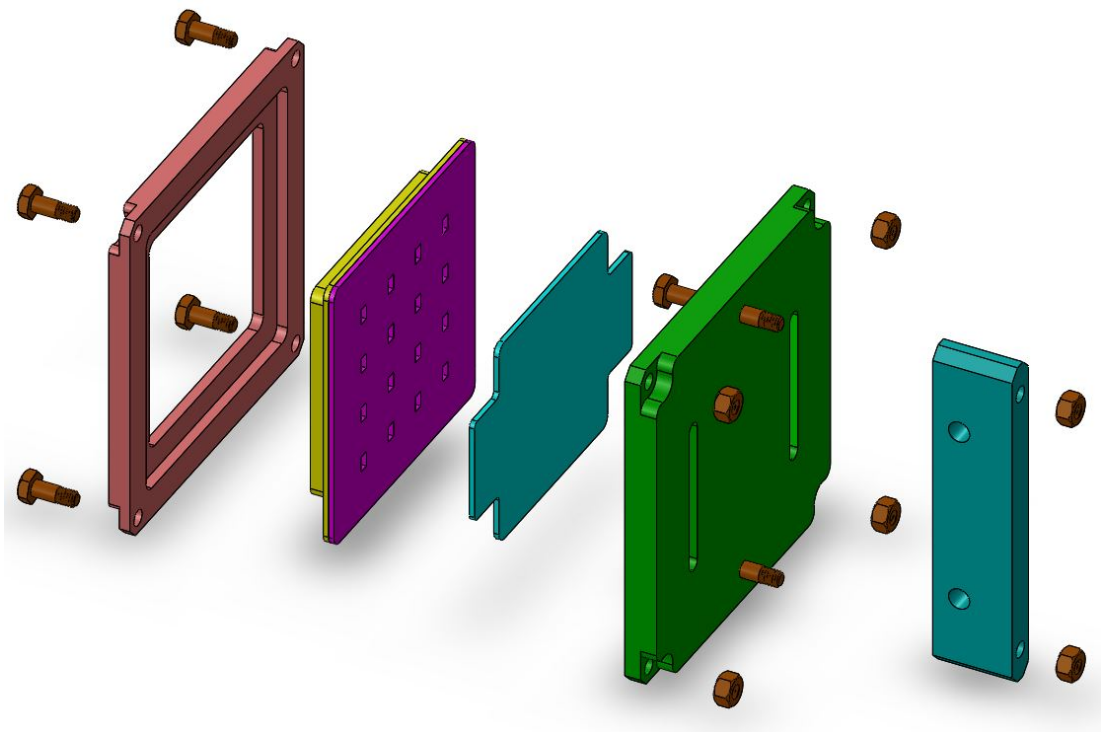
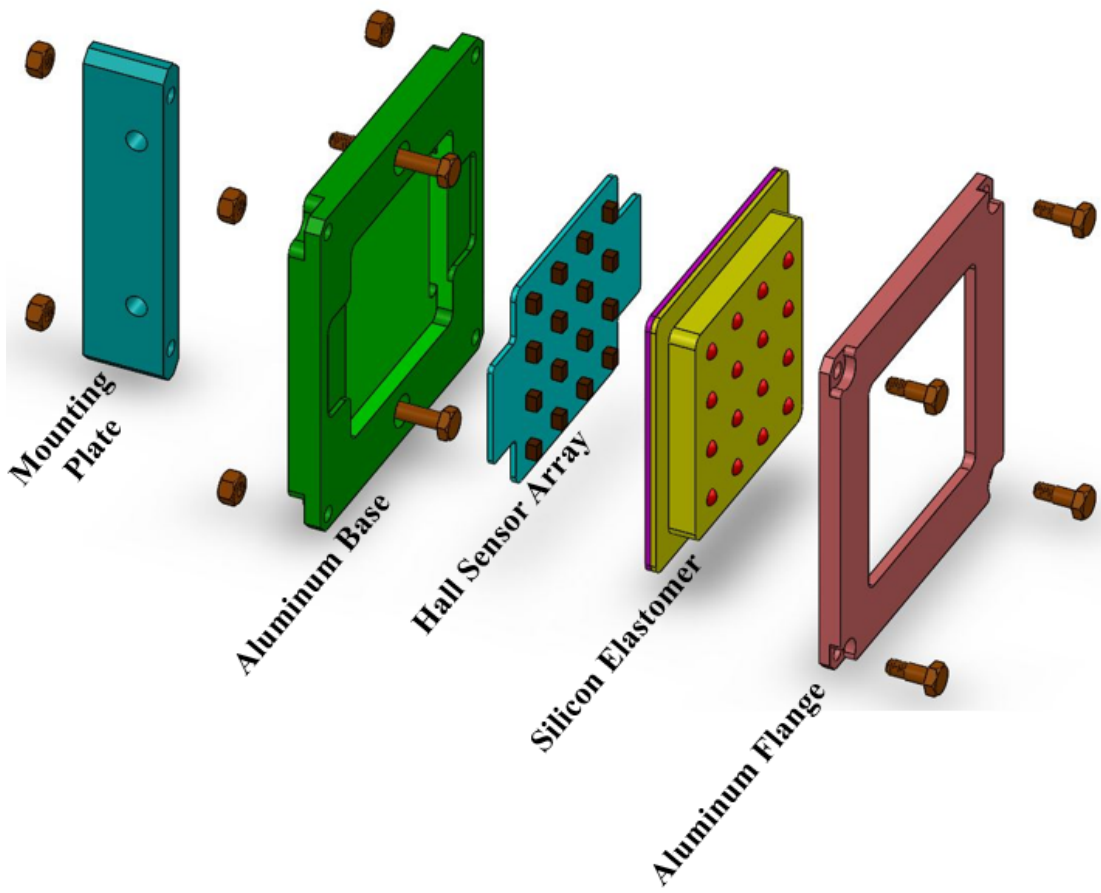


Figure 3.18: Exploded view of the complete construction

and VCC. Accordingly, V_{out} (*Output Voltage*) for minimum and maximum compression states of the elastomer can be calculated as follows. The typical supply voltage i.e. 5 Vdc is considered. B denotes magnetic flux density.

$$V_{out_min} = \frac{VCC}{2} * \left(1 + \frac{B_{min}}{B_{+ve_range}}\right) \quad (3.1)$$

According to Equation 3.1 the minimum voltage output can be calculated.

$$V_{out_min} = \frac{5}{2} * \left(1 + \frac{324.69}{1000}\right) = 3.312V$$

Similarly,

$$V_{out_max} = \frac{VCC}{2} * \left(1 + \frac{B_{max}}{B_{+ve_range}}\right) \quad (3.2)$$

$$V_{out_max} = \frac{5}{2} * \left(1 + \frac{745.89}{1000}\right) = 4.365V$$

It is evident from above that the range of variation in V_{out} is 4.365 - 3.312 = 1.053V. When using an Analog to Digital Converter (ADC) to capture this signal, this range of variation matters. The ADC used for this sensor, that of development board Teensy 3.6 [103] has a resolution of 13 bits. This is a quite high resolution compared to what is offered by other alternatives such as PIC or Arduino and enables in detail analysis of variations in force. However to gain this advantage, it should be implemented properly.

Teensy is a microcontroller that works in 3.3 V logic level, thus its ADC works in the same range as well. Feeding it a voltage ranging from 3.312V to 4.365V may cause it to malfunction or fry the chip as well. Thus circuitry is needed to create an output voltage signal that varies between 0–3.3V from an input voltage

signal varying in the range 3.312–4.365V.

First the null offset (3.312V) should be removed so that a clean signal is obtained that varies between 0–1.053V. As this is only a fraction of ADC's conversion range, performance can be increased by scaling the range 0–1.053V to 0–3.3V.

A differential operational amplifier has been used to accomplish the above task. A differential operational amplifier is the setup of an Operational Amplifier (op-amp) where it amplifies the voltage difference between its inverting and non-inverting inputs. The typical circuit diagram is as follows. Refer to Figure 3.19.

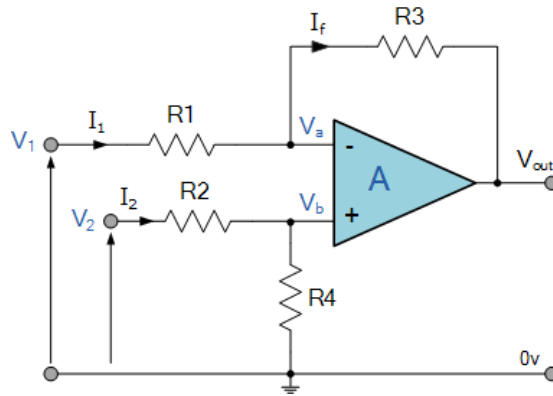


Figure 3.19: Typical arrangement for a Differential Operational Amplifier

The circuit acts as a voltage subtractor/multiplier where the difference of voltage between V_1 & V_2 is amplified by a factor decided by some ratio between the resistors R_1 , R_2 , R_3 & R_4 . For simplicity of design, resistor values can be set such that $R_1 = R_2$ & $R_3 = R_4$. This gives the general equation for differential operational amplifier as in Equation 3.3.

$$V_{out} = \frac{R_3}{R_1} * (V_2 - V_1) \quad (3.3)$$

A reference voltage V_{ref} should be set so that it is always equal to the null offset voltage i.e. 3.312V. A voltage divider can be used to do this. The voltage divider will require 1 fixed resistor and 1 linear potentiometer to fine tune V_{ref}

to the required value since a value like 3.312 with multiple decimal places cannot be reproduced using standard resistor values. By setting $V_1 = V_{ref}$ this amount will always be subtracted from the input signal thus getting rid of the null offset.

Then the resistor values for R1 & R3 should be chosen to do the scaling between 0–1.053V to 0–3.3V. Following calculation can be done.

From Equation 3.3:

$$\frac{R_3}{R_1} = \frac{V_{out}}{(V_2 - V_1)}$$

Setting $V_{out} = 3.3V$, $V_1 = 3.312V$ & $V_2 = 4.365V$:

$$\frac{R_3}{R_1} = \frac{3.3}{4.365 - 3.312} = 3.134$$

Thus $R_1 = 10\text{ k}\Omega$ & $R_3 = 33\text{ k}\Omega$ or any other combination that keeps the amplification factor between 3–4 can be used. Resistors in kilo ohms range are preferred as they reduce current consumption. For the sample circuit refer to Figure 3.20.

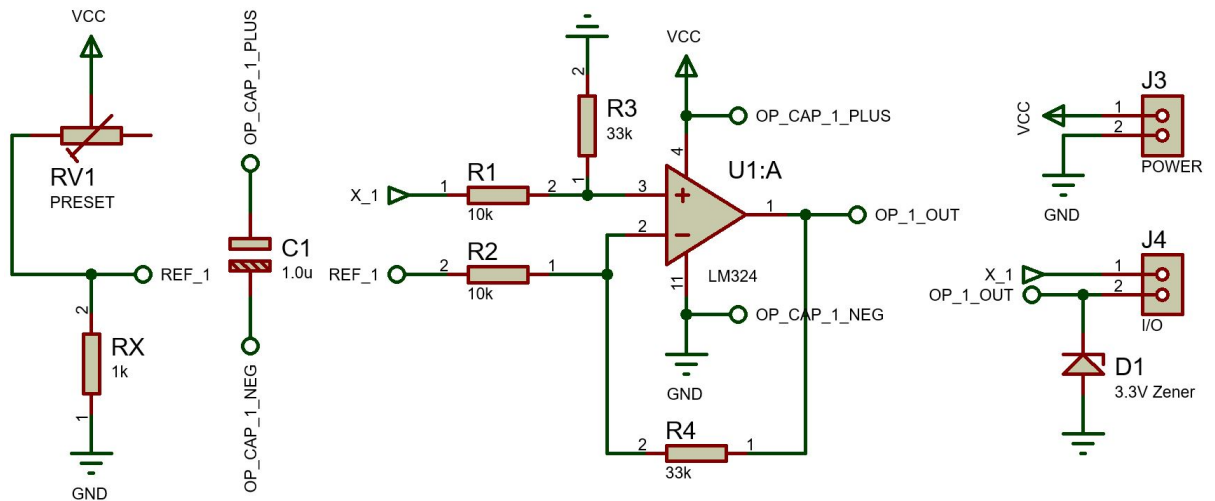


Figure 3.20: Op-Amp circuit for one hall sensor

Reference voltage is obtained using the voltage division done by RV1 Preset and RX (1 k Ω) resistor in series. U1 is the Op-Amp arrangement. SIL Connector

3.2.6 Signal Analysis and Processing

The amplifier outputs an analog voltage in the range 0–3.3V for compression of the elastomer between its idle and maximum compression states. These voltages are fed to the development board [103] and captured through the onboard 13bit ADC. The data can be visualized in real time using the serial output module of the board and also data can be saved using the onboard SD card read/write module.

Writing data to SD card carries convenience in data acquisition and gets rid of systematic errors attached to serial port data transfer such as packet loss. Raw data (no filtering) is captured, saved and subsequently transferred to the computer for analysis.

Data is obtained for the idle state i.e. nothing is pressing against the elastomer and for excited state i.e. a random deformation is made on the elastomer. Data is captured for 5 seconds with a sampling rate of 1 kHz. Sampling rate is decided through previous experience on the same development board considering ADC conversion delay, SD Card read/write delay and clock cycle. Refer to Algorithm 1.

Algorithm 1: Run ADC to get Hall Sensor Data

Data: Hall Voltage: V

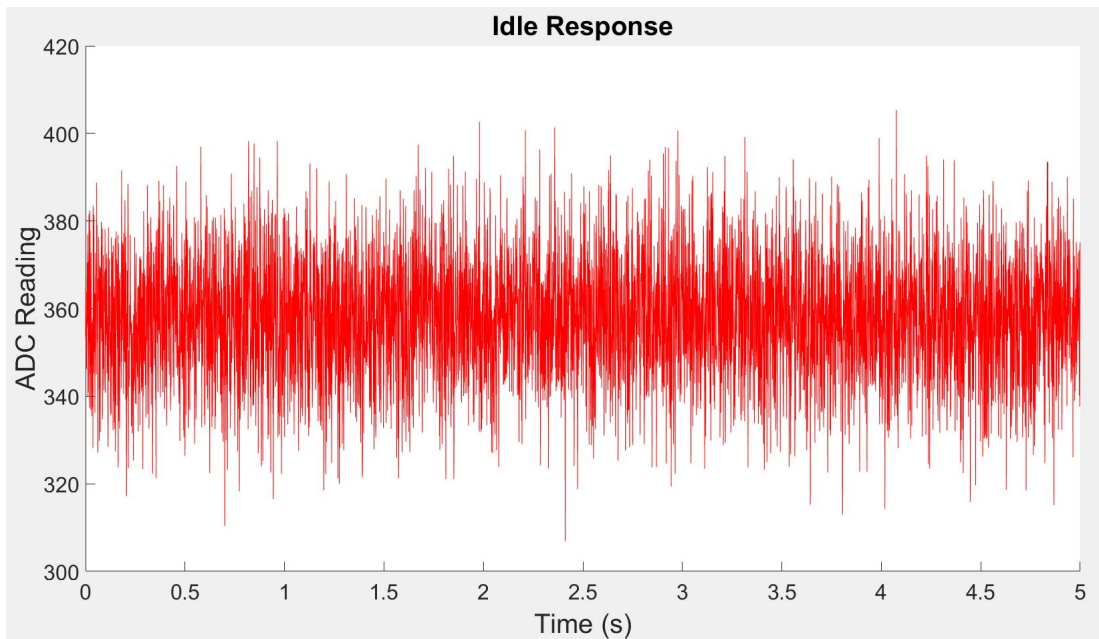
Result: 13bit Value: X

```
1 begin
2   /* Timer interrupt frequency is 1 kHz */
3   while True do
4     /* Loop runs indefinitely */
5     /* INT is set to 1 when timer interrupts */
6     if INT = 1 then
7        $X \leftarrow \nabla(V)$  //  $\nabla$  is the conversion function of ADC
8       INT  $\leftarrow$  0
9       SDCard  $\leftarrow$  append( $X$ )
```

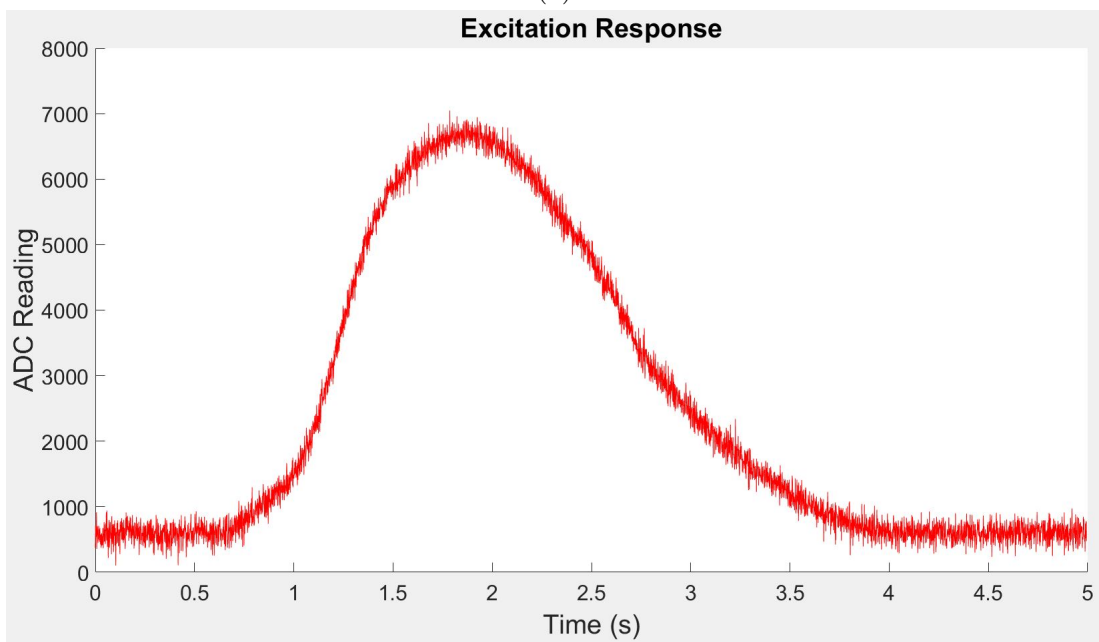
The typical waveforms obtained during the experiment are as follows. Refer to Figure 3.22.

It is evident from Figures 3.22a & 3.22b that a high amount of noise is present in the output. This noise should be filtered out before further processing. To implement a signal filter, the nature of noise should be identified.

By analyzing the frequency components of a signal, specific noise frequencies can be identified. Since it is possible to filter out these specific noise frequencies using low-pass, high-pass or band-pass filters, the signal can be filtered without significant attenuation of useful information. Therefore a Fast Fourier Transform (FFT), a computationally less expensive & efficient version of Fourier Transform is applied to above depicted signals. The results are as follows. Refer to Figure 3.23.



(a)



(b)

Figure 3.22: Signal Waveforms – (a) Idle state (b) Random excitation

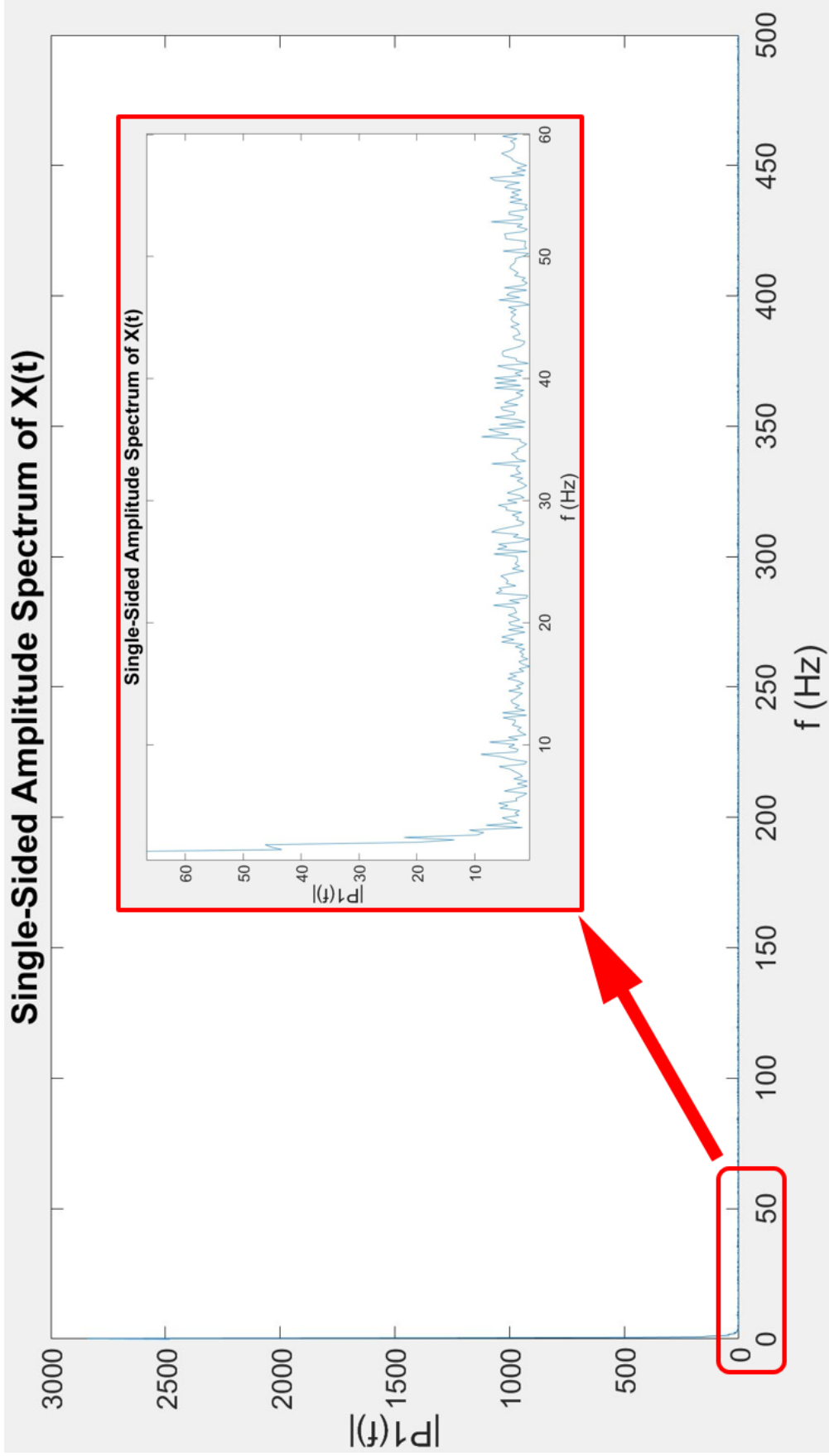


Figure 3.23: FFT for hall sensor output: 0–60Hz range is shown enlarged

FFT plot shows similar information for both scenarios i.e. idle state and random excitation. Thus FFT only for random excitation is given in Figure 3.23. As it can be seen there are no dominant frequencies of noise. The impulse at 0 Hz is due to the DC signal of excitation and rest of the signal power is distributed over a continuous spectrum with random distribution. This is a key characteristic of random noise and this uncertainty of measurement is quite common in electronics.

A moving average filter can be used to filter out this noise. An exponential moving average filter is an ideal solution in this scenario due to its less processing power and memory requirements considering that it has to run inside a microcontroller. It also has minimum lag and its behavior can be reasonably controlled according to our requirements.

The characteristic equation of an exponential moving average filter is given in Equation 3.4.

$$y[n] = (1 - \alpha)y[n - 1] + \alpha x[n] \quad (3.4)$$

$y[n]$	Current estimate of output (at n^{th} instance)
$y[n - 1]$	Previous estimate of output at $(n - 1)^{th}$ instance
$x[n]$	Current noisy measurement
α	A value between 0–1

The behavior of the filter is different for each value of α . For higher values of α , priority is given to current measurement, thus less filtering is done. For lower values of α , the impact of new measurements are attenuated thus more filtering is done. However this reduces responsiveness of the filter for quick changes of input i.e. lagging.

Therefore the selection of α is a tradeoff between sensor's responsiveness versus precision. Thus some definite criteria is needed to decide this tradeoff. For

measuring tactile forces, the sensor should be accurate and precise. If we assume that the tactile forces are not changing quickly i.e. reasonably static forces are being applied, we can neglect all the frequency components above 1 Hz.

This way, stability of the sensor can be improved with a reasonable tradeoff between lag while still maintaining adequate functionality. It will be assumed that the sensor is only required to measure the magnitude of forces that are reasonably static i.e. signal frequency is close to zero Hz.

Thus the Exponential Moving Average (EMA) filter should be applied here as a low pass filter, where its cutoff frequency is decided using the value of α . By taking the Z Transform of Equation 3.4 and solving for the -3 dB corner of the filter one can obtain,

$$\alpha = \cos(\Omega_{3dB}) - 1 \pm \sqrt{\cos^2(\Omega_{3dB}) - 4 \cos(\Omega_{3dB}) + 3} \quad (3.5)$$

Ω_{3dB} is the half power (3dB) normalized frequency in radians. α cannot be negative thus only the +ve answer from above is valid. Since,

$$\Omega_{3dB} = \frac{2\pi}{F_s} f_{3dB} \quad (3.6)$$

where F_s is the sampling frequency and f_{3dB} is the cutoff frequency expressed in Hz, α can be calculated as follows.

Setting $F_s = 1000\text{Hz}$ and $f_{3dB} = 1\text{Hz}$,

$$\Omega_{3dB} = \frac{2\pi}{1000} * 1 = 6.2832 \times 10^{-3} \text{ radians/sample}$$

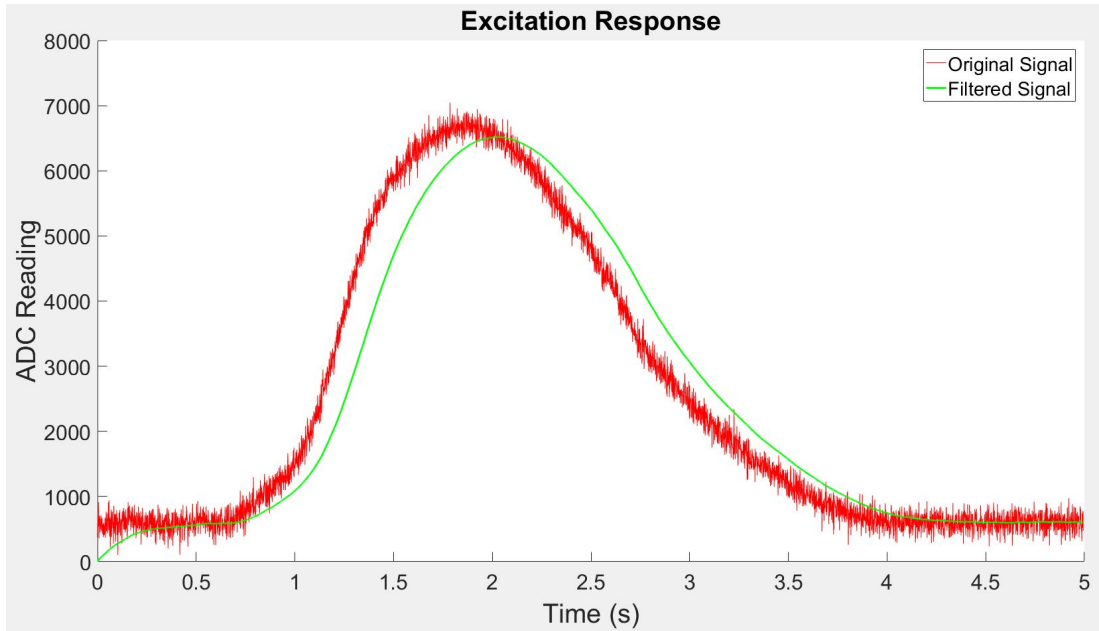


Figure 3.24: Filtered Signal

Assigning to Equation 3.5,

$$\begin{aligned}
 \alpha &= \cos(6.2832 \times 10^{-3}) - 1 \\
 &+ \sqrt{\cos^2(6.2832 \times 10^{-3}) - 4 \cos(6.2832 \times 10^{-3}) + 3} \\
 &= 6.2635 \times 10^{-3}
 \end{aligned}$$

Refer to Algorithm 2 for implementation.

Algorithm 2: Run EMA Filter

Data: 13bit Value: X_N

Filter Ratio: α

Result: 13bit Value: Y_N

- 1 *Apply EMA Filter to smooth out data*
 - 2 **begin**
 - 3 $Y_{N-1} \leftarrow$ Previous EMA output
 - 4 $Y_N \leftarrow (1 - \alpha) * Y_{N-1} + \alpha * X_N$
-

Figure 3.24 shows a plot between signal amplitude vs. time after signal filtering is done using EMA filter with the above mentioned value for α . Original signal is also depicted in the background.

According to this figure, it is apparent that the output signal lags behind the input signal. However this effect is minimal and the signal noise is satisfactorily eliminated. Therefore this output can be used for sensor characterization after following.

According to Figure 3.22a, it can be seen that a null offset is present. Behavior of this null offset is such that upon starting or restarting of the system, it begins with a non-zero value, keeps fluctuating & its value at any particular point of time is uncertain.

For example, consider a time duration of 10 seconds since start of operation. No compression is applied on the elastomer thus the system is in its idle state. The output from the EMA filter indicates a non zero value that has minor variations. These variations as well as the offset value itself is not predictable. It is systemic thus cannot be eliminated and can only be compensated.

Therefore for 10 seconds since startup, the signal will be studied to decide the best counter-offset value. The duration is arbitrary, but through several test runs it was observed that after such duration the result is satisfactory. If the counter-offset is too low, the sensor will not indicate a zero output at idle state and if the counter-offset is too high, the sensor will indicate negative values at idle state. Averaging the output along the entire duration is also not sensible since an EMA filter is already applied.

Therefore a calibration stage is carried out for 10 seconds. 3 seconds are reserved for the EMA filter to converge. During the next 7 seconds, the maximum value of filtered output X_{max} & minimum value of filtered output X_{min} is searched for and memorized. Then the offset is calculated according to Equation 3.7.

$$\text{Offset} = X_{min} + \frac{X_{max} - X_{min}}{2} \quad (3.7)$$

Hence, the output value of the filtered and offset corrected signal will be,

$$\text{Signal Output} = \begin{cases} \text{Signal Input} - \text{Offset}, & \text{if Signal Input} > \text{Offset} \\ 0, & \text{otherwise} \end{cases}$$

Here *Signal Output* denotes offset corrected signal. *Signal Input* denotes signal to be corrected. Algorithm 3 depicts pseudo code for offset estimation.

Algorithm 3: Offset Correction

Data: EMA Filter Output: Y_N
Result: Offset Corrected Output: \bar{Y}_N

```

1 begin
2   T ← Time // Current time in milli seconds
3   t ← 0 // Time stamp of previous iteration
4   Xmax ← 0 // Maximum offset value
5   Xmin ← 10000 // Minimum offset value; Initial value should
   be > MAX(YN), is arbitrary and required for convergence
6   X ← 0 // Estimate for offset value
7   while T - t ≤ 10000 do
   /* Executes for 10 seconds */
   /* Allow 3 seconds for EMA Convergence */
8    $\bar{Y}_N \leftarrow Y_N - X$ 
9   if T - t ≤ 7000 then
   /* Run below code for remaining 7 seconds */
10  |   if YN > Xmax → Xmax = YN
11  |   if YN < Xmin → Xmin = YN
12  |    $X \leftarrow X_{min} + \frac{X_{max} - X_{min}}{2}$ 
13  |   if YN - X > 0 then
14  |   |    $\bar{Y}_N \leftarrow Y_N - X$ 
15  |   else
16  |   |    $\bar{Y}_N \leftarrow 0$ 

```

For complete code for the tactile sensor refer to Appendix A.1.

3.3 Design of the Parallel Jaw Gripper

The gripper is made by CNC machining a 6mm thick aluminum sheet. Aluminum provides necessary strength and light weight. The parallel jaw mechanism operates through a gear system driven by a Servo Motor. The servo motor is controlled using a micro maestro servo controller.

Servo motor is attached to the driving wheel using a D-Shaft and a coupling. The links move relative to each other on bearings attached to each element and center shafts. Refer to Figure 3.25 & 3.26.

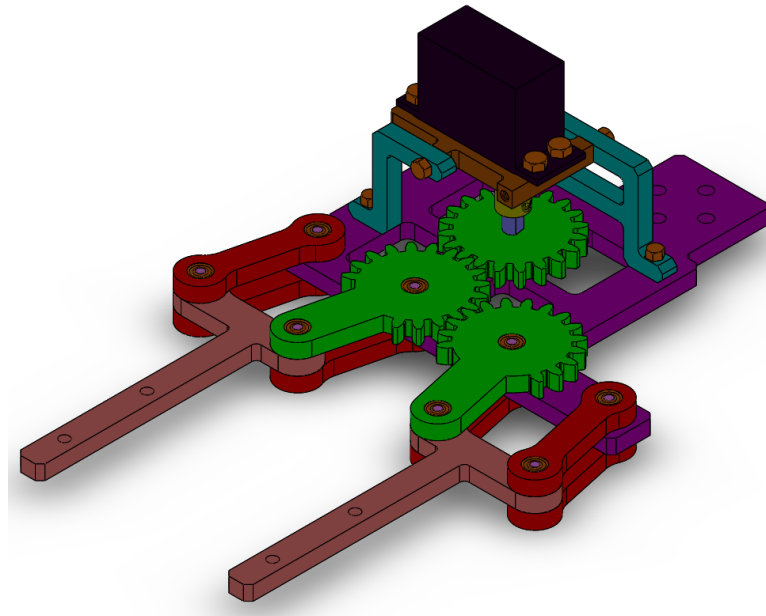


Figure 3.25: Parallel Jaw Gripper - Assembled View

3.4 Hardware Setup

Two identical tactile sensors are fixed on each jaw of the gripper. Refer to Figure 3.27. Servo controller connects to the computer through USB. Thus the gripper can be controlled through code and Maestro Control Center (a useful software bundled with the servo controller) as well. This allows rapid demonstra-

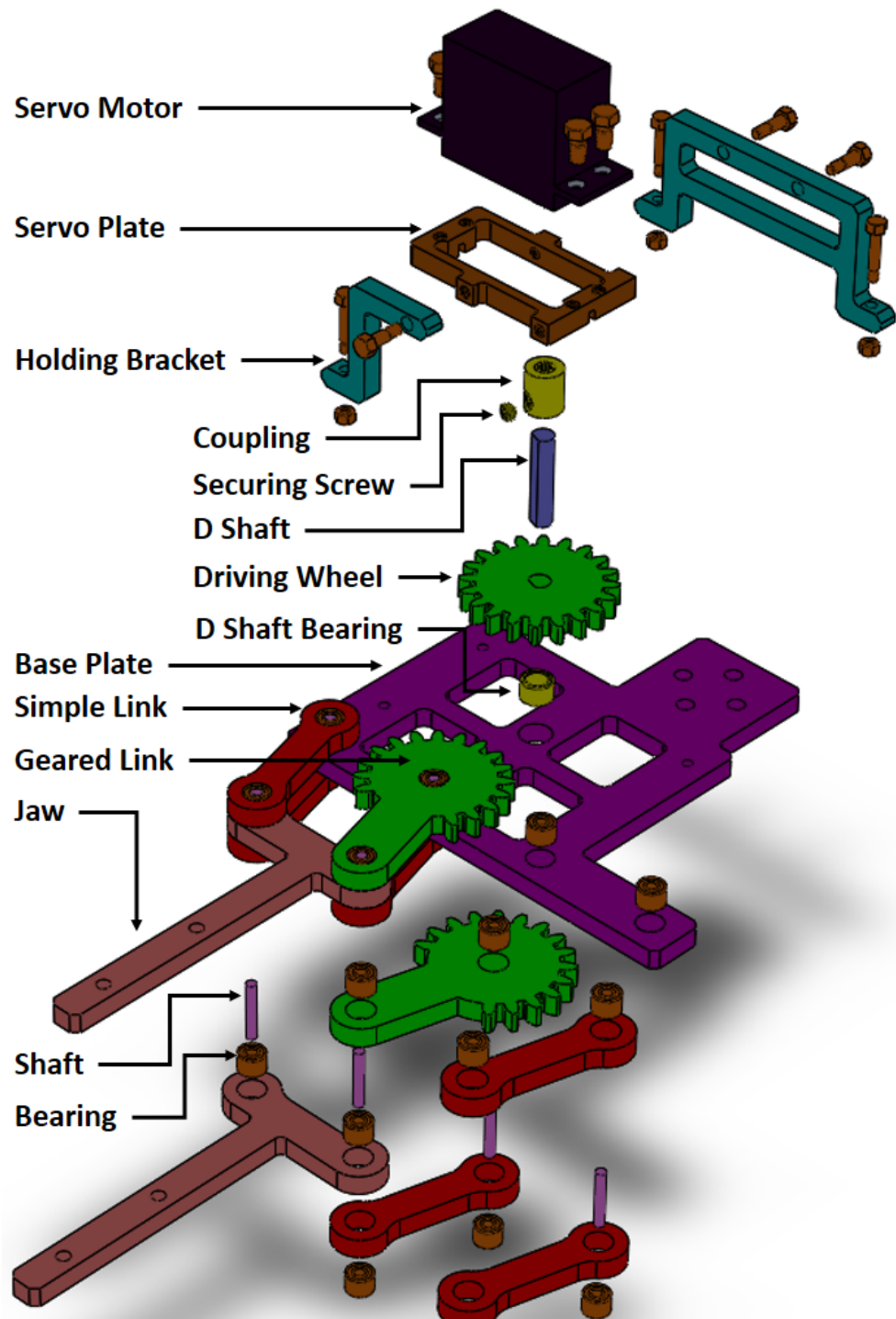


Figure 3.26: Parallel Jaw Gripper - Exploded View

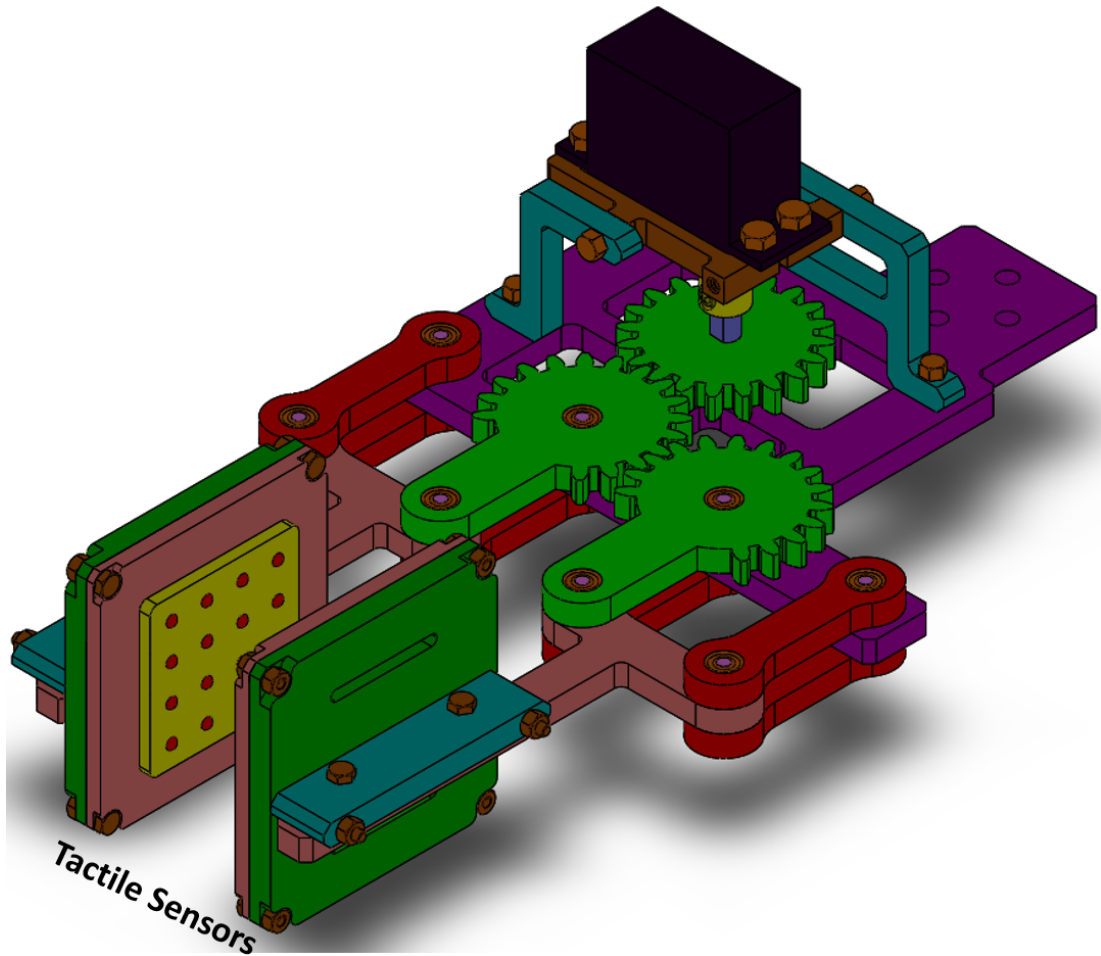


Figure 3.27: Parallel Jaw Gripper with Tactile Sensors attached

tion and programming. The servo motor used here is a Hitec HS-5585MH Servo with enough torque to entirely compress the silicon elastomer on each side of any object.

It requires a 7.4V external power supply that is provided through an adjustable DC bench power supply. By adjusting the maximum allowable current through the motor, the stall torque can be controlled thus preventing any damage to the sensors or motor itself.

For an actual photo, refer to Figure 3.28.

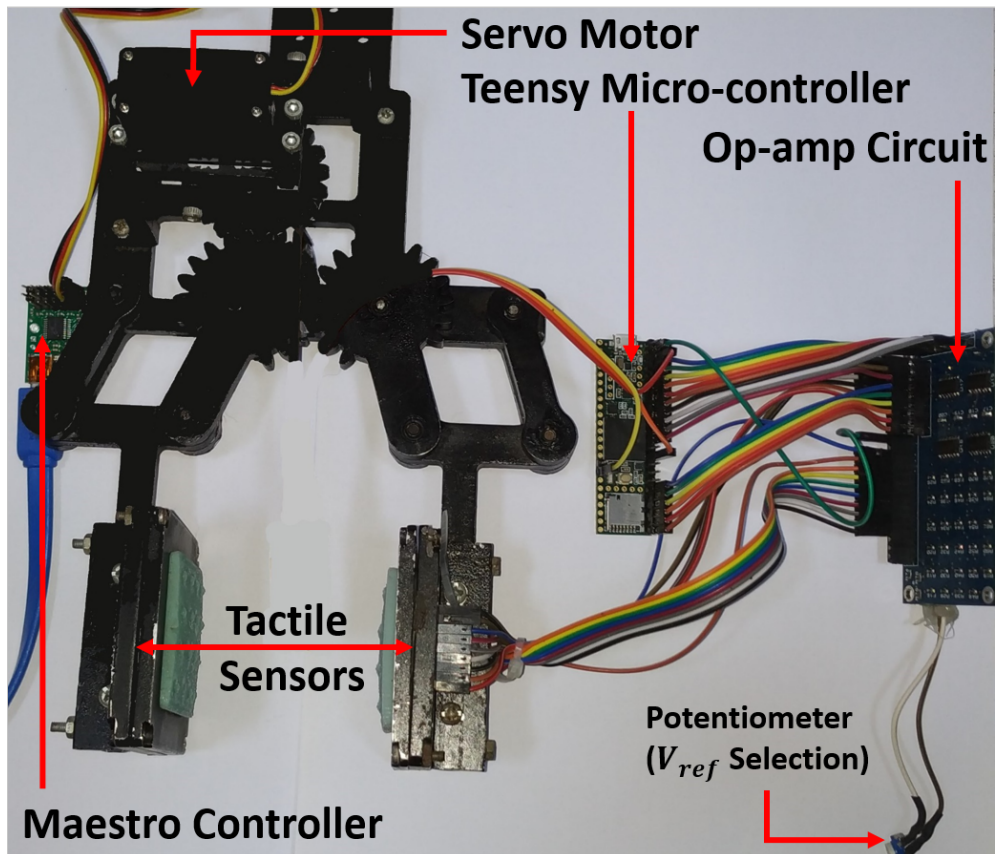


Figure 3.28: The complete experimental setup

CHARACTERIZATION OF THE SENSOR ARRAY

Throughout the previous chapter, an extensive description of the design of the sensor was presented. But to realize its purpose i.e. measure tactile forces, a quantitative relation between its signal output and mechanical forces imposed on it must be derived. To do so, a sensor characterization process must be carried out using a calibration setup, an experimentation procedure and results analysis.

4.1 Calibration Setup

During the design stage of the sensor, it was fabricated so that the sensor has 16 individual channels of response. These 16 separate outputs give rich information about the deformation of the silicon elastomer due to application of tactile forces.

As they were designed keeping in mind their response to normal forces applied on them, a quantitative relation must be established between taxel's output signal vs. actual normal force applied on it. Here taxel means one of the 16 individual elements in the 4×4 array of the sensor. Refer to Figure 4.1.

As such a mechanism is needed to be devised so that a normal force can be applied on each taxel and be measured at the same time. This required a calibration device with sufficient accuracy, precision and capability for such purpose.

For this purpose, the Universal Testing Machine (Testometric - 10KN M350-

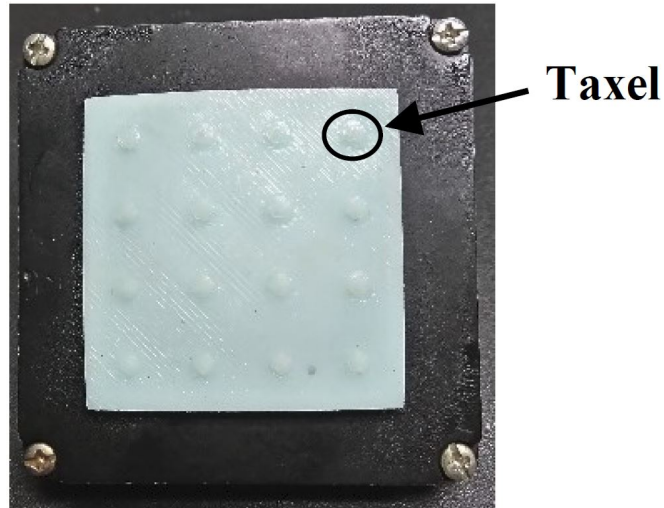


Figure 4.1: A taxel is the combination of elements that provide a separate voltage output for compression of elastomer

10 AT) was used [105]. The load cell of this machine can measure forces up to 10kN. It can measure both tensile and compression forces, where in this case compression forces were measured. Refer to figures 4.2a & 4.2b.

The sensor was fixed to the bottom cylindrical pin using a custom made fixture. Another fixture was fixed to the load cell on the top with 16 pin heads on a 4x4 array. These pin heads were aligned with the same array of taxels in the sensor. Refer to figures 4.3 & 4.4a.

By bringing down the load cell, these pin heads can be imposed on the tactile sensor thereby deforming the elastomer. At the same time the total force acting on the tactile sensor can also be measured using the load cell reading. Therefore the force acting on each taxel is $\frac{1}{16}$ times the load cell reading. The load cell reading was logged against time by the testing machine.

Parallel to the above operation, the sensor sent data to the computer at a sampling rate of 1kHz. This data was recorded by a data logging software custom built for this purpose using C#.



Figure 4.2: (a) Universal Testing Machine (b) WinTest Software Interface

4.2 Experimentation Procedure

The experimentation procedure was as follows.

The procedure was performed using two methods namely Displacement step method and Force step method. Each method was sub divided into a loading phase and unloading phase. The process was repeated for each orientation of the sensor, rotating clockwise against identical initial position. This was done to reduce errors introduced by asymmetries of the silicon elastomer or minor misalignment of the setup.

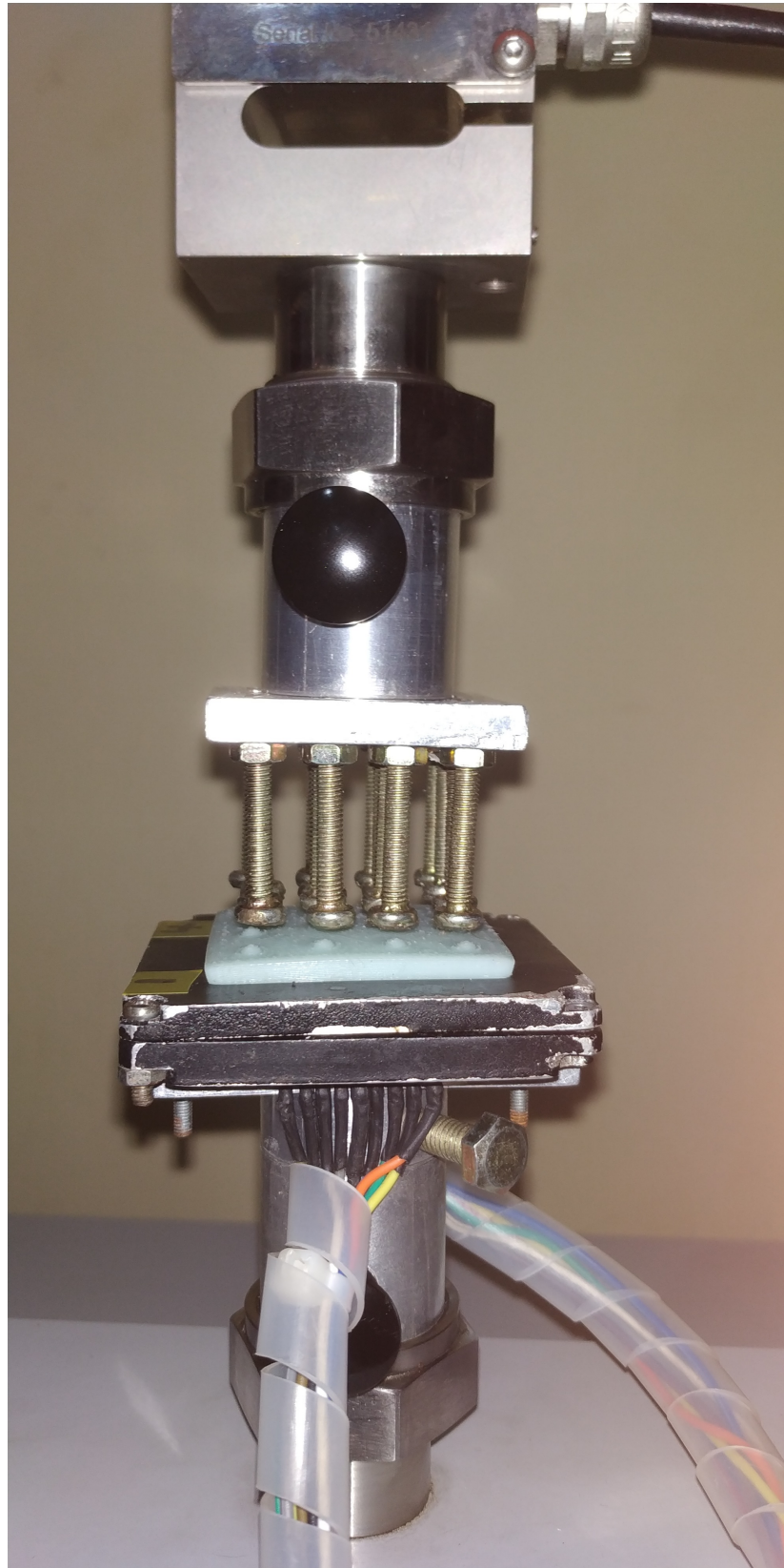


Figure 4.3: Tactile Sensor fixed to the Universal Testing Machine

4.2.1 Displacement Step Method

Under this method, the load cell was brought down in 0.25mm increments. At each increment the load cell was kept still for 30 seconds. A total of 14 steps were done. Total number of steps were selected w.r.t the maximum allowable displacement of the silicon elastomer (3.5mm).

The same procedure was repeated but this time the load cell was moving along the reverse direction i.e. away from the elastomer. The full procedure was repeated for the remaining three orientations of the tactile sensor.

4.2.2 Force Step Method

Under this method, the load cell was brought down in 2N increments up to the maximum allowable displacement of 3.5mm. The same procedure was performed for the unloading phase as well. This was repeated for the remaining three orientations of the sensor.

During experimentation the WinTest UI and Data Logger App presented current state of the experiment. The data was saved for subsequent analysis as well.



(a) Final Setup



(b) Running the experiment

Figure 4.4: Using the Universal Testing Machine to Characterize the Tactile Sensor

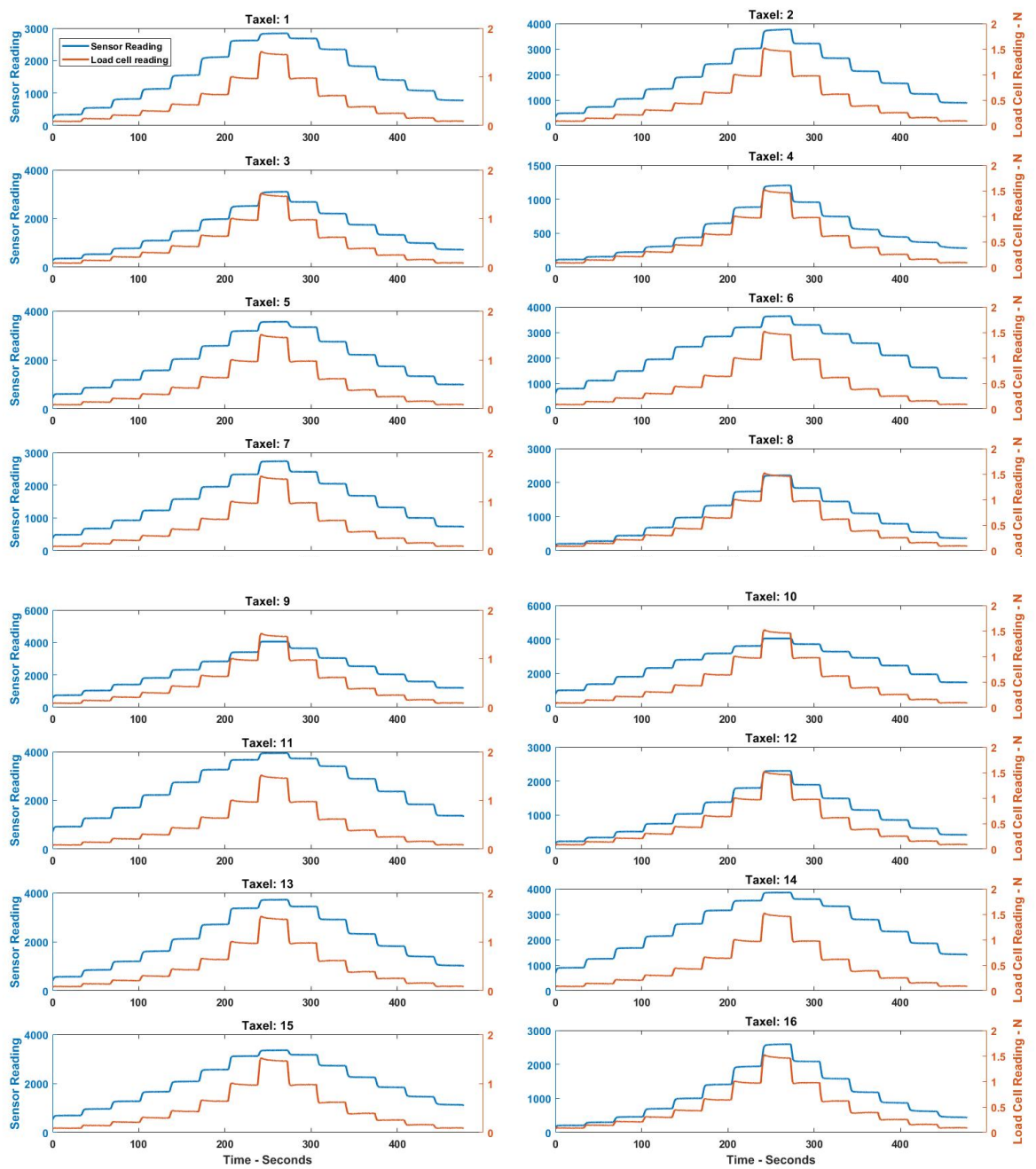


Figure 4.5: Sensor Reading, Load Cell Reading vs. Time: Displacement Step Method

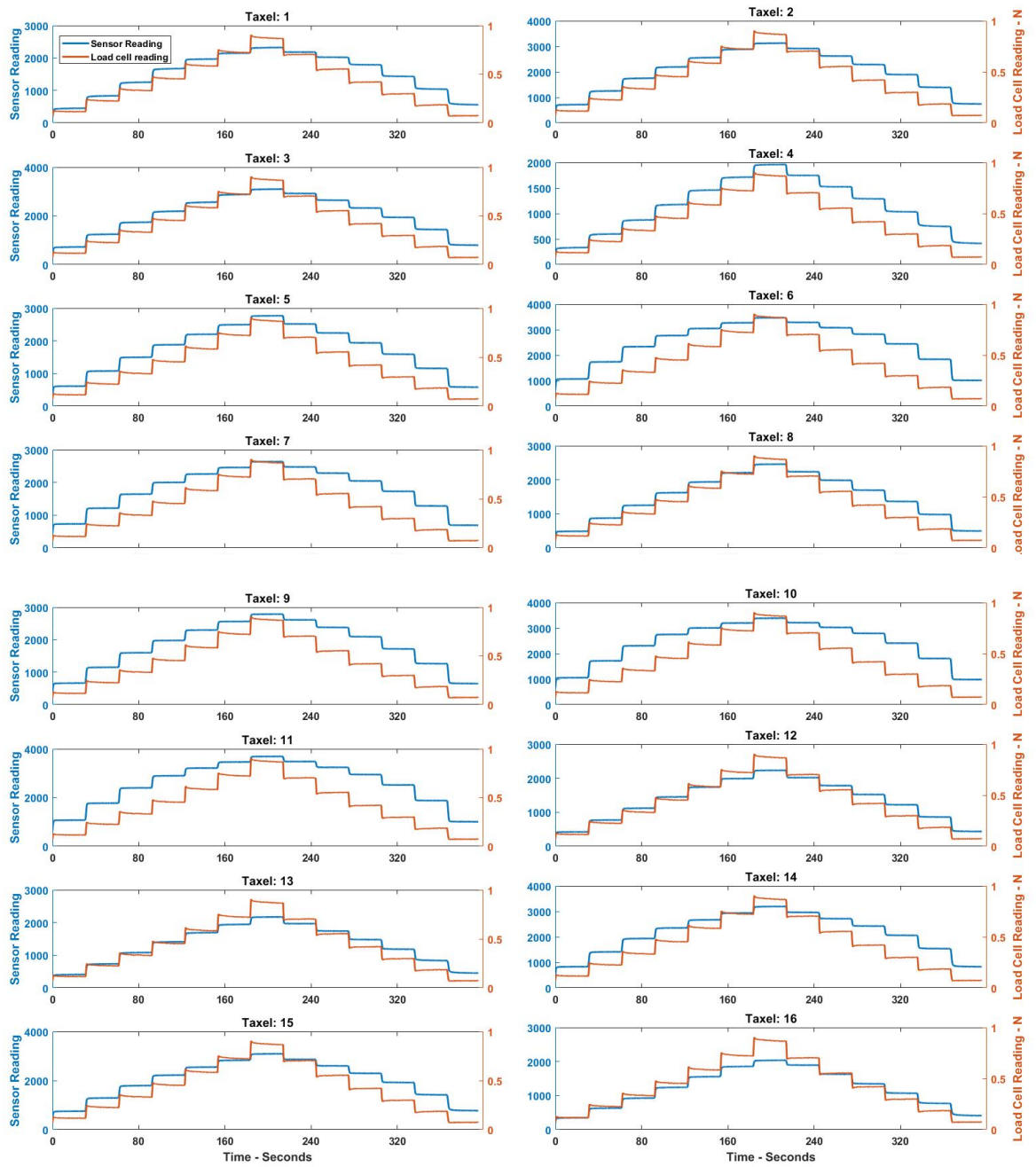


Figure 4.6: Sensor Reading, Load Cell Reading vs. Time: Force Step Method

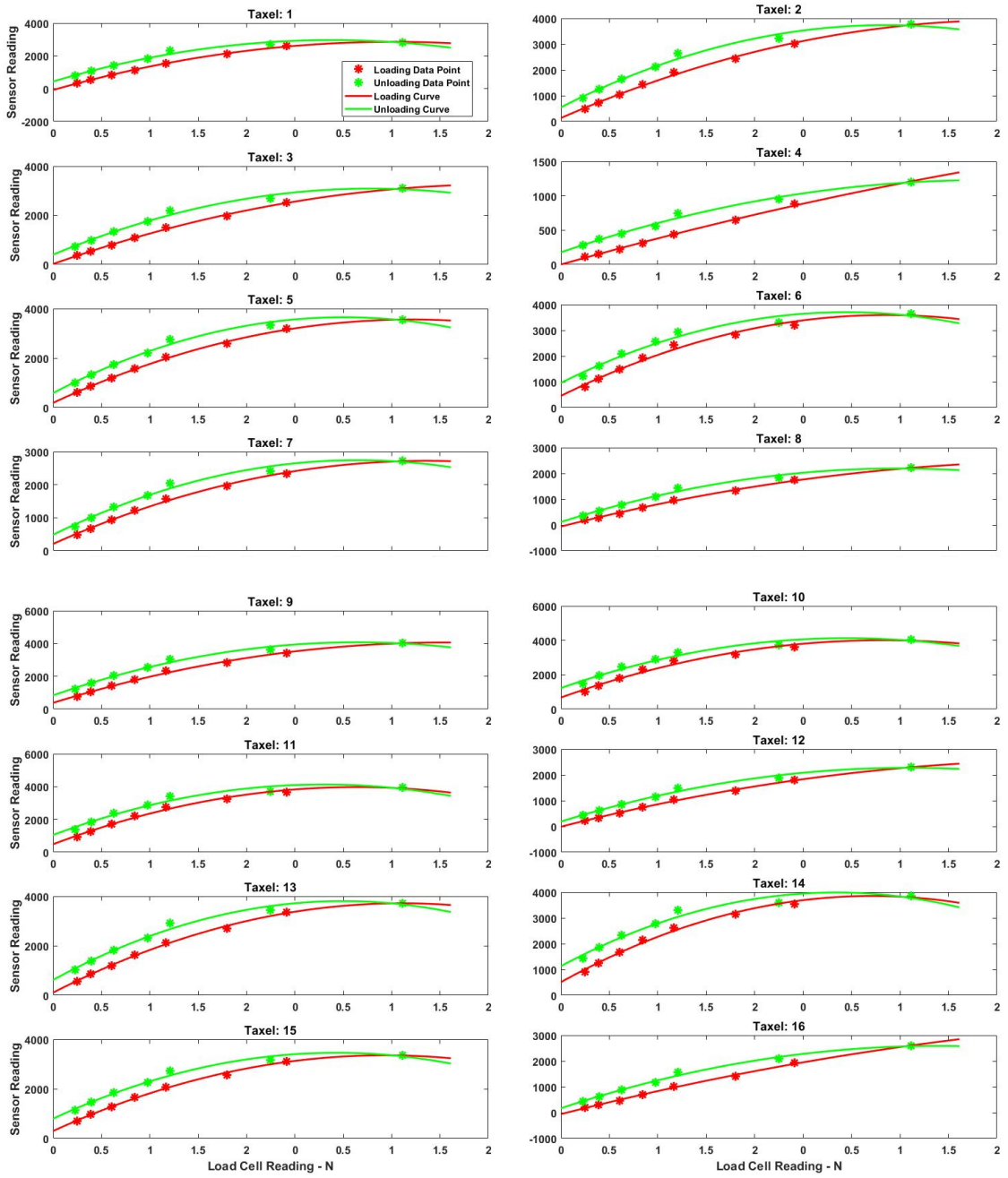


Figure 4.7: Sensor Reading vs. Load Cell Reading: Displacement Step Method

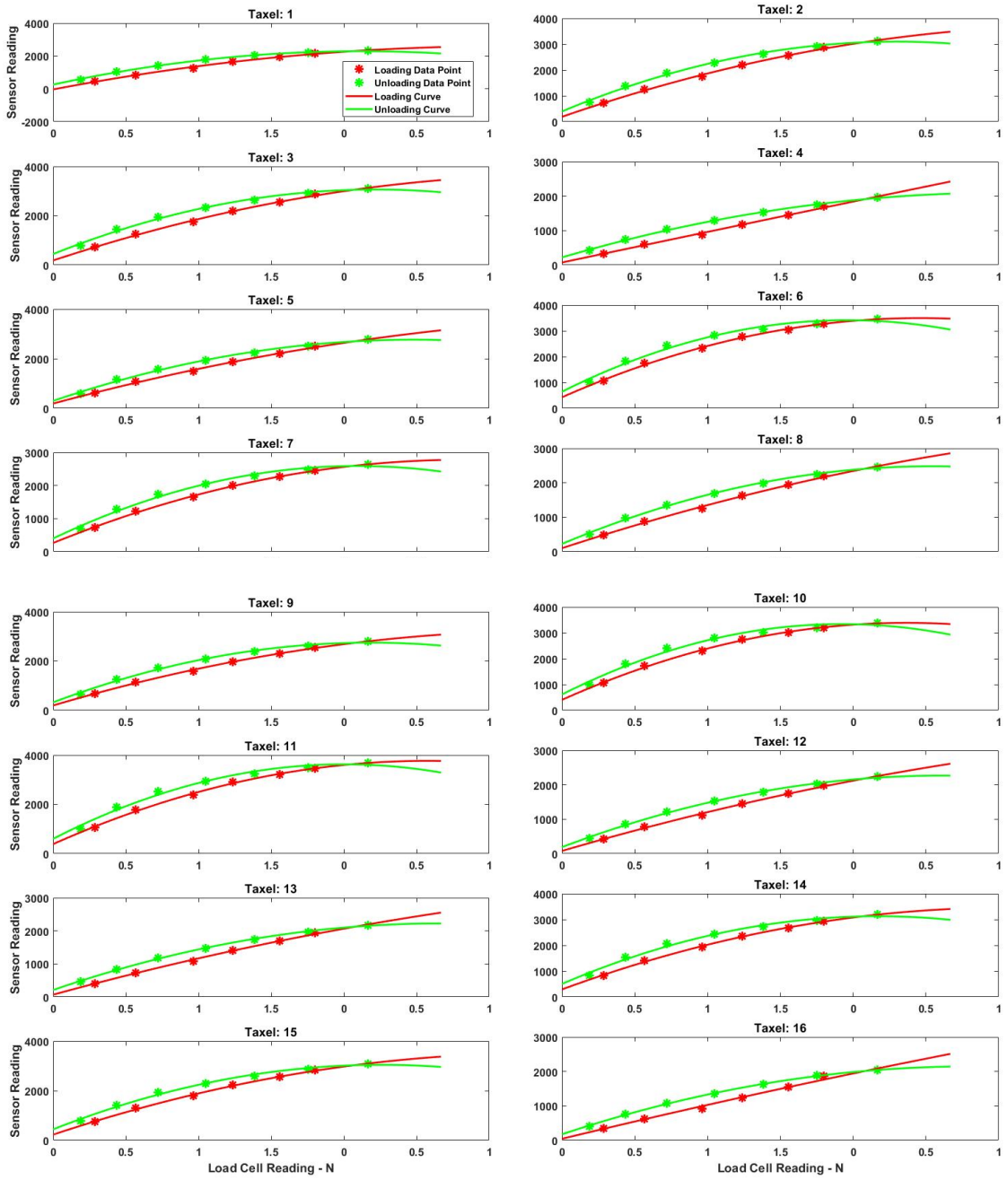
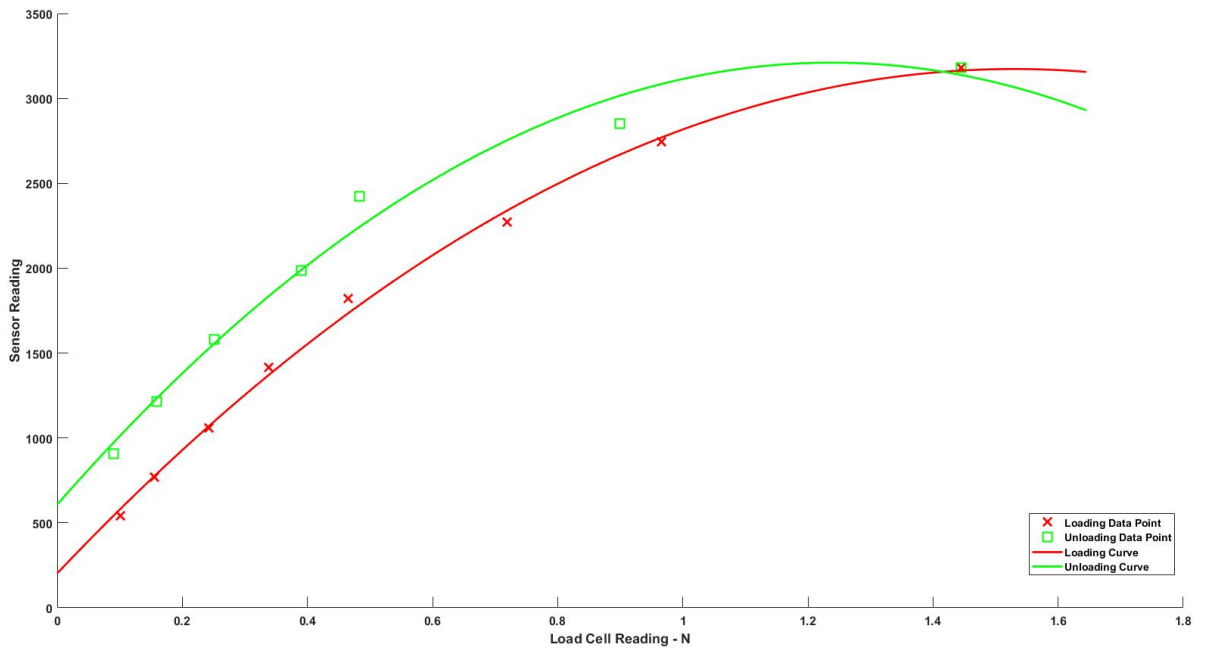
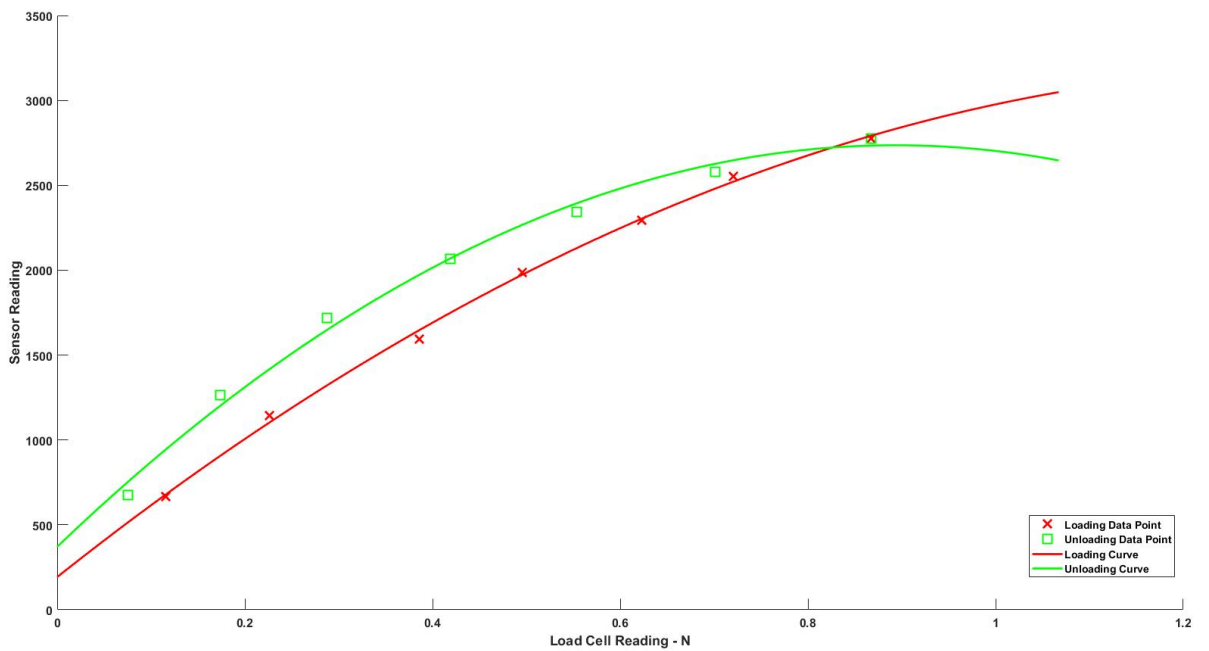


Figure 4.8: Sensor Reading vs. Load Cell Reading: Force Step Method

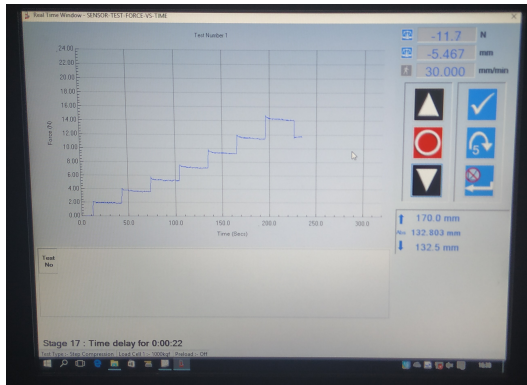


(a) Sensor Reading vs. Load Cell Reading: Displacement Step Method–Average Values

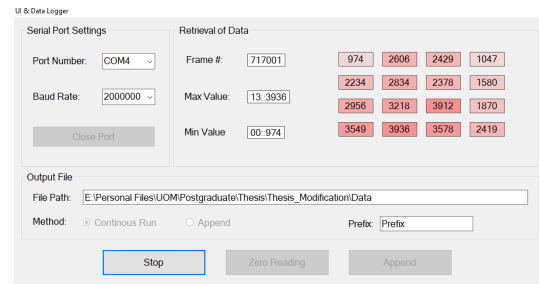


(b) Sensor Reading vs. Load Cell Reading: Force Step Method–Average Values

Figure 4.9: Generalized Characterization for the Sensor



(a)



(b)

Figure 4.10: (a) Graph being drawn on WinTest Screen (b) Data Logger App recording data

4.3 Analysis

For displacement and force step methods, each taxel reading and corresponding load cell reading was plotted against time. Data sets from different orientations were averaged prior to that. During the displacement step method, the maximum force reported by the orientations 1 & 4 were greater than that of 2 & 3. Due to this discrepancy, only the results for the highest forces (orientations 1 & 4) were presented. However results for orientations 2 & 3 depicted similar behavior. Refer to Figures 4.5 & 4.6.

The load cell was not sensitive to the lower end of force spectrum the tactile sensor was sensitive to. Therefore this region had to be excluded during the analysis. This was a limitation of the experiment.

Then each taxel reading was plotted against the corresponding load point for both methods. Polynomial regression has been applied to obtain a correlation between the sensor reading and applied load. Refer to Figures 4.7 & 4.8. The amount of correlation (R-Squared value) and taxel hysteresis has been calculated using this data. Refer to tables 4.1 & 4.2.

To obtain a generalized result, readings from each sensor were averaged. Those averaged data points were plotted against corresponding force values as in Figures 4.9a & 4.9b. Through these calculations, average values for hysteresis and R-Squared values were obtained for the sensor. Refer to Table 4.5.

An impairment of correlation between sensor readings and applied force values is evident through reduced R-Squared values during unloading. This is due to the hysteresis caused by material properties of the silicon elastomer. Silicon is a viscoelastic material, thus takes time to restore after deformation. However, response to compression was rather quick albeit the opposite during relaxation.

Best regression fit was obtained using a second order polynomial equation. The coefficients of each equation can be used to characterize the relation between applied force and sensor reading for each taxel. Refer to Tables 4.3 & 4.4. A generalization of these values for all taxels was also calculated using mean values of sensor readings. Refer to Table 4.5.

This non linearity was introduced by the change in magnetic fields that vary with distance coupled by the elastic properties of the elastomer. Even though the hall sensor responds linearly to changing magnetic fields, above factors changed the linear response.

4.4 Drift and Noise Characteristics

The drift of each taxel was tested using two methods. During one method, the taxel was allowed to drift in no load state for 2 hours. Taxel output was logged every 1 second. During the second method, a 0.5N force was constantly applied on the taxel and allowed to drift for 2 hours. Same as before, taxel output was logged in 1 second intervals.

During the no load phase, no change in sensor output was noticed for the first

Taxel No.	Displacement Step Method %	Force Step Method %
1	10.92	7.75
2	14.49	11.38
3	13.37	12.29
4	11.2	8.83
5	13.16	9.84
6	12.66	10.58
7	8.8	8.69
8	7.02	9.57
9	12	11.12
10	11.05	10.23
11	11.32	11.73
12	6.83	8.66
13	14.08	8.17
14	15.55	10.45
15	12.59	10.38
16	8.77	9.24

Table 4.1: Tactile Sensor: Hysteresis values of each taxel

Taxel No.	Displacement Step Method		Force Step Method	
	Loading	Unloading	Loading	Unloading
1	0.94	0.84	0.98	0.92
2	0.98	0.93	0.99	0.94
3	0.98	0.92	0.99	0.93
4	1	0.97	1	0.98
5	0.95	0.87	0.99	0.96
6	0.93	0.86	0.96	0.88
7	0.96	0.9	0.97	0.91
8	0.99	0.94	1	0.96
9	0.97	0.9	0.99	0.93
10	0.92	0.86	0.95	0.86
11	0.9	0.81	0.96	0.89
12	0.99	0.94	1	0.97
13	0.95	0.87	1	0.97
14	0.91	0.83	0.98	0.92
15	0.93	0.85	0.99	0.94
16	1	0.96	1	0.97

Table 4.2: Tactile Sensor: R-Squared values of regression lines

Taxel No.	Loading			Unloading		
	a	b	c	a	b	c
1	-1482.40	4175.24	-82.71	-1905.16	4389.49	436.26
2	-1099.00	4086.70	133.47	-1770.57	4751.88	548.42
3	-924.69	3463.53	22.32	-1554.29	4086.91	402.68
4	-107.13	991.82	0.29	-343.04	1200.61	178.07
5	-1531.57	4541.86	191.67	-2120.64	5098.42	586.69
6	-1739.17	4673.16	453.73	-1980.71	4662.77	960.17
7	-1055.53	3260.30	205.58	-1427.03	3590.92	483.87
8	-559.55	2385.18	-63.30	-1069.28	2981.91	113.24
9	-1397.19	4536.46	382.16	-2046.08	5147.79	838.11
10	-1885.66	5016.11	672.93	-2088.52	4925.55	1225.48
11	-2216.42	5561.07	483.72	-2474.60	5522.35	1049.65
12	-553.29	2396.55	-10.94	-1010.86	2904.12	189.56
13	-1731.19	4999.48	107.00	-2218.11	5316.62	618.50
14	-2034.29	5217.64	508.10	-2215.33	5031.76	1130.22
15	-1622.39	4455.71	296.33	-1942.47	4550.21	793.06
16	-374.82	2383.84	-59.29	-998.57	3108.71	168.76

Table 4.3: Coefficients list for the quadratic regression functions obtained for loading and unloading phases of displacement step method

Taxel No.	Loading			Unloading		
	a	b	c	a	b	c
1	-1688.90	4218.59	-36.96	-2830.36	4798.10	256.94
2	-1659.81	4860.06	187.14	-3204.52	5887.57	394.55
3	-1713.40	4887.47	182.81	-3329.02	5906.09	444.37
4	-26.20	2232.06	72.15	-1271.43	3091.24	220.21
5	-1085.06	3926.37	192.39	-2513.77	4983.29	297.99
6	-3168.75	6236.79	426.41	-4514.72	7075.94	640.77
7	-1967.08	4450.35	261.92	-3138.14	5247.61	397.13
8	-816.66	3456.44	99.73	-2183.23	4439.74	224.12
9	-1556.68	4357.06	196.04	-3183.85	5558.32	322.57
10	-3326.99	6302.28	403.88	-4609.56	7093.22	611.44
11	-3192.37	6569.58	387.26	-4714.51	7554.02	601.08
12	-664.10	3083.13	77.82	-1912.38	3986.71	188.76
13	-631.48	2999.97	68.84	-1768.59	3773.88	211.05
14	-2109.47	5170.30	291.72	-3484.05	6047.22	503.60
15	-1811.15	4880.02	227.95	-3195.31	5767.95	441.47
16	-223.73	2550.64	43.59	-1561.63	3509.33	174.53

Table 4.4: Coefficients list for the quadratic regression functions obtained for loading and unloading phases of force step method

Average from all taxels	Displacement Step Method		Force Step Method	
	Loading	Unloading	Loading	Unloading
Hysteresis		13.29		11.49
R-Squared Value	0.96	0.89	0.99	0.93

Table 4.5: Hysteresis and R-Squared values calculated from the mean of all data

	Displacement Step Method		Force Step Method	
	Loading	Unloading	Loading	Unloading
a	-1269.64	-1697.83	-1602.61	-2963.44
b	3884.04	4204.38	4386.32	5295.01
c	202.57	607.67	192.67	370.66

Table 4.6: Coefficients of the quadratic regression function obtained using the mean of all data

5000 seconds. During the remaining period of time, sensor drift appeared in all four hall sensors. During the loaded phase, no considerable change in output was observed upto 6000 seconds.

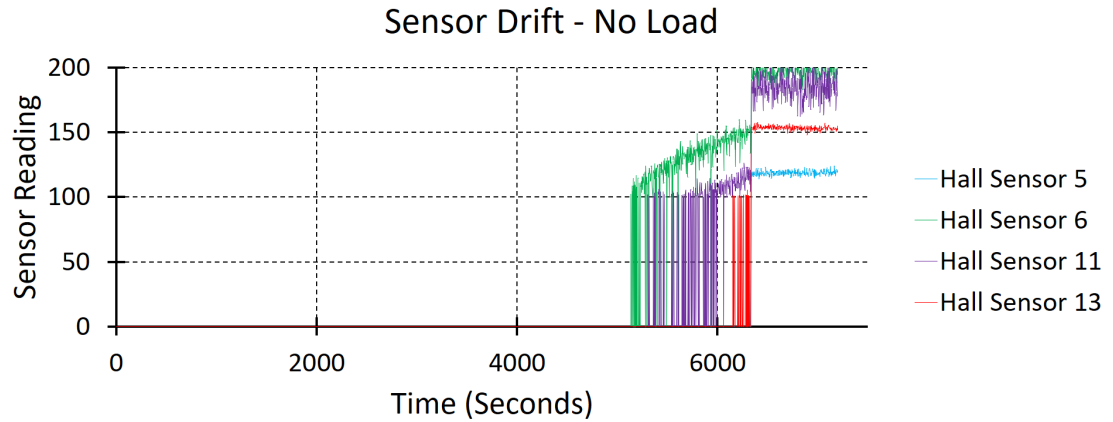


Figure 4.11: Sensor Drift - No load

According to manufacturer's specifications ss39et is a reasonably stable sensor with minimum drift. The change in output is between $\pm 0.1\% \text{C}^{-1}$ [101]. These experiments were carried out in a temperature controlled environment (air-conditioned) minimizing the amount of drift introduced by changes in environmental temperature. Thus drift evident in Figure 4.11 is almost related to the

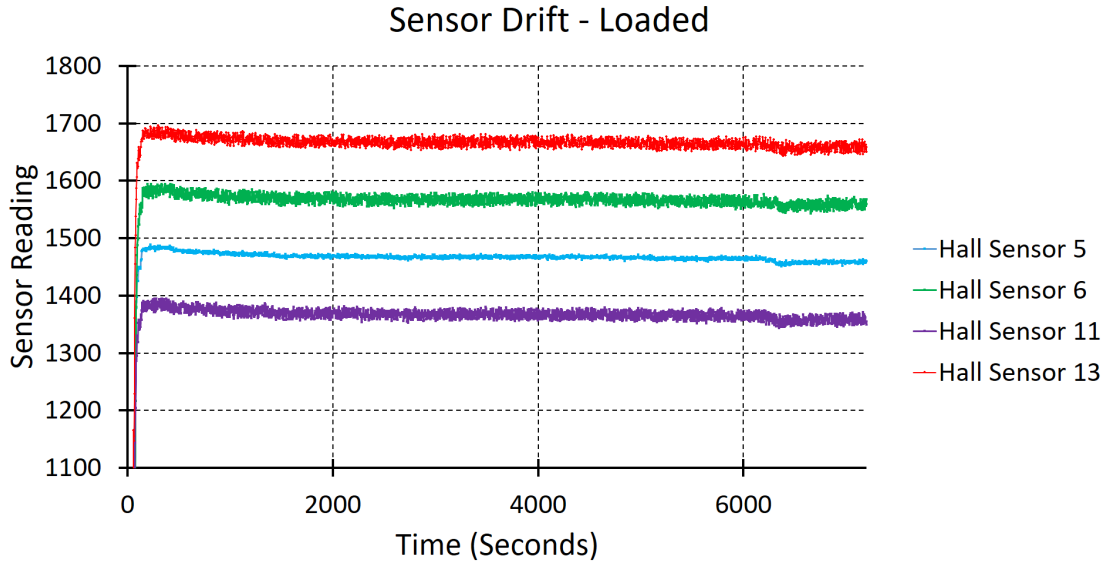


Figure 4.12: Sensor Drift - 0.5N Force

heating of sensor elements along with time.

When referring to Figures 4.11 & 4.12, scale on the Y-Axis should be noted. Though not visible, drift similar to Figure 4.11 might be present in Figure 4.12 appearing as only minor fluctuations disregarded as noise, due to multiples of magnitude in signal reading compared to no load state.

4.5 Super-resolution

Super-resolution is a simple yet effective mechanism that can be used to enhance the details of an array of data, similar to oversampling a signal. This interpolation technique can compensate for finer details that were lost due to limitations in sampling such as low-resolution.

In the context of this tactile sensor, this method can be applied to approximate a contact location with increased accuracy. For an example, consider the following scenario. A point force is applied on the elastomer on some location; for convenience assume the location is on center.

As taxels are separated by 10mm apart, no one taxel is directly behind this point force. So there is no way of telling where this force is applied, even though each taxel gives separate readings of their own. Refer to Figure 4.13.

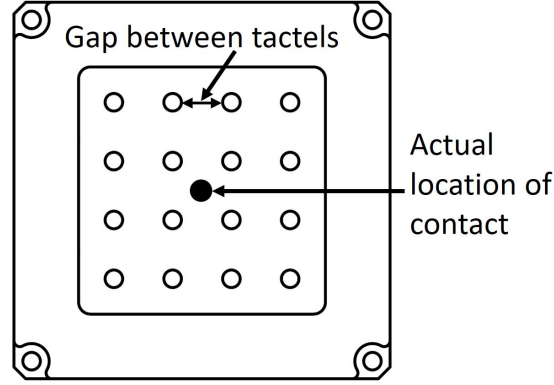


Figure 4.13: Point of application of force vs. Taxel arrangement

By taking Center of Gravity (CoG) of pressure distribution over the entire array of readings, a single point can be identified where all the readings are pointing to. This result is also known as the resultant point of contact. Refer to Equations 4.1 & 4.2.

$$P_x = \frac{\sum_{i=1}^n h_i x_i}{\sum_{i=1}^n h_i} \quad (4.1) \quad P_y = \frac{\sum_{i=1}^n h_i y_i}{\sum_{i=1}^n h_i} \quad (4.2)$$

where:

- P_x & P_y X & Y Coordinates of CoG
- h_i Signal output from i^{th} hall sensor
- x_i & y_i X & Y Coordinates of i^{th} taxel
- n Number of taxels

A typical implementation is as follows. Refer to Algorithm 4.

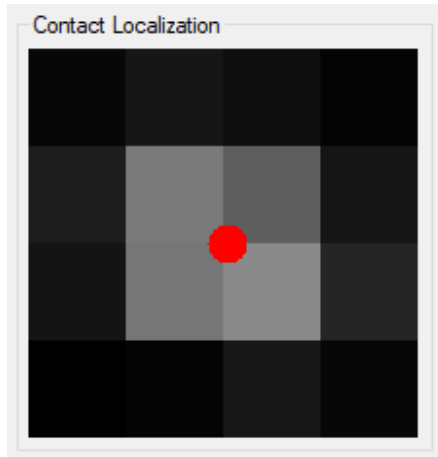


Figure 4.14: A point force applied on center—The Image is 200×200 pixels with each square being 50×50 pixels. The Greyness i.e. color value is proportional to taxel reading

For a visual depiction of the result, Refer to Figure 4.14. The visual representation depicted here is obtained through a custom Graphical User Interface (GUI) designed for the sensor using the .NET Framework. The UI acquires encoded tactile sensor readings through the Universal Serial Bus (USB) Protocol, decodes the data and displays them on screen. It simultaneously calculates the CoG of each data set (16 values) and draws it as an image on the UI.

The gray scale squares displayed correspond to the tactile data values. At the maximum reading (8192) it displays a white square (Gray Value 255) and at the minimum reading (0) it displays a black square (Gray Value 0). It should be noted that the actual hall sensor is placed at the middle of each square thus the gray square is only a pictorial presentation of the hall sensor reading. Refer to Figure 4.15.

The mechanism has been validated by cross checking the point of application of force (applied using a pointy device such as a pen) against the position approximated by the algorithm. Also the tip was guided on the elastomer to see how the red dot behaves with the movement of pen. A visually acceptable and stable correlation is present that can be used for further Research and Development purposes.

Algorithm 4: CoG Calculation

Data: Number of taxels: n

Pitch of the taxel array: d

Result: X & Y Coordinates of CoG: PX & PY

```
1 begin
  /* n-dimensional null vectors */
2  x[n] ← (0...0)
3  y[n] ← (0...0)
4  h[n] ← (0...0)
  /* Generate X & Y coordinates of each taxel from a common
     origin (Top Left) */
5  for i ← 0 to (n - 1) do
    /* runs for i=0,1,...,(n-1) */
6    x[i + 1] ←  $\frac{d}{2} + (i \% 4) * d$  // % denotes modulus operator
7    y[i + 1] ←  $\frac{d}{2} + \mathbf{floor}(i \div 4) * d$  // 'floor' denotes the
    mathematical functions under same name
8  h[n] ←  $\Lambda(\phi)$  // where  $\Lambda$  is some function that returns an
    n-dimensional vector of values for hall sensor readings.
    This data is obtained through a DAQ Routine  $\phi$ 
  /* Solve the Equations 4.1 & 4.2 stated above */
9  ZigmaHX, ZigmaHY, ZigmaH ← 0
10 for j ← 1 to n do
11   ZigmaHX ← ZigmaHX + x[j] * h[j]
12   ZigmaHY ← ZigmaHY + y[j] * h[j]
13   ZigmaH = ZigmaH + h[j]
14 PX ← ZigmaHX / ZigmaH
15 PY ← ZigmaHY / ZigmaH
```

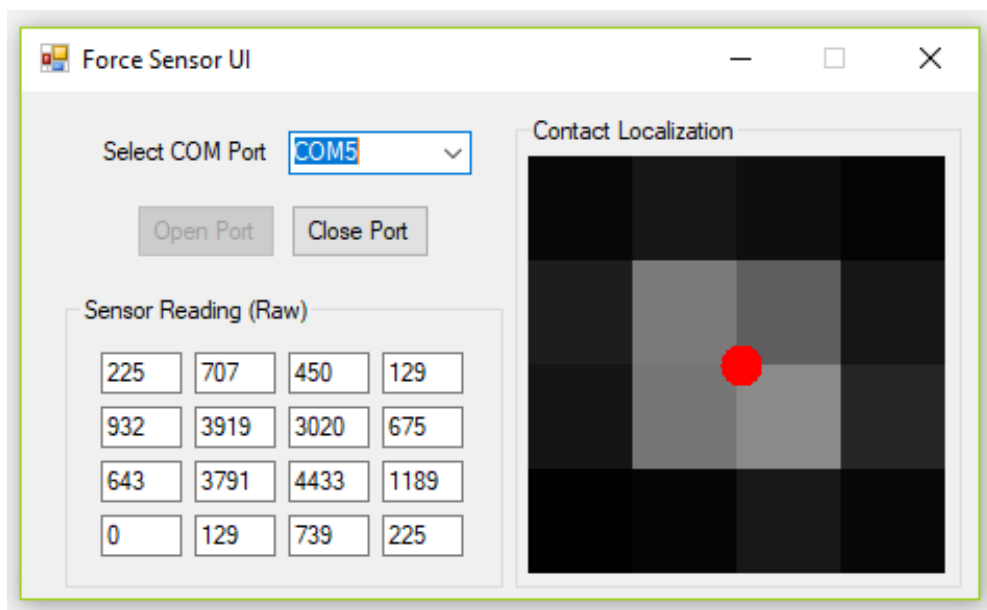


Figure 4.15: User Interface–Communication Port 5 (COM5) is opened. Sensor readings are displayed in a 4×4 array of text boxes

CONCLUSION AND FUTURE DIRECTIONS

5.1 Conclusion

In this thesis, the development and characterization of a tactile array sensor for parallel grippers for use in object manipulation was presented. It uses an array of magnets embedded in a flexible elastomer to generate a varying magnetic field when the elastomer is pressed against an object. The variation of the magnetic field is captured by a similar array of hall sensors. The signal output from hall sensors is then processed to measure tactile forces acting between the contact surfaces.

The sensor's performance was tested using a Universal Testing Machine. Sensor's behavior on step displacement of elastomer and step force on elastomer were studied. All taxels were experimented individually and findings were generalized.

Average hysteresis for all taxels were 13.29% for displacement step method and 11.49% for force step method. This was due to the delayed elastic strain recovery of the silicon elastomer. It is a common characteristic of silicon based materials [106].

The best regression fit for the sensor data was obtained through a second order polynomial. Even though hall sensors responded linearly to change in magnetic fields, the overall behavior had become non linear. This was due to the non-linearity introduced by viscoelastic properties of the elastomer and variation of

magnetic field densities inside the elastomer.

The load cell of the Universal Testing Machine was sensitive only for a limited range of the force spectrum felt by the tactile sensor. Therefore the results had to be trimmed in order to isolate the sensing area of both sensors. This was a limitation of the experiment.

The sensor cannot be used to measure forces when magnetic materials are imposed on the elastomer. This is because the hall sensor array's readings are disturbed by the external magnetic fields. Inevitably strong magnetic fields can also limit the performance of the sensor.

5.2 Future Directions

The end goal of developing tactile sensors is to utilize them in providing feedback during object manipulation. Thus object manipulation should be studied using this gripper and attached tactile sensors. Consequently, knowledge can be obtained on how to better perform such manipulation tasks, allowing future improvements to be made.

Though the silicon elastomer is flexible, the rest of the package is not. Therefore its compliance over curved surfaces is limited. More compliant the sensor is, the more information it can gather about the grasp.

The sensor can be made more compliant by placing the hall sensor array inside the silicon elastomer as well (parallel to magnet array with layers of separation between them). Hall sensor array can be developed on flexible PCB so that the circuit stays robust under multiple deformations. By adopting this method, the sensor might work well with an object with curved surfaces and may even increase its sensitivity.

The most interesting development of this sensor would be to build such a flex-

ible sensor as described above and integrate it into a finger tip. The flexible sensor should be built in the shape of a finger tip than wrapping a planar tactile array around the tip. So when the finger tip touches an object, the small flexible magnetic tactile array residing inside the finger tip will deform and give readings similar to that of given by human tactile nerve endings. This would be a tremendous improvement over what is presented in this thesis; to lay the foundation for greater technology to come.

LIST OF PUBLICATIONS

- L. Weerasinghe and D. S. Chathuranga, "Development and Characterization of a Soft Tactile Sensor Array Used for Parallel Grippers," 2018 Moratuwa Engineering Research Conference (MERCon), Moratuwa, 2018, pp. 102-107.

BIBLIOGRAPHY

- [1] C. Chi, X. Sun, N. Xue, T. Li, and C. Liu, “Recent Progress in Technologies for Tactile Sensors,” *Sensors (Basel)*, apr 2018.
- [2] R. S. Dahiya and M. Valle, *Robotic Tactile Sensing*. Dordrecht: Springer Netherlands, 2013. [Online]. Available: <http://link.springer.com/10.1007/978-94-007-0579-1>
- [3] S. A. Wall and S. Brewster, “Sensory substitution using tactile pin arrays: Human factors, technology and applications,” *Signal Processing*, vol. 86, no. 12, pp. 3674–3695, 2006.
- [4] M. Park, B. G. Bok, J. H. Ahn, and M. S. Kim, “Recent advances in tactile sensing technology,” *Micromachines*, vol. 9, no. 7, 2018.
- [5] M. I. Tiwana, S. J. Redmond, and N. H. Lovell, “A review of tactile sensing technologies with applications in biomedical engineering,” *Sensors and Actuators, A: Physical*, vol. 179, pp. 17–31, 2012. [Online]. Available: <http://dx.doi.org/10.1016/j.sna.2012.02.051>
- [6] M. Sergio, N. Manaresi, M. Tartagni, R. Guerrieri, and R. Canegallo, “A textile based capacitance pressure sensor,” *Ieee*, p. 1625, 2002.
- [7] Y. M. Shkel and N. J. Ferrier, “Electrostriction enhancement of solid-state capacitance sensing,” *IEEE/ASME Transactions on Mechatronics*, vol. 8, no. 3, pp. 318–325, 2003.
- [8] K. Arshak, D. Morris, O. Korostynska, E. Jafer, A. Arshak, J. Harris, S. Clifford, and G. Lyons, “Novel silicone-based capacitive pressure sensors

- with high sensitivity for biomedical applications,” *E-Polymers*, no. 061, pp. 1–11, 2004.
- [9] C. T. Ko, S. H. Tseng, and M. S. Lu, “A CMOS micromachined capacitive tactile sensor with high-frequency output,” *Journal of Microelectromechanical Systems*, vol. 15, no. 6, pp. 1708–1714, 2006.
- [10] T. Salo, T. Vančura, and H. Baltes, “CMOS-sealed membrane capacitors for medical tactile sensors,” *Journal of Micromechanics and Microengineering*, vol. 16, no. 4, pp. 769–778, 2006.
- [11] A. Schmitz, M. Maggiali, M. Randazzo, L. Natale, and G. Metta, “A prototype fingertip with high spatial resolution pressure sensing for the robot iCub,” *2008 8th IEEE-RAS International Conference on Humanoid Robots, Humanoids 2008*, pp. 423–428, 2008.
- [12] A. Shashank, M. I. Tiwana, S. J. Redmond, and N. H. Lovell, “Design, simulation and fabrication of a low cost capacitive tactile shear sensor for a robotic hand,” *Proceedings of the 31st Annual International Conference of the IEEE Engineering in Medicine and Biology Society: Engineering the Future of Biomedicine, EMBC 2009*, pp. 4132–4135, 2009.
- [13] C. C. Chen, P. Z. Chang, and W. P. Shih, “Flexible tactile sensor with high sensitivity utilizing botanical epidermal cell natural micro-structures,” *Proceedings of IEEE Sensors*, pp. 0–3, 2012.
- [14] J. A. Dobrzynska and M. A. M. Gijs, “Polymer-based flexible capacitive sensor for three-axial force measurements,” *Journal of Micromechanics and Microengineering*, vol. 23, no. 1, p. 015009, jan 2013. [Online]. Available: <http://stacks.iop.org/0960-1317/23/i=1/a=015009?key=crossref.a8ead82b12ca40867badfbdba79653f2>
- [15] B. C.-K. Tee, A. Chortos, R. R. Dunn, G. Schwartz, E. Eason, and Z. Bao, “Tunable Flexible Pressure Sensors using Microstructured

- Elastomer Geometries for Intuitive Electronics,” *Advanced Functional Materials*, vol. 24, no. 34, pp. 5427–5434, sep 2014. [Online]. Available: <http://doi.wiley.com/10.1002/adfm.201400712>
- [16] G. Liang, Y. Wang, D. Mei, K. Xi, and Z. Chen, “Flexible Capacitive Tactile Sensor Array with Truncated Pyramids as Dielectric Layer for Three-Axis Force Measurement,” *Journal of Microelectromechanical Systems*, vol. 24, no. 5, pp. 1510–1519, 2015.
- [17] A. Charalambides and S. Bergbreiter, “A novel all-elastomer MEMS tactile sensor for high dynamic range shear and normal force sensing,” *Journal of Micromechanics and Microengineering*, vol. 25, no. 9, p. 95009, 2015. [Online]. Available: <http://dx.doi.org/10.1088/0960-1317/25/9/095009>
- [18] A. Rana, J. P. Roberge, and V. Duchaine, “An Improved Soft Dielectric for a Highly Sensitive Capacitive Tactile Sensor,” *IEEE Sensors Journal*, vol. 16, no. 22, pp. 7853–7863, 2016.
- [19] S. Denei, P. Maiolino, E. Baglini, and G. Cannata, “Development of an Integrated Tactile Sensor System for Clothes Manipulation and Classification Using Industrial Grippers,” *IEEE Sensors Journal*, vol. 17, no. 19, pp. 6385–6396, 2017.
- [20] T. Paulino, P. Ribeiro, M. Neto, S. Cardoso, A. Schmitz, J. Santos-Victor, A. Bernardino, and L. Jamone, “Low-cost 3-axis soft tactile sensors for the human-friendly robot Vizzy,” in *2017 IEEE International Conference on Robotics and Automation (ICRA)*, may 2017, pp. 966–971.
- [21] P. J. Kyberd and P. H. Chappell, “A force sensor for automatic manipulation based on the Hall effect,” *Measurement Science and Technology*, vol. 4, no. 3, pp. 281–287, 1993.
- [22] L. Jamone, L. Natale, G. Metta, and G. Sandini, “Highly Sensitive Soft Tactile Sensors for an Anthropomorphic Robotic Hand,” *IEEE Sensors Journal*, vol. 15, no. 8, pp. 4226–4233, aug 2015.

- [23] A. Alfadhel and J. Kosel, "Magnetic Nanocomposite Cilia Tactile Sensor," *Advanced Materials*, vol. 27, no. 47, pp. 7888–7892, dec 2015. [Online]. Available: <http://doi.wiley.com/10.1002/adma.201504015>
- [24] D. Li and K. Shida, "Monostructure touch sensor with multifunction for discrimination of material properties," *Electrical Engineering in Japan (English translation of Denki Gakkai Ronbunshi)*, vol. 117, no. 3, pp. 68–75, 1996.
- [25] N. Futai, N. Futai, K. Matsumoto, and I. Shimoyama, "A flexible micro-machined planar spiral inductor for use as an artificial tactile mechanoreceptor," *Sensors and Actuators, A: Physical*, vol. 111, no. 2-3, pp. 293–303, 2004.
- [26] X. Chen, S. Yang, and S. Motojima, "Preparation and property of novel CMC tactile sensors," *Sensors And Actuators*, vol. 2, no. 2, pp. 289–292, 2005.
- [27] X. Chen, S. Yang, M. Hasegawa, K. Takeuchi, K. Kawabe, and S. Motojima, "Novel Tactile Sensors Manufactured by Carbon Microcoils," in *2004 International Conference on MEMS, NANO and Smart Systems (ICMENS'04)*, no. Cmc. IEEE, 2006, pp. 486–491. [Online]. Available: <http://ieeexplore.ieee.org/document/1508998/>
- [28] X. Chen, J. Sakai, S. Yang, and S. Motojima, "Biomimetic Tactile Sensors with Fingerprint-Type Surface Made of Carbon Microcoils/Polysilicone," *Japanese Journal of Applied Physics*, vol. 45, no. No. 37, pp. L1019–L1021, sep 2006. [Online]. Available: <http://stacks.iop.org/1347-4065/45/L1019>
- [29] S. Motojima and X. Chen, "Preparation and characterization of carbon microcoils (CMCs)," *Bulletin of the Chemical Society of Japan*, vol. 80, no. 3, pp. 449–455, 2007.

- [30] S. Takenawa, “A soft three-axis tactile sensor based on electromagnetic induction,” *IEEE 2009 International Conference on Mechatronics, ICM 2009*, no. April, 2009.
- [31] S. Wattanasarn, K. Noda, K. Matsumoto, and I. Shimoyama, “3D flexible tactile sensor using electromagnetic induction coils,” in *2012 IEEE 25th International Conference on Micro Electro Mechanical Systems (MEMS)*. IEEE, jan 2012, pp. 488–491. [Online]. Available: <http://ieeexplore.ieee.org/document/6170230/>
- [32] M. Ohka, Y. Mitsuya, I. Higashioka, and H. Kabeshita, “An experimental optical three-axis tactile sensor for micro-robots,” *Robotica*, vol. 23, no. 4, pp. 457–465, 2005.
- [33] P. Piacenza, W. Dang, E. Hannigan, J. Espinal, I. Hussain, I. Kymissis, and M. Ciocarlie, “Accurate contact localization and indentation depth prediction with an optics-based tactile sensor,” *Proceedings - IEEE International Conference on Robotics and Automation*, pp. 959–965, 2017.
- [34] A. Massaro, F. Spano, P. Cazzato, C. La Tegola, R. Cingolani, and A. Athanassiou, “Robot tactile sensing: Gold nanocomposites as highly sensitive real-time optical pressure sensors,” *IEEE Robotics and Automation Magazine*, vol. 20, no. 2, pp. 82–90, 2013.
- [35] M. Ohka, H. Kobayashi, and Y. Mitsuya, “Sensing characteristics of an optical three-axis tactile sensor mounted on a multi-fingered robotic hand,” *2005 IEEE/RSJ International Conference on Intelligent Robots and Systems, IROS*, vol. 22, pp. 1959–1964, 2005.
- [36] D. Z. Tan, Q. M. Wang, R. H. Song, X. Yao, and Y. H. Gu, “Optical fiber based slide tactile sensor for underwater robots,” *Journal of Marine Science and Application*, vol. 7, no. 2, pp. 122–126, 2008.
- [37] H. Kobayashi, H. B. Yussof, N. Morisawa, J. Takata, H. Suzuki, and M. Ohka, “Object exploration and manipulation using a robotic finger

- equipped with an optical three-axis tactile sensor,” *Robotica*, pp. 3425–3430, 2008.
- [38] N. F. Lepora and B. Ward-Cherrier, “Tactile Quality Control With Biomimetic Active Touch,” *IEEE Robotics and Automation Letters*, vol. 1, no. 2, pp. 646–652, 2016.
- [39] M. OHKA, H. KOBAYASHI, J. TAKATA, and Y. MITSUYA, “An Experimental Optical Three-Axis Tactile Sensor Featured with Hemispherical Surface,” *Transactions of the Japan Society of Mechanical Engineers Series C*, vol. 74, no. 742, pp. 1477–1484, 2011.
- [40] R. Windecker, S. Franz, and H. J. Tiziani, “Optical roughness measurements with fringe projection,” *Applied Optics*, vol. 38, no. 13, p. 2837, 2008.
- [41] H. Xie, A. Jiang, L. Seneviratne, and K. Althoefer, “Pixel-based optical fiber tactile force sensor for robot manipulation,” in *2012 IEEE Sensors*. IEEE, oct 2012, pp. 1–4. [Online]. Available: <http://ieeexplore.ieee.org/document/6411462/>
- [42] R. Ahmadi, M. Packirisamy, J. Dargahi, and R. Cecere, “Discretely loaded beam-type optical fiber tactile sensor for tissue manipulation and palpation in minimally invasive robotic surgery,” *IEEE Sensors Journal*, vol. 12, no. 1, pp. 22–32, 2012.
- [43] E. Fujiwara, F. D. Paula, Y. T. Wu, M. F. M. Santos, E. A. Schenkel, and C. K. Suzuki, “Optical fiber tactile sensor based on fiber specklegram analysis,” *25th International Conference on Optical Fiber Sensors*, vol. 10323, p. 103232N, 2017.
- [44] J. H. Kim, J. I. Lee, H. J. Lee, Y. K. Park, M. S. Kim, and D. I. Kang, “Design of flexible tactile sensor based on three-component force and its,” *Proceedings - IEEE International Conference on Robotics and Automation*, vol. 2005, no. April, pp. 2578–2581, 2005.

- [45] K. Kim, K. R. Lee, W. H. Kim, K. B. Park, T. H. Kim, J. S. Kim, and J. J. Pak, “Polymer-based flexible tactile sensor up to 32×32 arrays integrated with interconnection terminals,” *Sensors and Actuators, A: Physical*, vol. 156, no. 2, pp. 284–291, 2009.
- [46] Y. Tanaka, M. Tanaka, and S. Chonan, “Development of a sensor system for collecting tactile information,” *Microsystem Technologies*, vol. 13, no. 8-10, pp. 1005–1013, 2007.
- [47] C. Li, P. M. Wu, S. Lee, A. Gorton, M. J. Schulz, and C. H. Ahn, “Flexible dome and bump shape piezoelectric tactile sensors using PVDF-TrFE copolymer,” *Journal of Microelectromechanical Systems*, vol. 17, no. 2, pp. 334–341, 2008.
- [48] K. Takashima, S. Horie, T. Mukai, K. Ishida, and K. Matsushige, “Piezoelectric properties of vinylidene fluoride oligomer for use in medical tactile sensor applications,” *Sensors and Actuators, A: Physical*, vol. 144, no. 1, pp. 90–96, 2008.
- [49] S. Sokhanvar, M. Packirisamy, and J. Dargahi, “A multifunctional PVDF-based tactile sensor for minimally invasive surgery,” *Smart Materials and Structures*, vol. 16, no. 4, pp. 989–998, 2007.
- [50] M. A. Qasaimeh, S. Sokhanvar, J. Dargahi, and M. Kahrizi, “PVDF-based microfabricated tactile sensor for minimally invasive surgery,” *Journal of Microelectromechanical Systems*, vol. 18, no. 1, pp. 195–207, 2009.
- [51] L. Z.-z. XI Xu-gang, “A Tele-manipulator with Tactile Tele-presence and Myoelectric Bionic Control,” *ROBOT*, vol. 0446, no. 31(3), pp. 270–275, 2009.
- [52] N. Wettels, D. Popovic, V. J. Santos, R. S. Johansson, and G. E. Loeb, “Biomimetic tactile sensor for control of grip,” *2007 IEEE 10th International Conference on Rehabilitation Robotics, ICORR’07*, vol. 00, no. c, pp. 923–932, 2007.

- [53] W. Liu, P. Yu, C. Gu, X. Cheng, and X. Fu, “Fingertip Piezoelectric Tactile Sensor Array for Roughness Encoding Under Varying Scanning Velocity,” *IEEE Sensors Journal*, vol. 17, no. 21, pp. 6867–6879, nov 2017. [Online]. Available: <http://ieeexplore.ieee.org/document/7962146/>
- [54] Y. Zhang and N. Miki, “Erratum: Sensitivity enhancement of a micro-scale biomimetic tactile sensor with epidermal ridges (Journal of Micromechanics and Microengineering (2010) 20 (085012)),” *Journal of Micromechanics and Microengineering*, vol. 20, no. 12, 2010.
- [55] F. Maita, L. Maiolo, A. Minotti, A. Pecora, D. Ricci, G. Metta, G. Scandurra, G. Giusi, C. Ciofi, and G. Fortunato, “Ultraflexible Tactile Piezoelectric Sensor Based on Low-Temperature Polycrystalline Silicon Thin-Film Transistor Technology,” *IEEE Sensors Journal*, vol. 15, no. 7, pp. 3819–3826, jul 2015. [Online]. Available: <http://ieeexplore.ieee.org/document/7029628/>
- [56] M. Sim, Y. Jeong, K. Lee, K. Shin, H. Park, J. I. Sohn, S. N. Cha, and J. E. Jang, “Psychological tactile sensor structure based on piezoelectric sensor arrays,” in *2017 IEEE World Haptics Conference, WHC 2017*. IEEE, jun 2017, pp. 340–345. [Online]. Available: <http://ieeexplore.ieee.org/document/7989925/>
- [57] L. Seminara, L. Pinna, M. Valle, L. Basirico, A. Loi, P. Cosseddu, A. Bonfiglio, A. Ascia, M. Biso, A. Ansaldo, D. Ricci, and G. Metta, “Piezoelectric Polymer Transducer Arrays for Flexible Tactile Sensors,” *IEEE Sensors Journal*, vol. 13, no. 10, pp. 4022–4029, oct 2013. [Online]. Available: <http://ieeexplore.ieee.org/document/6531646/>
- [58] R. Kumar, U. Mehta, and P. Chand, “A Low Cost Linear Force Feedback Control System for a Two-fingered Parallel Configuration Gripper,” *Procedia Computer Science*, vol. 105, no. December 2016, pp. 264–269, 2017. [Online]. Available: <http://dx.doi.org/10.1016/j.procs.2017.01.220>

- [59] X. Liu, Y. Zhu, M. W. Nomani, X. Wen, T. Y. Hsia, and G. Koley, “A highly sensitive pressure sensor using a Au-patterned polydimethylsiloxane membrane for biosensing applications,” *Journal of Micromechanics and Microengineering*, vol. 23, no. 2, 2013.
- [60] R. Kilaru, Z. Celik-Butler, D. P. Butler, and I. E. Gonenli, “NiCr MEMS tactile sensors embedded in polyimide toward smart skin,” *Journal of Microelectromechanical Systems*, vol. 22, no. 2, pp. 349–355, 2013.
- [61] C. C. Wen and W. Fang, “Tuning the sensing range and sensitivity of three axes tactile sensors using the polymer composite membrane,” *Sensors and Actuators, A: Physical*, vol. 145-146, no. 1-2, pp. 14–22, 2008.
- [62] Y. Hu, R. B. Katragadda, H. Tu, Q. Zheng, Y. Li, and Y. Xu, “Bioinspired 3-D tactile sensor for minimally invasive surgery,” *Journal of Microelectromechanical Systems*, vol. 19, no. 6, pp. 1400–1408, 2010.
- [63] S. Pyo, J. I. Lee, M. O. Kim, T. Chung, Y. Oh, S. C. Lim, J. Park, and J. Kim, “Development of a flexible three-axis tactile sensor based on screen-printed carbon nanotube-polymer composite,” *Journal of Micromechanics and Microengineering*, vol. 24, no. 7, 2014.
- [64] M. C. Hsieh, Y. K. Fang, M. S. Ju, G. S. Chen, J. J. Ho, C. H. Yang, P. M. Wu, G. S. Wu, and T. Y. F. Chen, “A contact-type piezoresistive micro-shear stress sensor for above-knee prosthesis application,” *Journal of Microelectromechanical Systems*, vol. 10, no. 1, pp. 121–127, 2001.
- [65] K. Noda, H. Onoe, E. Iwase, K. Matsumoto, and I. Shimoyama, “Flexible tactile sensor for shear stress measurement using transferred sub- μm -thick Si piezoresistive cantilevers,” *Journal of Micromechanics and Microengineering*, vol. 22, no. 11, 2012.
- [66] A. Drimus, G. Kootstra, A. Bilberg, and D. Kragic, “Design of a flexible tactile sensor for classification of rigid and deformable objects,” *Robotics*

- and Autonomous Systems*, vol. 62, no. 1, pp. 3–15, 2014. [Online]. Available: <http://dx.doi.org/10.1016/j.robot.2012.07.021>
- [67] Y. Hasegawa, M. Shikida, T. Shimizu, T. Miyaji, H. Sasaki, K. Sato, and K. Itoigawa, “A micromachined active tactile sensor for hardness detection,” *Sensors and Actuators, A: Physical*, vol. 114, no. 2-3, pp. 141–146, 2004.
- [68] P. Piacenza, Y. Xiao, S. Park, I. Kyriakidis, and M. Ciocarlie, “Contact localization through spatially overlapping piezoresistive signals,” *IEEE International Conference on Intelligent Robots and Systems*, vol. 2016-Novem, pp. 195–201, 2016.
- [69] C. Schurmann, R. Kõiva, R. Haschke, and H. Ritter, “A modular high-speed tactile sensor for human manipulation research,” in *2011 IEEE World Haptics Conference*. IEEE, jun 2011, pp. 339–344. [Online]. Available: <http://ieeexplore.ieee.org/document/5945509/>
- [70] G. Westheimer, “Optical superresolution and visual hyperacuity,” *Progress in Retinal and Eye Research*, vol. 31, no. 5, pp. 467–480, 2012. [Online]. Available: <http://dx.doi.org/10.1016/j.preteyeres.2012.05.001>
- [71] D. J. Van Den Heever, K. Schreve, and C. Scheffer, “Tactile sensing using force sensing resistors and a super-resolution algorithm,” *IEEE Sensors Journal*, vol. 9, no. 1, pp. 29–35, 2009.
- [72] N. F. Lepora, U. Martinez-Hernandez, M. Evans, L. Natale, G. Metta, and T. J. Prescott, “Tactile Superresolution and Biomimetic Hyperacuity,” *IEEE Transactions on Robotics*, vol. 31, no. 3, pp. 605–618, jun 2015. [Online]. Available: <http://ieeexplore.ieee.org/document/7078841/>
- [73] O. K. Bruno Siciliano, “Springer handbook of robotics,” *Choice Reviews Online*, vol. 46, no. 06, pp. 46–3272–46–3272, feb 2009. [Online]. Available: <http://choicereviews.org/review/10.5860/CHOICE.46-3272>

- [74] G. J. Monkman, S. Hesse, R. Steinmann, and H. Schunk, *Robot Grippers*. Wiley, oct 2006. [Online]. Available: <https://onlinelibrary.wiley.com/doi/book/10.1002/9783527610280>
- [75] J. Krüger, T. K. Lien, and A. Verl, “Cooperation of human and machines in assembly lines,” *CIRP Annals - Manufacturing Technology*, vol. 58, no. 2, pp. 628–646, 2009.
- [76] G. Fantoni, M. Santochi, G. Dini, K. Tracht, B. Scholz-Reiter, J. Fleischer, T. Kristoffer Lien, G. Seliger, G. Reinhart, J. Franke, H. Nørgaard Hansen, and A. Verl, “Grasping devices and methods in automated production processes,” *CIRP Annals - Manufacturing Technology*, vol. 63, no. 2, pp. 679–701, 2014. [Online]. Available: <http://dx.doi.org/10.1016/j.cirp.2014.05.006>
- [77] A. Bertelsen, J. Melo, E. Sánchez, and D. Borro, “A review of surgical robots for spinal interventions,” *The International Journal of Medical Robotics and Computer Assisted Surgery*, vol. 9, no. 4, pp. 407–422, dec 2013. [Online]. Available: <http://doi.wiley.com/10.1002/rcs.1469>
- [78] G. Hirzinger, B. Brunner, K. Landzettel, and J. Schott, “Preparing a new generation of space robots - A survey of research at DLR,” *Robotics and Autonomous Systems*, vol. 23, no. 1-2, pp. 99–106, 1998.
- [79] K. Tai, A.-R. El-Sayed, M. Shahriari, M. Biglarbegian, and S. Mahmud, “State of the Art Robotic Grippers and Applications,” *Robotics*, vol. 5, no. 2, p. 11, 2016.
- [80] S. Raval and B. Patel, “A Review on Grasping Principle and Robotic Grippers,” *International Journal of Engineering Development and Research*, vol. 4, no. December, pp. 483–490, 2016.
- [81] “2 Jaw Penumatic Gripper - KG SCHUNK GmbH & Co.” Germany, 2019. [Online]. Available: <http://www.directindustry.com/prod/schunk/product-12463-551794.html>

- [82] “3 Jaw Pnuematic Gripper - KG SCHUNK GmbH & Co.” Germany, 2019. [Online]. Available: <http://www.directindustry.com/prod/schunk-gmbh-co-kg/product-7038-1841232.html>
- [83] R. J. Ellwood, A. Raatz, and J. Hesselbach, “Vision and force sensing to decrease assembly uncertainty,” *IFIP Advances in Information and Communication Technology*, vol. 315, pp. 123–130, 2010.
- [84] A. I. Elizarov and N. G. Shein, “The use of production robots in the production of plate heat exchangers,” *Chemical and Petroleum Engineering*, vol. 18, no. 2, pp. 54–56, feb 1982. [Online]. Available: <http://link.springer.com/10.1007/BF01176531>
- [85] S. Yu and M. Gil, “Manipulator handling device for assembly of large-size panels,” *Assembly Automation*, vol. 32, no. 4, pp. 361–372, 2012.
- [86] G. J. Monkman, “Automated handling of packaging materials,” 1993, pp. 16–19.
- [87] “Efficient robotic packing speeds soft drinks manufacture,” *Industrial Robot: An International Journal*, vol. 29, no. 3, p. ir.2002.04929caf.005, jun 2002. [Online]. Available: <https://doi.org/10.1108/ir.2002.04929caf.005><http://www.emeraldinsight.com/doi/10.1108/ir.2002.04929caf.005>
- [88] A. H. Zahraee, J. K. Paik, J. Szewczyk, and G. Morel, “Toward the development of a hand-held surgical robot for laparoscopy,” *IEEE/ASME Transactions on Mechatronics*, vol. 15, no. 6, pp. 853–861, 2010.
- [89] G. Rateni, M. Cianchetti, G. Ciuti, A. Menciassi, and C. Laschi, “Design and development of a soft robotic gripper for manipulation in minimally invasive surgery: a proof of concept,” *Meccanica*, vol. 50, no. 11, pp. 2855–2863, 2015.

- [90] J.-H. Low, I. Delgado-Martinez, and C.-H. Yeow, “Customizable Soft Pneumatic Chamber–Gripper Devices for Delicate Surgical Manipulation,” *Journal of Medical Devices*, vol. 8, no. 4, p. 044504, 2014.
- [91] E. Gultepe, J. S. Randhawa, S. Kadam, S. Yamanaka, F. M. Selaru, E. J. Shin, A. N. Kalloo, and D. H. Gracias, “Biopsy with thermally-responsive untethered microtools,” *Advanced Materials*, vol. 25, no. 4, pp. 514–519, 2013.
- [92] G. Tortora, T. Ranzani, I. De Falco, P. Dario, and A. Menciassi, “A Miniature Robot for Retraction Tasks under Vision Assistance in Minimally Invasive Surgery,” *Robotics*, vol. 3, no. 1, pp. 70–82, 2014.
- [93] U. Kim, D. H. Lee, W. J. Yoon, B. Hannaford, and H. R. Choi, “Force Sensor Integrated Surgical Forceps for Minimally Invasive Robotic Surgery,” *IEEE Transactions on Robotics*, vol. 31, no. 5, pp. 1214–1224, 2015.
- [94] R. B. Kelley, J. R. Birk, H. A. Martins, and R. Tella, “A Robot System Which Acquires Cylindrical Workpieces from Bins,” *IEEE Transactions on Systems, Man and Cybernetics*, vol. 12, no. 2, pp. 204–213, 1982.
- [95] V. A. Sujan, S. Dubowsky, and Y. Ohkami, “Robotic Manipulation of Highly Irregular Shaped Objects: Application to a Robot Crucible Packing System for Semiconductor Manufacture,” *Journal of Manufacturing Processes*, vol. 4, no. 1, pp. 1–15, jan 2002. [Online]. Available: <https://linkinghub.elsevier.com/retrieve/pii/S1526612502701291>
- [96] S. I. Cho, S. J. Chang, Y. Y. Kim, and K. J. An, “Development of a three-degrees-of-freedom robot for harvesting lettuce using machine vision and fuzzy logic control,” *Biosystems Engineering*, vol. 82, no. 2, pp. 143–149, 2002.
- [97] K. Tanigaki, T. Fujiura, A. Akase, and J. Imagawa, “Cherry-harvesting robot,” *Computers and Electronics in Agriculture*, vol. 63, no. 1, pp. 65–72, 2008.

- [98] E. Ramsden, *Hall-Effect Sensors: Theory and Application*. Elsevier Science, may 2006.
- [99] “Smooth-On, Inc. (2018). Mold Max™ 40 Product Information,” <https://www.smooth-on.com/products/mold-max-40/>.
- [100] “Smooth-On, Inc. (2018). Dragon Skin® FX- Pro Product Information,” <https://www.smooth-on.com/products/dragon-skin-fx-pro/>.
- [101] “Sensing.honeywell.com. (2018). SS39ET/SS49E/SS59ET Series Linear Hall-effect Sensor ICs,” https://sensing.honeywell.com/index.php?ci_id=50359.
- [102] “Electromagnetic Simulation Software,” <https://www.emworks.com/>.
- [103] “Teensy 3.6 Datasheet,” https://www.pjrc.com/teensy/card9a_rev1.pdf.
- [104] “LM324 Datasheet,” <http://www.ti.com/lit/ds/symlink/lm124-n.pdf>.
- [105] O. N. Testometric - Unit 1, Lincoln Business Park Lincoln Close, Rochdale, “Testometric Universal Testing Machine - 10kN.” [Online]. Available: <https://www.testometric.co.uk/10kn/>
- [106] T. E. Gould, M. Jesunathadas, S. Nazarenko, and S. G. Piland, “Mouth Protection in Sports,” in *Materials in Sports Equipment*. Elsevier, 2019, pp. 199–231. [Online]. Available: <https://linkinghub.elsevier.com/retrieve/pii/B978008102582600006X>

APPENDIX A

APPENDIX

A.1 Firmware of Sensor - Data Acquisition & Processing: Teensy 3.6

```
#define HALL_1 A15
#define HALL_2 A16
#define HALL_3 A8
#define HALL_4 A14
#define HALL_5 A1
#define HALL_6 A17
#define HALL_7 A6
#define HALL_8 A4
#define HALL_9 A2
#define HALL_10 A18
#define HALL_11 A7
#define HALL_12 A9
#define HALL_13 A3
#define HALL_14 A0
#define HALL_15 A19
#define HALL_16 A5

volatile uint8_t read_now = 0;
uint16_t signalValue[16] = {0};
double filteredValue[16] = {0};
double alpha = 0.005; //0.0609;
double y_n_1[16] = {0};
double y_n[16] = {0};
uint32_t last_millis = 0;
double offset_max[16] = {0};
double offset_min[16] = {0};
double offset[16] = {0};
double finalValue[16] = {0};
uint32_t sig_val = 0;
uint32_t fin_val = 0;
uint32_t frame_no = 0;
String data_packet;

uint8_t led_V = 25;
uint8_t led_GND = 24;
uint8_t led_status = 0;
```

```

uint32_t led_last_millis = 0;

void isr();
void readData();
void EMAfilter();

IntervalTimer timer_;

void setup() {

    pinMode(led_V, OUTPUT);
    pinMode(led_GND, OUTPUT);
    digitalWrite(led_GND, LOW);
    digitalWrite(led_V, HIGH);

    PORTE_PCR6 = PORT_PCR_MUX(1);
    GPIOE_PDDR |= (1<<6);
    GPIOE_PSOR = (1<<6); // turn on USB host power
    delay(10);

    Serial.begin(2000000);
    analogReadResolution(12);

    timer_.begin(isr, 1000);

    for (int k = 0; k < 16; k++) {
        offset_min[k] = 10000;
    }
    last_millis = millis();
    while(millis() - last_millis <= 5000) { //8000
        if (read_now) {
            readData();
            EMAfilter();
            if (millis() - last_millis > 3000) {
                for (int i = 0; i < 16; i++) {
                    if (filteredValue[i] > offset_max[i]) {offset_max[i] =
                        filteredValue[i];}
                    if (filteredValue[i] < offset_min[i]) {offset_min[i] =
                        filteredValue[i];}
                    offset[i] = ((offset_max[i] - offset_min[i]) / 2) + offset_min[i];
                }
            }
            read_now = 0;
        }
    }
}

void loop() {
    if (read_now) {
        readData();
        EMAfilter();
        for (int i = 0; i < 16; i++) {
            finalValue[i] = (filteredValue[i] - offset[i] > 0) ? (filteredValue[i]
                - offset[i]) : 0;
            finalValue[i] = map(finalValue[i], 0, (4095 - offset[i]), 0, 4095);

```

```

        //Serial.print((String) finalValue[i] + ' ');
        //Serial.print((String) signalValue[i] + ' ');
        data_packet = (String) frame_no + ':' + i + ':' + (uint16_t) finalValue[i];
        Serial.println(data_packet);
    }
    frame_no++;
    //Serial.println(frame_no);
    read_now = 0;
}
if ((millis() - led_last_millis) > 50) {
    led_status ^= 1;
    digitalWrite(led_V, led_status);
    led_last_millis = millis();
}
}

void readData() {

    signalValue[0] = analogRead(HALL_1);
    signalValue[1] = analogRead(HALL_2);
    signalValue[2] = analogRead(HALL_3);
    signalValue[3] = analogRead(HALL_4);

    signalValue[4] = analogRead(HALL_5);
    signalValue[5] = analogRead(HALL_6);
    signalValue[6] = analogRead(HALL_7);
    signalValue[7] = analogRead(HALL_8);

    signalValue[8] = analogRead(HALL_9);
    signalValue[9] = analogRead(HALL_10);
    signalValue[10] = analogRead(HALL_11);
    signalValue[11] = analogRead(HALL_12);

    signalValue[12] = analogRead(HALL_13);
    signalValue[13] = analogRead(HALL_14);
    signalValue[14] = analogRead(HALL_15);
    signalValue[15] = analogRead(HALL_16);
}

void isr() {
    read_now = 1;
}

void EMFilter() {
    for (int i = 0; i < 16; i++) {
        y_n[i] = (1 - alpha)*y_n_1[i] + alpha * signalValue[i];
        y_n_1[i] = y_n[i];
        filteredValue[i] = y_n[i];
    }
}
}

```